ISSN : 2347 - 9213

Indian Journal of Current Research (IJCR)

(Quarterly International Journal)

Vol.2, March 2015

Special Issue No.3

Recent Researches in Modern Engineering Materials

BON SECOURS COLLEGE FOR WOMEN

Accredited with 'A' Grade by NAAC
Affiliated to Bharathidasan University, Tiruchirappalli
UGC Recognized 2(f) and 12(B) Institution
VILAR BYPASS, THANJAVUR - 613 006, TAMIL NADU
Phone: +91-4362-257447, 255939, Fax: +91-4362-255939
Website: www.bonsecourscollege.org
Email id: bonsecourscollege02@gmail.com

JOURNAL COMMITTEE

Patron	:	**Rev. Sr. Jeyarani FBS** Secretary
Chief Editor	:	**Dr. Sr. D. Victoria Amalorpava Mary FBS** Principal
Associate Editors	:	**Ms. N. Rajarajeswari** Head, Dept. of Physics
		Mrs. N. Anuradha Assistant Professor of Physics
		Ms. K. Kalpana Assistant Professor of Physics
		Mr. T. Joseph Pandian IQAC Co-ordinator

Editor–in Chief, Editorial Board and Publisher take no responsibility for inaccurate, misleading data, opinion and statements appeared in the articles and advertisements published in the journal. It is the sole responsibility of the contributors and advertisers. No part of this journal can be reproduced without the written permission of the Editor- in- Chief who also holds the copyright © of the "Indian Journal of Current Research (IJCR)".

Editorial .....

In the last few years the role of the material has become very important with emergence of Nano material, Bio-materials, High temperature superconducting materials, polymers, etc., Material related issues can be found in all areas such as Biomedical, Telecommunication, Aeronautical Construction, Chemical & Mechanical field. Without the emerging materials, the development of technology would have been impossible. Computers, high performance engine and nuclear reactor required new and better materials than what had previously been available. This opens up new avenues for educational research in the field of "Crystal Physics and Modern Engineering Materials.

The foremost and developing research field in Modern Material World are Crystal Growth, Thin film Technology and Nanoscience & Technology. Crystal growth involves variety of research fields ranging from Surface Physics, Crystallography and Material Science to condensed mater physics. Though it has been studied extensively for more than 100 years, crystal growth still plays an important role in both theoretical and experimental research field as well as in application. Modern technology requires thin films for different applications. Thin film technology is the basis of astounding development in solid state electronics. Thin film studies have directly or indirectly leads to many new areas of research in solid state physics and chemistry.

Nano technology is the latest mega trend in science and engineering, that brings a wave of radical innovation and will definitely spark new industrial revolution in various applications. The theme of the Conference is of great relevance in the present context of development in science and technology. This Conference will enthuse many students and researches to take up their career in the field of "Crystal Physics and Modern Engineering Materials".

Editors

CONTENTS

S. No.	Title	Page No.
1.	**Ultrasonic Studies on Aqueous Solutions of Benzyl Alcohol** *N. Anuradha*	1
2.	**Investigations on Growth, Phytochemical and Optical Analyses of Amino Acid of Aloe Barbadensis Miller Added Potassium Dihydrogen Phosphate: the Nonlinear Optical Crystals** *R. Manimekalai, R. Jeyasree, S. Divya Bharathi & C. Ramachandra Raja*	7
3.	**Benzoxazole Derivatives – A Comparative Study** *M. Kayalvizhi & G. Vasuki*	14
4.	**Radio-Nuclear Power and Recent Structure Studies** *Dr. S. Santhosh Kumar*	21
5.	**Alkaline Polymer Electrolyte Fuel Cells** *V. Marypradeepa*	25
6.	**A Study on Radiations Emitted from Mobile Towers and its Biological Effects** *M. Anusha Devi & N. Rajarajeswari*	31
7.	**Synthesis, Growth and the Influence of Aloe Vera's Natural Amino Acid on Structural, Thermal, Mechanical and Surface Morphological Properties of Potassium Dihydrogen Ortho Phosphate** *R. Manimekalai, G. Anuradha, C. Ramachandra Raja*	37
8.	**Characterization of Spray Deposited Manganese Oxide Thin Films Fabricated at two Different Substrate Temperatures** *D. Vanitha*	42
9.	**Studies on Zinc Doped Cadmium Oxide Thin Films Prepared by Spray Pyrolysis Technique** *V. Rathna*	54
10.	**Structural and Photoluminescence Characterisation of Isilar Deposited Undoped and In Doped CdS Thin Films** *K. Kalpana*	68
11.	**Nanostructured Nickel Oxide Thin Films by Spray Pyrolysis and Ethanol Sensing Response** *Charles J & Lawrence N*	73

ULTRASONIC STUDIES ON AQUEOUS SOLUTIONS OF BENZYL ALCOHOL

N. Anuradha

Assistant Professor of Physics, Bon Secours College for Women, Vilar Bypass Thanjavur- 613 006.
Email id: jai.anuganesh@gmail.com

Abstract

Ultrasonics is widely used in recent years to study various molecular interactions. The present work deals with the study of acoustical parameters of aqueous solution of Benzyl Alcohol at different temperatures and at various molalities. From the experimental data of the density (ϱ), ultrasonic velocity (U) and viscosity (η), various acoustical parameters such as adiabatic compressibility (β), intermolecular free length (L_f), acoustic impedance (Z), relaxation time (τ), available volume (V_a) and molar compressibility were calculated. It is used in so many fields of scientific researches in physics, chemistry, biology, medicines and industry. About molecular packing, molecular motion and various types of interactions and their strength, influenced by the size, shape and the chemical nature of component molecules are also provided by these parameters.

Keywords: *Benzyl alcohol, Ultrasonic velocity and Viscosity, Adiabatic compressibility, intermolecular free length, molar compressibility and interactions*

1. Introduction

In recent years the measurement of ultrasonic velocity has been adequately employed in understanding the nature of molecular interaction in pure liquids and liquids mixtures. Ultrasonic propagation parameters yield valuable information regarding the behavior of liquid systems, because intramolecular and intermolecular association, dipolar interactions, complex formation and related structural changes affect the compressibility of the system which in turn produces corresponding variations in the ultrasonic velocity. Ultrasonic studies provide wealth of information about the state of the any solution (N. Karunanidhi, et al., 1999). The propagation of ultrasonic waves in a substance has become a fundamental test to investigate its properties (S.C. Bhatt, et. al., 1999). Prakash. S. and Singh. R., Singal. S.P., Sathyanarayanamurthy. M., Seshagiri Rao. M. G. and Ramachandra Rao. B., Garnsey et al. and many others have carried out ultrasonic study of aqueous and non aqueous solutions.

Benzyl alcohol occurs free and as ester in jasmine oil, Tolu and pera balsams. It is a typical and simplest primary aromatic alcohol and is isomeric with methyl benzonalCH_3-C_6H_4-OH (Soni & Chawla, 2001). Benzyl Alcohol is used as a chemical intermediate for synthesis of target molecules used in pharmaceuticals, cosmetics, preservatives and flavouring and fragrance agents. The various acoustical parameters of aqueous solution of Benzyl Alcohol are computed with the help of measured U, ϱ & η of solutions at different temperatures and at various concentrations.

2. Experimental Study

Aqueous solution of various molalities of Benzyl Alcohol is prepared with AR grade salt and double distilled water. A single pan balance accurate upto 0.0001g is used for weighing the salt. Density (ϱ) of the solution is measured using 25ml specific gravity bottle. The temperature is maintained with a circulating ultra thermo stating bath accurate to within ±0.1°C. The coefficient of viscosity (η) of the solutions is determined with a cannon-Fenske viscometer. It is a special type of Ostwald's viscometer.

Ultrasonic velocity (U) of the solution is measured by using a ultrasonic interferometer (Mittal Enterprises Ltd.) of fixed frequency 2 MHZ. The cell temperature is maintained with a circulating ultra thermostat accurate to within 0.1 K. The acoustical parameters are calculated from U, ϱ and η values using the following relations.

2.1. Acoustic Impedance (Z)

The specific acoustic impedance is related to density and ultrasonic velocity by the relation.

$$Z = U\rho$$

The value of specific acoustic impedance increases with concentration at a given temperature.

2.2. Adiabatic Compressibility (β)

The adiabatic compressibility values have been calculated from the measured ultrasonic velocities and densities.

$$\beta = \frac{1}{U^2\rho}$$

2.3. Intermolecular Freelength (L_f)

The free length is related to ultrasonic velocity and density as,

$$L_f = \frac{K}{\sqrt{\rho U}}$$

Where K is Jacobson's constant ($K = 2 \times 10^{-6}$)

2.4. Molar Sound Velocity (or) Rao's Constant(R)

Rao established the empirical relationship between molecular weight, density and ultrasonic velocity of liquids as

$$R = \frac{M}{\rho}(u)^{1/3}$$

Rao's constant or molar sound velocity shows increase with increase in concentration and temperature.

2.5. Molar Compressibility (or) Wada's Constant (W)

Wada Suggested a parameter known as molar compressibility to assess the strength of molecular interaction in liquids. It is obtain using the empirical relation

$$W = \frac{M_{eff}}{\rho}\beta^{-\frac{1}{7}}$$

Where, M_{eff} is the effective mass.

2.6. Acoustical Relaxation Time (τ)

Relaxation time can be calculated from viscosity coefficient density and ultrasonic velocity and is given by

$$\tau = \frac{4\eta}{3\rho U^2}$$

2.7. Relative Association (R_A)

Relative Association is obtained by using the formula

$$R_A = (\rho/\rho_o)(U_o/U)$$

Where U, Uo and ρ, ρ_o are the ultrasonic velocity and density of the solution and solvent respectively.

2.8. Available Volume (V_a)

The formula for available volume was suggested by Schaafs

$$V_a = (M_{eff}/\varrho)(U/U_\alpha)$$

Where, U_α = Schaaf's limiting value taken as 1600 m/s for liquids.

2.9. Vander Waal's Constant (b)

Vander Waal's constant is calculated by using the relation

$$b = (M/\rho).[1-(RT/MU^2)\{(1+MU^2/3RT^{1/2}-1\}]$$

Where, M = molecular weight,

R = 8.3143 $JK^{-1}mol^{-1}$, is the gas constant,

ρ = density

3. Results and Discussions

Ultrasonic velocity, Acoustical impedance, Adiabatic compressibility, Intermolecular free length, Molar Sound Velocity(or) Rao's constant, Molar Compressibility (or) Wada's Constant, Acoustical Relaxation Time (τ), Relative Association (R_A), Available Volume and Vander Waal's Constant of aqueous solution of Benzyl Alcohol at Various concentrations and temperatures are presented in Tables 3.1 – 3.10. Variation of these parameters with concentration and temperature are given in Graph 3.1 – 3.10.

Table 3.1. Ultrasonic Velocity (U) ms^{-1}

S. No.	Molality	Temperature				
		303 K	308 K	313 K	318 K	323 K
1.	0.001	1487.3	1524.00	1524.00	1525.33	1534.67
2.	0.002	1508.67	1530.00	1505.33	1508.67	1526.67
3.	0.003	1485.33	1512.67	1508.00	1492.67	1554.00
4.	0.004	1511.33	1522.67	1554.00	1565.33	1548.67
5.	0.005	1502.00	1526.67	1576.67	1499.33	1523.33

Graph 3.1 Molality Vs Ultrasonic Velocity

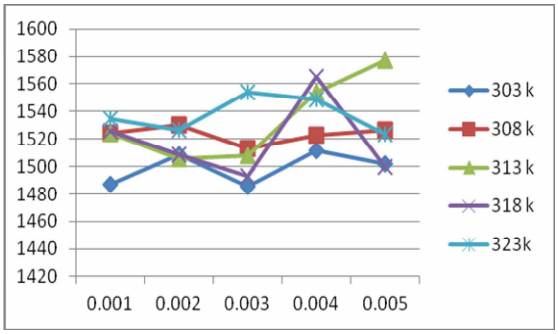

Acoustical Impedance(Z)

Table 3.2. Acoustical Impedance(Z) x 10^6 Kg m^{-2} s^{-1}

S. No.	Molality	Temperature				
		303 K	308 K	313 K	318 K	323 K
1.	0.001	1.4823	1.5164	1.5150	1.5119	1.5178
2.	0.002	1.5035	1.5223	1.4950	1.4953	1.5113
3.	0.003	1.4819	1.5068	1.4978	1.4796	1.5386
4.	0.004	1.5075	1.5150	1.5434	1.5529	1.5330
5.	0.005	1.4985	1.5191	1.5660	1.4862	1.5067

Graph 3.2 Molality Vs Acoustical Impedance

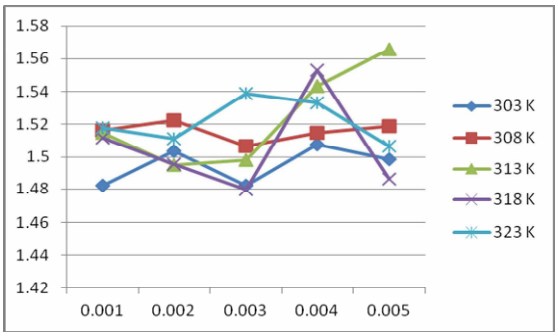

Table 3.3 Adiabatic Compressibility (β) x 10^{10} Pa^{-1}

S. No.	Molality	Temperature				
		303 K	308 K	313 K	318 K	323 K
1.	0.001	4.5359	4.3273	4.3311	4.3363	4.2932
2.	0.002	4.4085	4.2934	4.4434	4.4327	4.3342
3.	0.003	4.5431	4.3874	4.4273	4.5278	4.1823
4.	0.004	4.3890	4.3349	4.1695	4.1138	4.2120
5.	0.005	4.4430	4.3119	4.0501	4.4877	4.3570

Graph 3.3 Molality Vs Adiabatic Compressibility

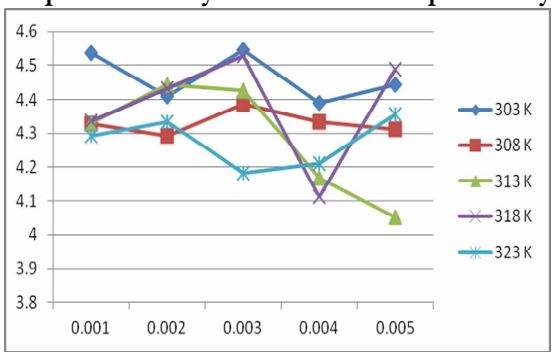

Table 3.4 Intermolecular Freelength(L_f) Å

S. No.	Molality	Temperature				
		303 K	308 K	313 K	318 K	323 K
1.	0.001	0.1347	0.1322	0.1336	0.1343	0.1350
2.	0.002	0.1328	0.1317	0.1353	0.1358	0.1356
3.	0.003	0.1348	0.1331	0.1351	0.1373	0.1332
4.	0.004	0.1325	0.1323	0.1311	0.1308	0.1337
5.	0.005	0.1333	0.1320	0.1292	0.1367	0.1360

Graph 3.4 Molality Vs Intermolecular Freelength

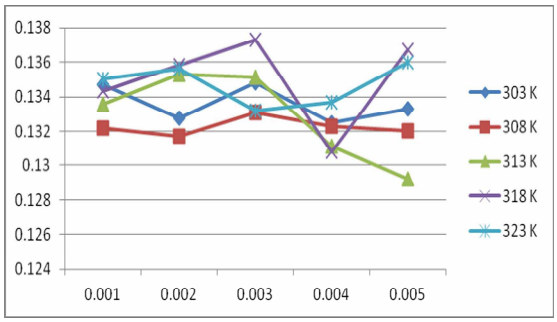

Table 3.5. Molar Sound Velocity (or) Rao's Constant(R) x 10^{-4} m^3 mol^{-1} $m^{1/3}$ $s^{-1/3}$

S. No.	Molality	Temperature				
		303 K	308 K	313 K	318 K	323 K
1.	0.001	2.0637	2.0839	2.0858	2.0929	2.1014
2.	0.002	2.0737	2.0868	2.0794	2.0851	2.0960
3.	0.003	2.0608	2.0768	2.0806	2.0776	2.1082
4.	0.004	2.0734	2.0839	2.1019	2.1093	2.1064
5.	0.005	2.0690	2.0857	2.1121	2.0812	2.0968

Graph 3.5 Molality Vs Rao's Constant

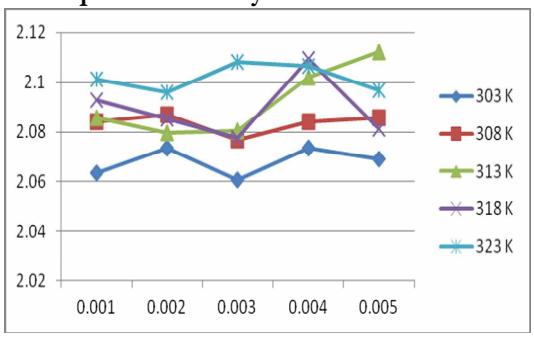

Table 3.6. Molar Compressibility (or) Wada's Constant(W) x10^{-4} m^3 mol^{-1} Pa$^{-1/7}$

S. No.	Molality	Temperature				
		303 K	308 K	313 K	318 K	323 K
1.	0.001	3.9079	3.9406	3.9437	3.9546	3.9690
2.	0.002	3.9242	3.9454	3.9333	3.9426	3.9602
3.	0.003	3.9034	3.9291	3.9353	3.9306	3.9800
4.	0.004	3.9238	3.9407	3.9699	3.9819	3.9772
5.	0.005	3.9167	3.9437	3.9865	3.9364	3.9617

Graph 3.6 Molality Vs Wada's Constant

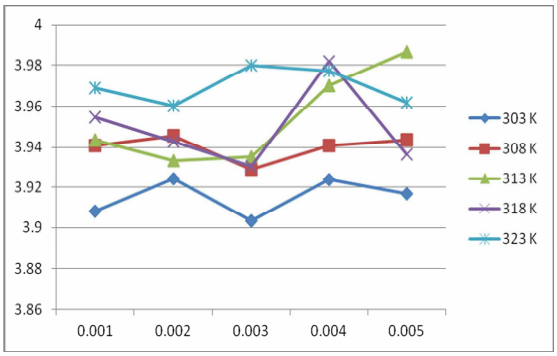

.

Table 3.7 Acoustical Relaxation Time (τ) x 10^{-13} s

S. No.	Molality	Temperature				
		303 K	308 K	313 K	318 K	323 K
1.	0.001	4.8731	4.1868	3.8074	3.4872	3.1551
2.	0.002	4.7476	4.1675	3.9148	3.5793	3.1949
3.	0.003	4.9037	4.2670	3.9190	3.6729	3.1084
4.	0.004	4.7599	4.2255	3.6973	3.3463	3.1363
5.	0.005	4.8296	4.2085	3.5963	3.6513	3.2482

Graph 3.7. Molality Vs Acoustical Relaxation Time

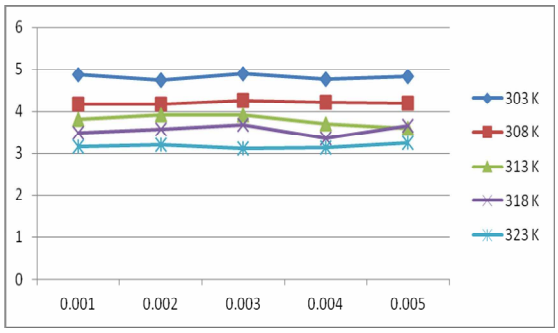

Table 3.8 Relative Association(R_A)

S. No.	Molality	Temperature				
		303 K	308 K	313 K	318 K	323 K
1.	0.001	1.0058	1.0000	1.0034	1.0036	1.0024
2.	0.002	1.0010	0.9987	1.0066	1.0073	1.0051
3.	0.003	1.0073	1.0036	1.0061	1.0110	0.9994
4.	0.004	1.0013	1.0003	0.9959	0.9959	1.0003
5.	0.005	1.0036	0.9995	0.9912	1.0095	1.0049

Graph 3.8 Molality Vs Relative Association

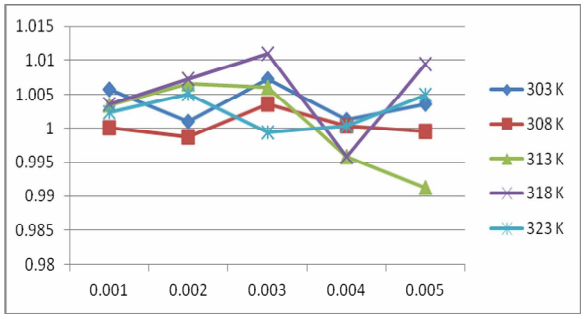

Table 3.9 Available Volume (V_a) x 10^{-6} m^3 mol^{-1}

S. No.	Molality	Temperature				
		303 K	308 K	313 K	318 K	323 K
1.	0.001	1.2731	0.8601	0.8609	0.8483	0.7439
2.	0.002	1.0321	0.7923	1.0735	1.0378	0.8343
3.	0.003	1.2945	0.9875	1.0432	1.2195	0.5233
4.	0.004	1.0013	0.8755	0.5217	0.3936	0.5841
5.	0.005	1.1066	0.8302	0.2646	1.1440	0.8732

Graph 3.9. Molality Vs Available Volume

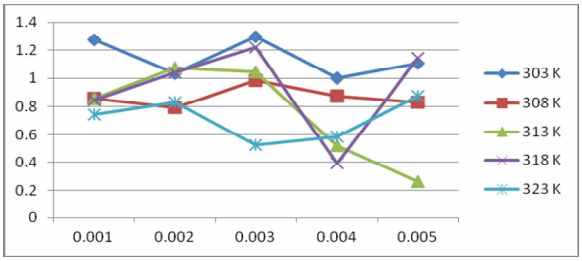

Table 3.10 Vander Waal's Constant (b) x 10^{-6} m^3 mol^{-1}

S. No.	Molality	Temperature				
		303 K	308 K	313 K	318 K	323 K
1.	0.001	24.34	25.06	24.74	24.52	24.50
2.	0.002	24.94	25.23	24.26	24.07	24.27
3.	0.003	24.27	24.73	24.33	23.63	25.01
4.	0.004	25.00	25.03	25.60	25.60	24.87
5.	0.005	24.74	25.15	26.23	23.82	24.21

Graph 3.10. Molality Vs Vander Waal's Constant

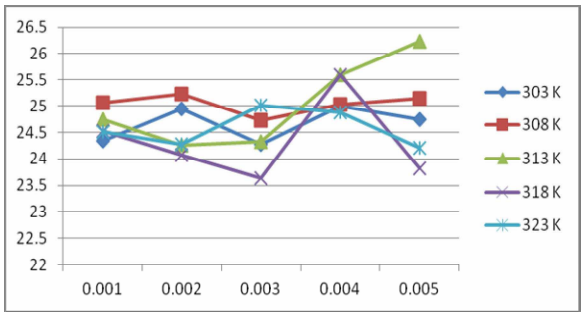

- At 303K, ultrasonic velocity reach a minimum value at 0.003m. At 313 K ultrasonic velocity reach a maximum value at 0.005m. At low concentration the number of hydrogen bonds formed may be less and at higher concentration, it may be more due to solute-solvent interactions.
- At 303K, acoustical impedance is minimum at 0.003m. the specific acoustical impedance can be used to access the strength of the intermolecular attraction. As the strength of intermolecular attraction increases ultrasonic velocity increases and consequently acoustical impedance also increases.
- Variation in adiabatic compressibility is found to be opposite to that of ultrasonic velocity in these solutions
- At 318K, intermolecular freelength gradually increases upto 0.003m and on further increase in concentration, there is a sudden dip at 0.004m. this indicates that the molecular associations are maximum at this concentration. Thereafter intermolecular freelength increases as the concentration is increases upto 0.005m
- Non-linear variation of Rao's constant with temperature and molality indicates significant molecular interactions in these solutions
- At 323K, Wada's constant decreases upto 0.002m and on further increases in concentration upto 0.003m. Increase in concentration upto 0.005m decreases Wada's constant.
- Acoustical relaxation time shows a general decrease with increase in temperature and also shows variation with change in concentration.
- At 323K, R_A & V_a increases upto 0.002m and on further increase in concentration R_A& V_a decreases upto 0.003m. thereafter R_A & V_a increases upto 0.005m.
- At 303K, Vander Waal's constant increases upto 0.002m and on further increase in concentration, Vander Waal's constant decreases upto 0.003m. As the concentration increases, Vander Waal's constant also increases upto 0.004m and thereafter decreses upto 0.005m.

4. Conclusion

The ultrasonic parameters like Ultrasonic Velocity, Acoustical Impedance, Adiabatic Compressibility, Intermolecular Freelength, Molar Sound Velocity (or) Rao's Constant, Molar Compressibility (or) Wada's Constant, Acoustical Relaxation Time, Relative Association, Available Volume and Vander Waal's Constant of aqueous solutions of Benzyl alcohol have been studied at various concentrations ranging from 0.001m to 0.005m and at various temperatures ranging from 303K to 323K.

These parameters play an important role in the estimation of molecular interactions in the solutions.

REFERENCES

1. Bhatt. S. C., Rawat. R. S. and Semwal. B.S. Acoustical investigation on some organic liquids. Journal of the Acoustical Society of India, 27, (1999). 297-300.
2. Garnsey. R. Boe., Mahoney.R. ant Litovity. T.A., J.Chem.Phys., 50(1969), 522.
3. Jacobson. B., Acta. Chem. Scand., 6(1952), 1485.
4. Karunanidhi. N., Subramanian. D. and Aruna. P. Acoustical Parameters of binary liquid mixtures. Journal of the Acoustical Society of India, 27, (1999). 305-307.
5. Prakash.S. and Singh. R., J. Acou.Soc.Ind., 4(1976), 36.
6. Rao. B. R., Proc. Ind. Acad. Sci., 25 (1947), 190.
7. Sathyanarayanamurthy. M., Ind. J.Pure and Appl.Phys., 3(1965), 156-159.
8. Schaafs, W., Z.Phys.,` 115(1940), 69.
9. Seshagiri Rao.M.G. and Ramachandra Rao.B., Ind. J.Pure and Appl.Phys., 1(1963), 362-366
10. Singal.S.P., Ind. J.Pure and Appl.Phys., 3(1965), 238-242.
11. Soni.P.L. and Chawla. H.M., "Text Book of Organic Chemistry" 28th Edn, Sultan Chand & Sons, New Delhi(2001).
12. Wada. Y., J. Phys. Soc. Japan, 4(1949), 280.

INVESTIGATIONS ON GROWTH, PHYTOCHEMICAL AND OPTICAL ANALYSES OF AMINO ACID OF ALOE BARBADENSIS MILLER ADDED POTASSIUM DIHYDROGEN PHOSPHATE: THE NONLINEAR OPTICAL CRYSTALS

R. Manimekalai[a], R. Jeyasree[b], S. Divya Bharathi[b], C. Ramachandra Raja[c*]

[a]*Department of Physics, A.V.V.M. Sri Pushpam College, Poondi, Thanjavur-613503, India.*

[b]*Department of Physics, Bonsecours College for Women, Thanjavur-613 005, India.*

[c]*Department of Physics, Govt.Arts College, (autonomous), Kumbakonam-612 001, India.*

Abstract

The amino acid of Aloe Barbadensis Miller added potassium dihydrogen phosphate nonlinear optical crystals (abbreviated as ABAKDP) were grown using slow solvent evaporation technique from aqueous solution. The High Performance Liquid Chromatography (HPLC) was carried out for the plant extract to identify the amino acids in it. The grown crystal was characterized by FT-IR, UV-Vis-NIR and photoluminescence. The colourimetric estimation method is adopted for the quantitative analysis of amino acid present in our grown crystal. The surface morphology was studied by etching studies.The Kurtz and Perry technique is used to confirm the Second Harmonic Generation (SHG) property of the grown crystal.

Keywords: *NLO crystal, solution growth, phyto-chemical analysis, photoluminescence, thin layer chromatography.*

Introduction

The fast development in the field of optoelectronics has stimulated the search for novel nonlinear optical crystals for efficient signal processing. New nonlinear optical (NLO) frequency conversion materials can have a significant impact on laser technology and optical communication [1-3]. One of the essential requirements for a material to exhibit second order optical susceptibilities is that the crystal should have noncentrosymmetric space group. The search for new frequency conversion materials over the past decade has concentrated primarily on organics. Much recent work have proved that organic crystals have very high nonlinear susceptibilities compared with inorganic crystals, but their use is restricted by their low optical transparencies, poor mechanical properties, low laser damage thresholds and on inability to produce and process large crystals. Purely inorganic NLO materials typically have excellent mechanical and thermal properties but posses relatively modest optical nonlinearities because of the lack of π electron delocalization. Nowadays, semi organic materials have been attracting a great deal of attention in the nonlinear field, because such materials have the potential for combining the high optical nonlinearity and chemical flexibility of organic materials with high thermal stability and excellent transmittance of inorganic substances [4-6]. Among the large family of second harmonic generation (SHG) materials, KDP is the most well studied crystal grown from solution and has served as a model system for studies of crystal growth mechanism [7,8]. The very first material to be used and exploited for its nonlinear optical (NLO) and electro-optic (EO) properties is potassium dihydrogen phosphate (KDP). It was used in the early experiments in nonlinear optics and it is still widely used in nonlinear optical devices. Still now, it continues to be popular as electro-optic materials because it is readily grown in useful sizes with good optical homogeneity [9-11].

Recently, the amino-acid family single crystals are gaining importance because they are highly feasible second-order NLO materials. They exhibit specific features of interest such as permanent magnetic dipole moment, molecular

chirality, which secures noncentro symmetric crystallographic structure, the absence of strong conjugated bonds, which lead to the wide transparency ranges in the visible and uv regions and the zwitter ionic nature of molecules, which favors the mechanical strength of the crystal for applications in devices [12]. Aloevera is the most important traditional herbal medicine. It is also known as "Plant of immortality" [13, 14]. In sanskrit, it is named as "Kumari" which means "ever young". Aloevera belongs to liliaceae family. The invention of X-rays and atom bomb brought Aloevera into popularity as it protected against radiation burns. From the literature [15-18] it is found that the Aloevera contains more amino acids, so we have extracted the natural amino acids from it.

As no reports are available on investigations on growth, phytochemical and optical analyses of Aloevera Barbadensis's aminoacid added potassium dihydrogen phosphate NLO (ABADP) biocrystals, we report in this article, the effect of Aloevera Barbadensis's amino acid with KDP on crystalline perfection, SHG efficiency, optical properties like FT-IR, UV-Vis-NIR, photoluminescence and the High Performance Liquid Chromatography (HPLC) was carried out for the plant extract. The colorimetric estimation method is adopted for the quantitative analysis and thin layer chromatography for qualitative analysis of amino acid present in our grown ABAKDP crystal respectively. The SHG efficiency of our grown crystal is studied using Kurtz and Perry technique. The obtained results are discussed below in detail.

Experimental

2.1. Phyto-chemical analysis

2.1.1. Aloevera amino acid extract preparation

For this investigation, disease free, 3 years old plant leaves are selected. The rind, sap, mucilage and gel are the four layers of the leaf. The gel portion is taken from the sterilized leaf. Five grams of gel is kept in 10 ml ethanol solvent. Then these are grind with the help of mortar and pestle and it is subjected to centrifugation for 10-15 min at 10,000 rpm. The supernatant is collected after filtration through what Mann no.1 filter paper and stored for further studies[19].

2.1.2. High Performance Liquid Chromatography (HPLC)

To identify the amino acids present in the extract HPLC analysis was carried out by using scimadzu**- spintron HPLC-530.**

Fig. (1a) shows the HPLC graph of (time-voltage) amino acid extract of Aloe Vera. From this analysis it is seen that there are five different peaks with various retention times, heights and areas. On matching the retention times with the known compounds, under similar conditions, the amino acids present in our extract are identified as homocystine, isoleucine, serine and tyrosine, from the recorded HPLC spectrum [20].

2.2. Crystal Growth

The saturated solution of KDP (analar grade) was prepared and then added with Aloevera amino acid extract in equal weight proportions. It was stirred well using magnetic stirrer. Then the solution is filtered and transferred to crystal growth vessel and crystallization was allowed to take place by the solvent evaporation technique. Well-defined, transparent single crystal (ABAKDP) of dimensions 2.5x0.5x0.5cm^3 as shown in fig.(1b) was harvested within the time span of 20-25 days.

Results and Discussion

3.1. FT-IR Spectral Analysis

FTIR spectroscopy is inter conversion of time-domain spectral data to frequency domain. Vibration bands in the region 1750-1400cm^{-1} give information on base-pairing while vibration bands in the region 1300-1000 cm^{-1} give information on the structure of the system. The FTIR spectra were recorded for the extract and our grown ABAKDP crystal (2a&2b), using **Perkin Elmer** Spectrophotometer in the wave length range 400-4000 cm^{-1} with the help of KBr pellet technique. The comparative

chart for Aloevera amino acid extract, KDP and our grown ABAKDP is shown in the table 1.

The characteristic vibrational frequencies that are occurring in amino acid extract of Aloevera like 3416,1406 and 1118 cm^{-1} because of the presence of amine, -C-H- groups [21] respectively are shifted to the lower frequency side due to the co-ordination of amines with KDP as seen in the table 3. The peak at 1641 cm^{-1} is confirming the presence of carboxylate ion in the system [22]. The frequencies at 861,542 and 454 cm^{-1} are also shifted to lower frequencies, ascertaining the formation of amino salts [23].

3.2. UV-Vis -NIRstudies

The UV-Vis-NIR transmission and absorption spectrum of ABAKDP crystal are recorded by using lamda 35 UV-Vis-NIR spectrophotometer in the range 190-1100nm. It is seen from the spectra (fig.3), that the crystal is transparent in the entire range thus indicating the suitability of ABAKDP for NLO applications. The knowledge of optical constants of a material such as optical band gap is essential to examine the potentiality of the material for optoelectronic applications [24-26]. Aloevera amino acid added KDP crystals is having greater percentage of transmission compared to pure KDP crystal. The lower cut-off wavelength is nearly 200nm.

From the UV-Vis-NIR spectral data, the optical band gapE_g is (3.75927eV) calculated, using the formula:

$E_g = hc/\lambda_g \times 1.602 \times 10^{-19}$ eV

Here $\lambda_g = 330 \times 10^{-9}$ m.

$E_g = 6.625 \times 10^{-34 \times 3} \times 10^8 / 330 \times 10^{-9} \times 1.602 \times 10^{-19}$

$E_g = 3.75927$ eV

3.4. Colorimetric Estimation Method

The quantitative estimation of amino acid present in the extract and in our grown ABAKDP crystal was determined by colorimetric estimation method. Using a spectro photo meter operating at 550nm, the presence/inclusion of amino acid is confirmed by colorimetric estimation method. At lower concentrations it will often give more accurate results. When minute amounts of substances are to be determined, that the colour reaction be highly sensitive therefore at such circumstances the colorimetric estimation method is particularly desirable. In visible region, the reaction product absorbs strongly. The strong absorption may be enhanced by the presence of groups like –OH, NH_2 and CH_3, called auxochromes. The colour produced should be sufficiently stable to permit an accurate reading to be taken. The colours arise from (i) d $\rightarrow$d transitions within the metal ion and (ii) n $\rightarrow\pi^*$ transitions within the ligands. Ninhydrin was added with our sample because it is having the capacity to bind with amino acids and imparts stable colour (pale yellowish green) to them. The colour intensity (optical density) was measured by **deep vision colorimeter** (digital) at 550 nm. [28].

Initially, the colorimeter was adjusted for null value with zero concentration (Blank) of the extract/crystal solution. Then, our samples (extract/crystal solution) added with ninhydrin was introduced [29] and the measured optical densities (ODs) were 0.096 and 0.046 for extract and our grown crystals respectively. With the help of the standards under similar conditions, the amount of amino acid present in the extract as well as in our crystal was found to be 165 and 106 μ g/ml respectively.

3.5. Photoluminescence (PL) Studies of ABAKDP Crystals

When a system is excited to the higher energy level by the absorption of photons then it decays to the lower energy levels, emitting a photon in the process. Luminescence is generally expected in compounds that are aromatic or those containing multiple conjugated double bonds. The PL spectrum was recorded for the powder sample at room temperature, using 1403-SPEX spectro - fluorometer with Argon ion laser (λ=457.9 nm at 2.71 eV) as the excitation source. The excitation spectrum is as shown in (fig.4).

It shows the purity and crystalline nature of the grown crystal. There are two peaks nearly at 390 and 460 nm having more or less the same intensity. This shows that the functional

groups are equally footed. There is also a medium peak ~at 550nm. The broadening of the peaks may be due to the flexibility of carboxylic groups of the amino acids that can make interactions with the neighboring groups in the crystal lattice [29,30]. The calculated optical band edge from the spectral data is 3.8015 eV.

3.6. Etching studies

Chemical etching is a simple and very powerful tool to analyze the defects present in the grown crystal surfaces. Dislocations can easily appear in the early stages of the growth itself. Once the damaged surface layer was removed by means of etching, a fresh surface appeared which in turn gave clear pits. The etched surface was dried and examined. Our sample ABAKDP crystal before etching (fig.5a) was examined through the optical microscope (Leitz Metallux-II). The crystal was etched by water etchant for five seconds and then analyzed through the microscope. Some well defined crystallographically aligned etch pits were observed on the surface and is shown in (fig. 5b).

3.7. Second Harmonic Generation Test

A preliminary study on the second harmonic generation efficiency of the crystal with reference to KDP was carried out by powder technique developed by Kurtz and Perry [31]. In this experiment, Q-switched Nd-YAG laser with the first harmonic output of 1064 nm was used. The crystal was ground to homogeneous powder and tightly packed in a micro capillary tube and mounted in the path of the laser beam of pulse energy 0.68 mJ. The SHG was confirmed by the emission of green light (λ=532 nm) collected by photo multiplier tube and displayed on the oscilloscope. SHG signals of intensity 3 mV was recorded for the sample while that for KDP was 8.8 m V. The second harmonic generation efficiency of ABAKDP is 2.9 times lesser than that of KDP.

Conclusion

The slow evaporation technique is used to grow ABAKDP single crystals. Aloevera amino acid extract is taken from the three years old plant leaf. The High Performance Liquid Chromatography is used to analyze the amino acids present in the extract. The important functional groups present in the grown crystals are assigned from the FTIR spectra. The linear optical transparency is observed by recording UV-Vis-NIR absorption and transmission spectra. The optical band edge is also calculated (3.7593 eV) from the transmission spectral data. The presence of amino acids in the grown crystals is qualitatively confirmed by thin layer chromatography (TLC). The photoluminescence spectrum is recorded to ascertain the SHG property of our grown sample. The optical band edge (3.8015 eV) is calculated from the PL spectral data. The colorimetric estimation method is used for quantification of amino acid present in the extract as well as in the grown crystals. The surface morphology is observed by etching technique. Kurtz and Perry technique is used to determine the SHG efficiency of the crystal.

Acknowledgements

The support rendered by St. Josephs college, Trichy , India, Gowri Biotech Private limited, Thanjavur, India; Indian Institute of Crop Processing Institute(IICPT), Thanjavur, India; Cresent Engineering College, Chennai, India, in our research work are also full heartedly acknowledged.

References

[1]. R.F. Belt, G. Gashurov , Y.S.Liu, Laser Focus 10,110 (1985)
[2]. R.S. Calark, Photonics Spectra 22, 135 (1988).
[3]. R.J. Gambino, Bull.Mater.Res.Soc. 15.20(1990).
[4]. Dongli Xu, Dongfeng Xue, J.of Cryst.Growth, 286(2006)108-113.
[5]. Y.J. Ding, X. Mu, X.Gu, J.Nonlinear Optical Physics and Materials, 9, 21(2000).
[6]. J. Ramajothi, S. Dhanuskodi and Nagarajan, Cryst.Res.Technol.39, 5(2004)414-420.

[7]. D.J. Williams, Angew. Chem. Int. Ed. Engl., 23 (1984) 690
[8]. S.R. Marden, J.W. Perry, Nonlinear Opt. Polym., 263 (1994) 1706
[9]. D.S. Chemla, J. Zyss, Non-linear Optical Properties of Organic Molecular Crystals, vol. 1,2Academic Press, London (1987)
[10]. J. Badan, R. Hierle, A. Perigaud, J. Zyss,in: D.J. Williams (Ed.), Nonlinear Optical Properties of Organic Molecules and Polymeric Materials, American Chemical Symposium Series, vol. 233, American Chemical Society, Washington, DC (1993).
[11]. S.A. deVries, P.Goedtkindt, W.J. Huisman, M.J.Zwanenburg, R. Feidenhans:l, S.L. Bennett, D.M. Smilgies, A. Stierle, J.J. DeYoreo, W.J.P. Van Enckevort, P. Bennema, E. Vlieg, J.Cryst.Growth 205(1999)202.
[12]. D.S. Chemla, J. Zyss, in: J.F.Nicoud, R.J. Twieg (Eds), Non-Linear Optical Properties of Organic Molecules and Crystals, Academic Press, London, Volume1 (1987)277.
[13]. The essential of Aloevera, the actions and the evidence by Dr.Peter Atherton, 2 nd edition, 1997.
[14]. Aloevera: A scientific Approach by Robert H Davis, Ph.D., 1997.
[15]. Urch, David, Aloevera Nature′s Gift: Great Britain Black down Publications, (1999), p-17.
[16]. Baker, O.T, The Amazing Ancient to Modern Useful Plant Aloe Vera: Amazing Plant of the Magic Valley, (Lemon Gove, CA: R. Prevost 1975), p.13-16.
[17]. A chemical Investigation of Aloe Barbedensis Miller, G.R. Waller, S. Mangiafico and C.R. Ritchey 1978. Proc. Okla.Acad.58, (1978)69.
[18]. Chemical studies of Aloevera Juice- Amino Acid Analysis, Gunmar Gjerstad, Advancing frontiers of plant sciences. Vol.28 (1969).
[19]. Satyavathi G.V., Medicinal Plants of India, ICMR publications, New Delhi, India.
[20]. Lindsay.S, Kealey.D, HPLC. J.Am.Chem.Soc. 110(1988)11.
[21]. Huixiang Tang, MiYan, Huizhang, MingzheXia, Deren Yang, Mater.Lett. 59(2005)1024.
[22]. M. Charbonnier, C. Courty, J.Phys. 28(1967)534.
[23]. L.I. Kozhevina, L.G. Skryabina, Yu.K. Tselinskii, J. Appl. Spectrosc.33 (1980)404.
[24]. K.V. Rajendran, D. Jeyaraman, R. Jeyavel, R. Mohankumar, P. Ramasamy, J. Cryst. Growth, 224(2001)122.
[25]. V. Pandey, N.Mehta, S.K. Tripathi, A. Kumar, Chalcogenide Lett. 2(2005)39.
[26]. M. Dongol, Egypt J. Solids, 25(2002)33.
[27]. Wagner.H, Bladt.S, Plant Drug Analysis, A Thin Layer Chromatography, 384(1996) 45.
[28]. S. Moore, W.H. Stein, Methods in Enzymol, Academic Press, New York, 1992.
[29]. P.S. Misra, E.T. Mertz, D.V. Glover, Cereal Chem.52 (1975)844.
[30]. AnieRoshan S, Cyriac Joseph, M.A. Ittyachen, Materials Letters, 49(2001)299-302.
[31]. S.K. Kurtz, T.T. Perry, J. Appl. Phys. 39 (1968) 3798.

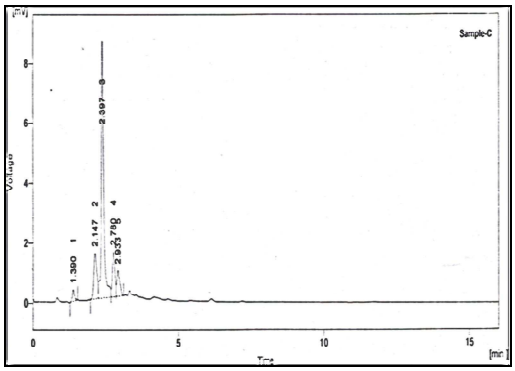

Fig. 1a High performance liquid chromatography (HPLC) of Aloevera amino acid extract

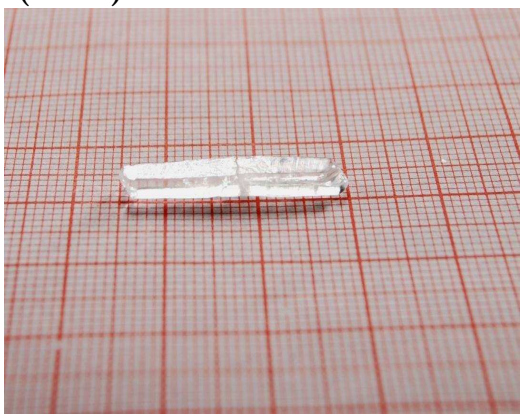

Fig. 1b As grown ABAKDP crystals

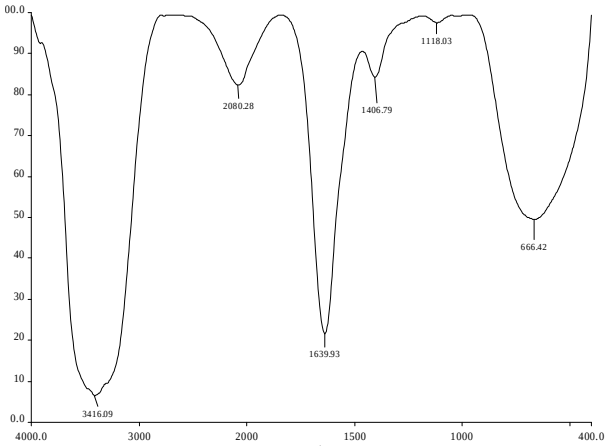

Fig.2a FTIR Spectrum of Aloevera extract

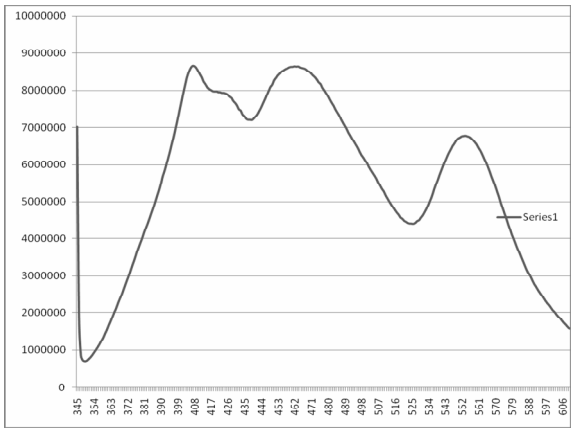

Fig.4 Photoluminescence spectrum of ABAKDP crystal

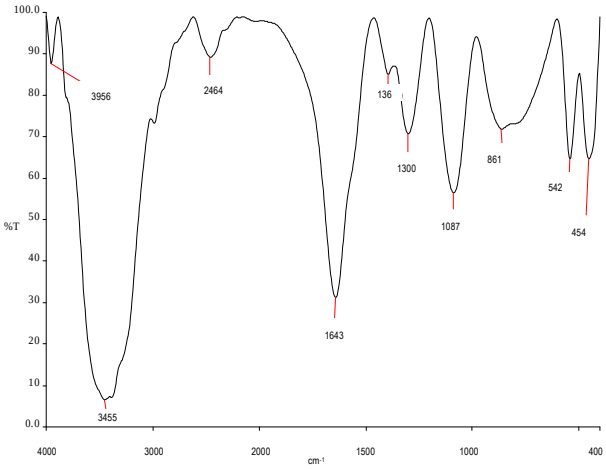

Fig. 2b FTIR Spectrum of ABAKDP crystal

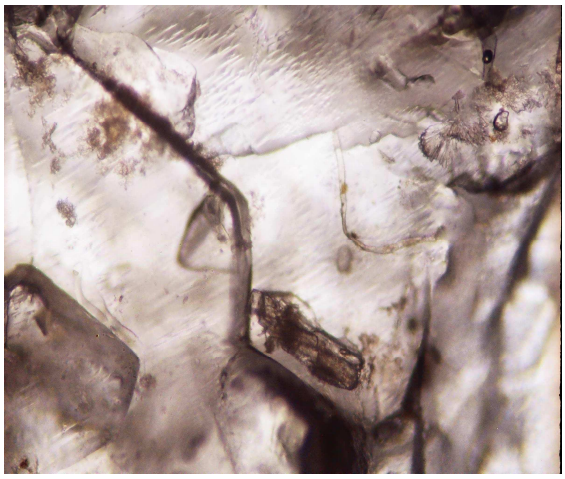

Fig.5a Etching pattern- before etching

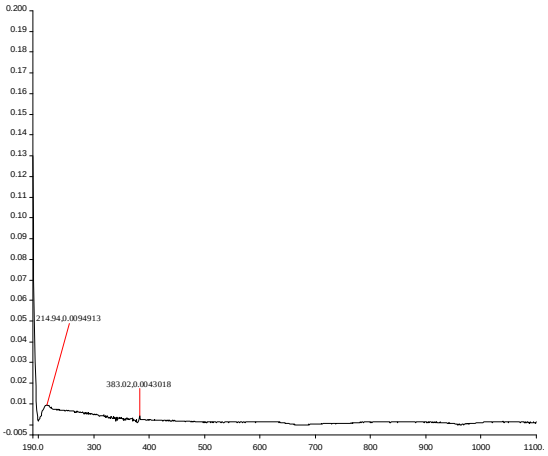

Fig. 3 Absorption spectrum of ABAKDP crystal

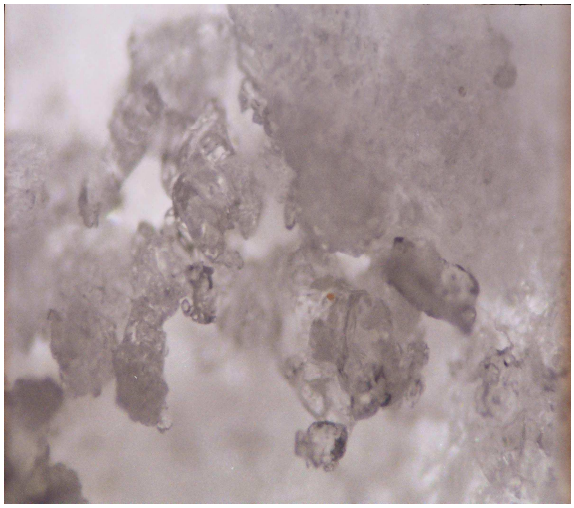

Fig.5b Etching pattern- after etching

Table 1: Tentative group assignments of ABAKDP crystal in cm^{-1}

Aloe Vera amino acid extract	Pure KDP	ABAKDP	Tentative Group Assignment
-	3956	3948	OH-bonding
3416	-	3410	NH_2^+ stretching
-	2464	2353	P-O-H bending of KDP
1639	-	1641	COO-asymmetric stretching
1406	-	1399	C-C-H stretching
1118	-	1101	C-H bending
666	861	727	PO_4^+ stretching
-	542 454	542 461	PO_4^+ rocking

BENZOXAZOLE DERIVATIVES – A COMPARATIVE STUDY

[1]M. Kayalvizhi & [2]G. Vasuki

[1]Lecturer in Physics,

[2]Associate Professor of Physics

Department of Physics, Kunthavai Naachiyaar Govt. Arts College (w), (Autonomous), Thanjavur- 613 007.

Email Id: kayalvizhi.mani@gmail.com

Abstract

Benzoxazole is primarily used in industry, medicinal chemistry, herbicidal activity, fungicidal activities and research. Substituted benzoxazoles have been reported to possess diverse chemotherapeutic properties including antibiotic, antimicrobial, antiviral, antitumor, pharmacological activities and multi-drug resistance cancer cell activities. Due to the vast applications the benzoxazole derivatives are taken under study. With its extensive uses as a drug for epilepsy, its cost-effective synthesis remained a great challenge for synthetic organic chemists. In a search for new benzisoxazole compounds with better biological activity, the title compounds, were synthesized and its crystal structures determined, in order to examine the structure–activity effects of the chloromethyl and methyl substituents on the benzoisoxazole ring. Using X-ray diffraction studies the molecular structure of these compounds were determined.

Keywords: *Benzoxazole, torsion angle, intra-molecular non-bonded interactions*

Introduction

Benzoxazole is an aromatic organic compound with a molecular formula, C_7H_5NO containing a benzene-fused isoxazole ring structure. Benzoxazole is primarily used in industry, medicinal chemistry, herbicidal activity, fungicidal activities and research. Substituted benzoxazoles have been reported to possess diverse chemotherapeutic properties including antibiotic, antimicrobial, antiviral, antitumor, pharmacological activities and multi-drug resistance cancer cell activities. In agriculture applications herbicidal activity has been identified as well as fungicidal activities against some plant pathogens. Some derivatives are also used as semiconductors and as corrosion inhibitors in fuels and lubricants. They are also important intermediates in the synthesis of many complex natural products. Among them, 3–substituted–1,2–benzisoxazole and their derivatives are emerging as potential antipsychotic compounds. The benzoxazole derivatives have also been under investigation because of their potential applicability using a light-emitting element in light-emitting devices and an electronic device (Kayalvizhi *et al.*, 2011 & 2012).

In the first compound, Fig.1, the torsion angle [N2—C3—C10—Cl = 121.31 (19)°] indicates that the side chain is anticlinal looking down the C3—C10 bond. The exocyclic angles C10—C3—C3*a* [129.35 (19)°] and C3—C3*a*—C4 [137.13 (19)°] deviate significantly from the normal values and this may be due to the intramolecular non-bonded interaction between the chlorine atom and an aromatic H atom [Cl···H4 = 3.2582 (8) Å]. In the crystal, adjacent molecules are linked *via* a pair of weak intermolecular C—H···N hydrogen bonds, Fig.2, forming dimers through a cyclic $R_2^2(8)$ association.

In the second compound, Fig.3, the widening of the exocyclic angle C10—C9—C3 [113.4 (2)°] from the normal value of 109° may be due to repulsion between neighbouring H atoms [H9···H11 = 2.2495 (1) Å]. The exocyclic angles C9—C3—C3a [132.1 (2)°] and C3—C3a—C4 [138.2 (2)°] deviate significantly from the normal value of 120° and this may be due to the intramolecular non-bonded interactions between the chlorine atom and H-atom H4 at C10 [Cl···H4 = 3.1169 (7) Å]. The isoxazole ring (O1, N2, C3, C3a, C7a) is planar [max. deviation 0.007 (3) Å]. Crystal packing of the compound is illustrated in Fig.4. There are no significant non-bonded

interactions present and the crystal structure is stabilized by van der Waals interactions only.

The r. m. s deviation of the 1,2-benzoxazole system lies in the range 0.0121 Å - 0.023 (3) Å for the N2 atom. The benzoxazole ring is almost planar. The N2 = C3 bond lies in the range [1.295(3) Å - 1.299 (3) Å] displays typical double-bond character, slightly longer than standard 1.28 Å value of a C = N double bond. The N2 - O1 [1.412 (2) Å - 1.417(2) Å] bond lies within the normal limits expected for a single N - O bond and the C7A - O1 [1.361 (3) Å - 1.363(2) Å] bond, although short, also lies within the anticipated range for a single C - O bond. The C - H…π and π - π interactions involving the benzoxazole and the benzene ring is also found in the first structure. There are no hydrogen-bonding interactions in the crystal structure, which is stabilized by van der Waals interactions only in the second compound.

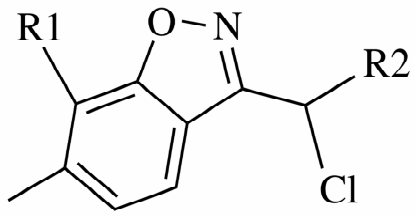

R1 = CH_3, R2 = C_6H_4
SCHEME
3-[Chloro(phenyl)methyl]-6-methyl-1,2-benzoxazole: CPMMB

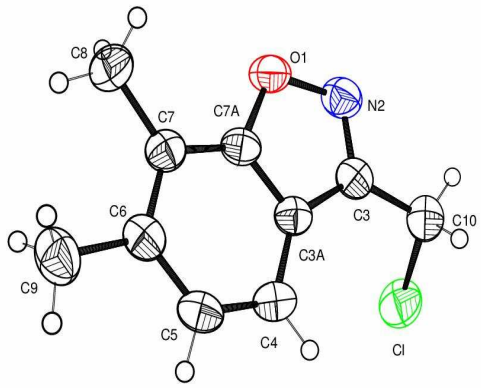

Fig.1

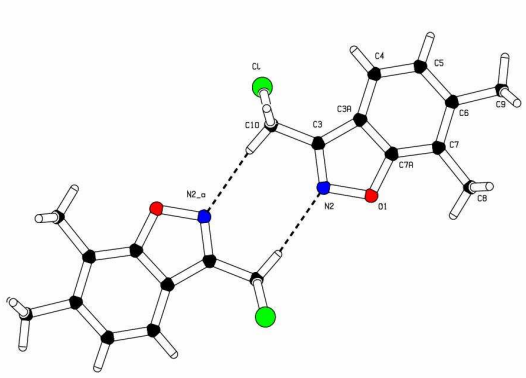

Fig.2
3-Chloromethyl-6,7-dimethyl-1,2-benzoxazole: CMDMB

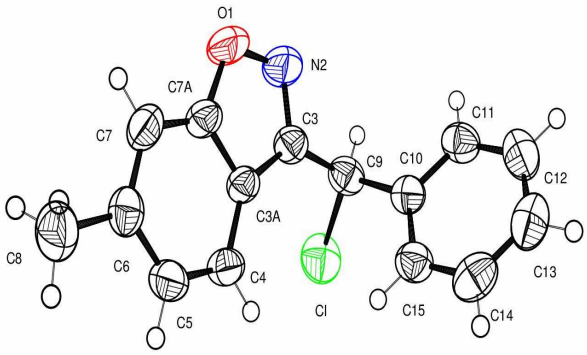

Fig.3

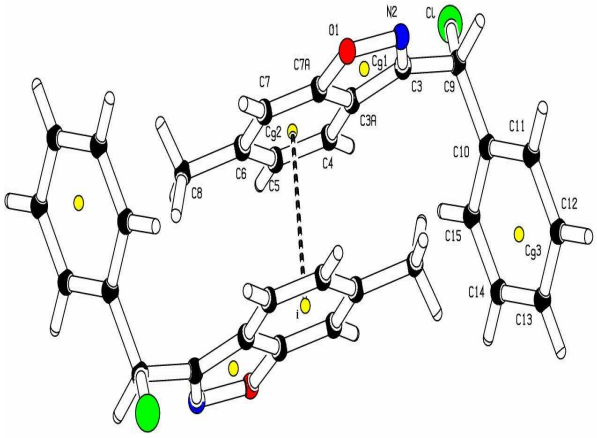

Fig.4

Table 1 Comparison of the bond lengths of the isoxazole ring (Å) of CPMMB and CMDMB with other closely related structures.

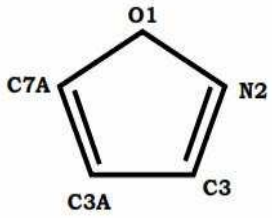

ISOXAZOLE RING (O1/N2/C3/C3A/C7A) of BENZOXAZOLE

Compound	O1-N2 (Å)	N2-C3 (Å)	C3-C3A (Å)	C3A-C7A (Å)	C7A - O1 (Å)	Reference
1	1.431(3)	1.301(3)	1.433(3)	1.378(3)	1.360(3)	Ge & Luo (2012)
2	1.427(4)	1.303(5)	1.433(6)	1.387(5)	1.371(5)	Banu et al., (2011a)
3	1.436(3)	1.304(4)	1.440(4)	1.389(4)	1.374(4)	Banu et al., (2011b)
4	1.4309(16)	1.3019(19)	1.439(19)	1.386(2)	1.3559(16)	Betz et al., (2011)
5	1.432(3)	1.294 (3)	1.431 (3)	1.381 (3)	1.357 (3)	Sun & Zhang et al., (2009)
6	1.440(3)	1.307(3)	1.441(3)	1.378(3)	1.35(3)	Naveen et al., (2007)
7	1.441(3)	1.2887(3)	1.438(3)	1.384(3)	1.364(3)	Wang et al., (2006a)
8	1.4275(19)	1.3023(18)	1.435(2)	1.390(2)	1.355(2)	Wang et al., (2006b)
9	1.436(3)	1.295(3)	1.439(3)	1.379(3)	1.351(3)	Ravikumar et al., (2005)
10	1.4317(17)	1.3007(19)	1.4382(19)	1.387(2)	1.3539(18)	Yathirajan et al (2005)
11	1.440(5)	1.297(6)	1.438(5)	1.380(7)	1.354(5)	Peeters et al., (1993)
12	1.438(7)	1.307(8)	1.45(2)	1.383(9)	1.354(8)	Jottier et al., (1992) Molecule A
	1.441(7)	1.306(9)	1.43(1)	1.373(9)	1.343(8)	Molecule B
13	1.418(2)	1.297(2)	1.434(2)	1.384(3)	1.364(2)	Domiano & Branca (1990) Molecule A
	1.411(2)	1.296(3)	1.440(3)	1.383(2)	1.364(3)	Molecule B
14	1.412(2)	1.299(3)	1.433(3)	1.378(3)	1.366(3)	Lisgarten & Palmer (1988)
15	1.412(3)	1.299(3)	1.430(3)	1.380(3)	1.361(3)	Present work CPMMB
16	1.417(2)	1.295(3)	1.420(3)	1.372(3)	1.363(2)	Present work CMDMB

Table 2 Comparison of the bond angles of the isoxazole ring (°) of CPMMB and CMDMB with other closely related structures.

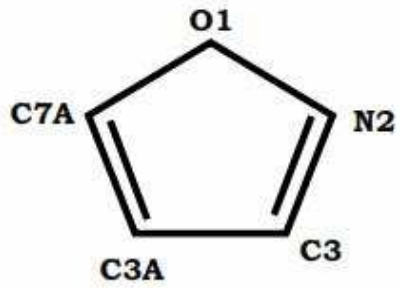

ISOXAZOLE RING (O1/N2/C3/C3A/C7A) of BENZOXAZOLE

Compound	O1-N2-C3 (°)	N2-C3-C3A (°)	C3-C3A-C7A (°)	C3A-C7A-O1 (°)	C7A-O1-N2 (°)	Reference
1	107.3(2)	111.2(2)	104.2(2)	110.2(2)	107.05(18)	Ge & Luo (2012)
2	107.0(3)	111.7(4)	104.2(3)	109.4(3)	107.7(3)	Banu et al., (2011a)
3	106.6 (2)	112.3 (3)	103.7 (3)	109.8 (3)	107.6 (2)	Banu et al., (2011b)
4	107.63(11)	111.00(13)	103.89(12)	110.37(12)	107.11(10)	Betz et al., (2011)
5	107.01(19)	111.6(2)	104.1(2)	109.8(2)	107.44(17)	Sun & Zhang et al., (2009)
6	106.82(18)	111.23(19)	104.23(19)	110.3(2)	107.44(17)	Naveen et al., (2007)
7	107.1(2)	112.1(2)	103.6(2)	110.2(2)	106.9(2)	Wang et al., (2006a)
8	107.03(13)	111.51(14)	103.84(13)	109.81(15)	107.80(11)	Wang et al., (2006b)
9	106.70(18)	111.7(2)	103.70(19)	110.3(2)	107.58(16)	Ravikumar et al., (2005)
10	107.03(11)	111.60(12)	103.50(12)	110.41(12)	107.44(11)	Yathirajan et al (2005)
11	107.0(4)	111.4(4)	104.1(4)	110.2(4)	107.3(4)	Peeters et al., (1993)
12	107.7(5)	110.0(6)	105.1(5)	109.7(6)	107.4(5)	Jottier et al., (1992) Molecule A
	106.1(5)	112.1(6)	103.2(6)	111.5(7)	107.2(5)	Molecule B
13	108.0(2)	111.1(1)	103.9(1)	109.9(2)	107.1(1)	Domiano & Branca (1990) Molecule A
	108.5(2)	110.7(2)	103.8(2)	110.1(2)	107.0(1)	Molecule B
14	107.7(2)	111.1(2)	104.0(2)	109.8(2)	107.4(2)	Lisgarten & Palmer (1988)
15	107.0(2)	111.9(2)	103.5(2)	110.0(2)	107.68(18)	Present work CPMMB
16	106.82(16)	112.04(18)	103.89(17)	109.88(17)	107.37(15)	Present work CMDMB

Table 3 Comparison of the torsion angles of the isoxazole ring (°) of CPMMB and CMDMB with other closely related structures.

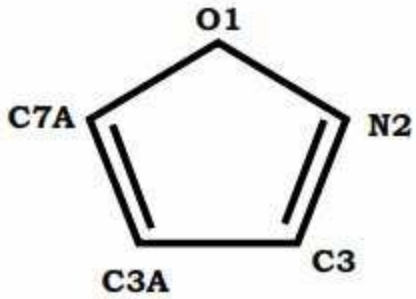

ISOXAZOLE RING (O1/N2/C3/C3A/C7A) of BENZOXAZOLE

Compound	O1-N2-C3-C3A (°)	N2-C3-C3A-C7A (°)	C3-C3A-C7A-O1 (°)	C3A-C7A-O1-N2 (°)	C7A-O1-N2-C3 (°)	Reference
1	0.7(3)	-1.2(3)	1.2(3)	-0.8(3)	0.0(3)	Ge & Luo (2012)
2	0.9(4)	-1.2(4)	1.0(4)	-0.5(4)	-0.3(4)	Banu et al., (2011a)
3	-1.7 (4)	1.6 (4)	-0.9 (3)	0.0 (3)	1.1 (3)	Banu et al., (2011b)
4	0.47(16)	-0.51(16)	0.33(16)	-0.07(15)	-0.26(15)	Betz et al., (2011)
5	1.0	-1.2(3)	0.9(2)	-0.4(2)	-0.4(2)	Sun & Zhang et al., (2009)
6	0.2(2)	-0.(3)	1.2(3)	-1.1(3)	0.6(3)	Naveen et al., (2007)
7	-0.7(3)	2.0(3)	-2.5(3)	2.2(3)	-0.9(3)	Wang et al., (2006a)
8	0.53(8)	-0.48(18)	0.23(17)	0.07(13)	-0.37(17)	Wang et al., (2006b)
9	-0.2(3)	0.4(3)	-0.4(2)	0.3(3)	-0.1(3)	Ravikumar et al., (2005)
10	-0.30(16)	-0.46(16)	1.08(16)	-1.29(16)	0.97(16)	Yathirajan et al (2005)
11	0.1(5)	0.3(6)	-0.7(5)	0.8(5)	-0.6(5)	Peeters et al., (1993)
12	0.80	-0.54	0.03	0.44	-0.77	Jottier et al., (1992) Molecule A
	-0.97	0.74	-0.17	-0.39	0.83	Molecule B
13	0.0	0.0	-0.1	0.1	0.0	Lisgarten & Palmer (1988)
14	1.3(3)	-0.9(3)	0.1(3)	0.7(3)	-1.2(3)	Present work CPMMB
15	0.5(2)	-0.4(2)	0.1(2)	0.2(2)	-0.5(2)	Present work CMDMB

Table 4 Compound names and references are given below for the Table 1, 2 & 3

Reference No.	Compound name	Reference
1	3-{2-[4-(6-fluoro1,2-benzoxazol-3-yl)piperidin-1-yl]ethyl}-9-hydroxy-2-methyl1,6,7,8,9,9a-hexahydropyrido[1,2-a]pyrimidin-4-one nitrate	Ge & Luo (2012)
2	3-{[5-(4-Bromophenyl)imidazo[2,1-b][1,3,4]thiadiazol-2-yl]methyl}-1,2-benzoxazole	Banu et al., (2011a)
3	3-{[6-(4-Chlorophenyl)imidazo[2,1-b][1,3,4]thiadiazol-2-yl]methyl}-1,2-benzoxazole	Banu et al., (2011b)
4	3-{2-[4-(6-fluoro-1,2-benzoxazol-3-yl)piperidin-1-yl]ethyl}-9-hydroxy-2-methyl1,6,7,8,9,9a-hexahydropyrido[1,2-a]pyrimidin-4-one	Betz et al., (2011)
5	4-(6-Fluoro-1,2-benzisoxazol-3-yl)-1-[2-(2-methyl-4-oxo-6,7,8,9-tetrahydro-4H-pyrido[1,2a]pyrimidin-3-yl)ethyl]piperidinium nitrate	Sun & Zhang et al., (2009)
6	(2-Ethoxyphenyl)[4-(6-fluorobenzo[d]isoxazol-3-yl)piperidin-1-yl]methanone	Naveen et al., (2007)
7	4-(6-fluoro-1,2-benzisoxazol-3-yl)-1-hydroxy-1-[2-(2-methyl4-oxo-3,4,6,7,8,9-hexahydro-2H-pyrido[1,2-a]pyrimidin-3-yl)ethyl]piperidine}	Wang et al., (2006a)
8	4-(6-fluoro-1,2-benzisoxazol-3-yl)-1-[2-(2methyl-4-oxo-3,4,6,7,8,9-hexahydro-2H-pyrido[1,2-a]pyrimidin-3-yl)ethyl]piperidinium}	Wang et al., (2006b)
9	4-(6-fluoro-1,2-benzisoxazol-3-yl)-1-hydroxy-1-[2-(2methyl-4-oxo-3,4,6,7,8,9-hexahydro-2H-pyrido[1,2-a]pyrimidin-3-yl)ethyl]piperidine N-oxide hydrogen peroxide methanol solvate	Ravikumar et al., (2005)
10	N-H^+...Cl^- and C-H...O interactions in 6-fluoro-3-(4-piperidinio)benz[d]isoxazole chloride	Yathirajan et al (2005)
11	3-{2-[4-(6-fluoro-1,2-benzoxazol-3-yl)piperidino]ethyl}-6,7,8,9-tetrahydro-2-methyl-4H-pyrido[1,2-a]pyrimidin-4-one (Risperidone)	Peeters et al., (1993)
12	3-{2-[4-(6-fluoro-1,2-benzoxazol-3-yl)-1-piperidinyl]ethyl}-2,9-dimethyl-4H-pyrido[1,2-a]pyrimidin-4-one (Ocaperidone)	Jottier et al., (1992)
13	1,2- Benzisoxazol-3-ylacetic acid	Domiano & Branca (1990)
14	1,2- Benzisoxazol-3-yl)methanesulfonamide	Lisgarten & Palmer (1988)
15	3-[Chloro(phenyl)methyl]-6-methyl-1,2-benzoxazole	Present work CPMMB
16	3-Chloromethyl-6,7-dimethyl-1,2-benzoxazole	Present work CMDMB

Table 5 Comparison of the dihedral angles between the planes observed in benzoxazole derivatives (°)

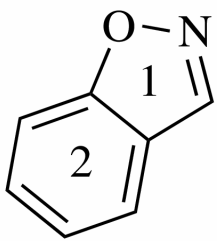

COMPOUND	Plane1 & Plane 2
CPMMB	1.54(13)°
CMDMB	1.40(9)°

CONCLUSION

The detailed conformational analysis on bond lengths, bond angles, torsion angles of two related benzoxazole derivatives and other closely related compounds indicates that the benzoxazole moiety is planar. The bond lengths, bond angles and torsion angles in the two related compounds are in good agreement with the expected values and are largely comparable with the corresponding values reported in the related structures values and they prove to be planar in conformation.

References

[1] 3-[Chloro(phenyl)methyl]-6-methyl-1,2-benzoxazole. M. Kayalvizhi, G. Vasuki, K. Ramamurthi, A. Veerareddy & G. Laxminarasimha. Acta Cryst. (2011). E67 o2999. CCDC No : 852230.

[2] 3-Chloromethyl-6,7-dimethyl-1,2-benzoxazole M. Kayalvizhi, G. Vasuki, A. Veerareddy & G. Laxminarasimha. Acta Cryst. (2012). E68, o3008. CCDC No : 907498.

[3] Ge, J and Luo, Y-H. Acta Cryst. (2012). E68, o2932.

[4] A. Banu, M. Ziaulla, N.S. Begum, R.S. Lamani and I.M. Khazi. Acta Cryst. (2011). E67, o154.

[5] A. Banu, M. Ziaulla, N.S. Begum, R.S. Lamani and I.M. Khazi. Acta Cryst. (2011). E67, o617-o618.

[6] R. Betz, T. Gerber, E. Hosten, A.S. Dayananda, H.S. Yathirajan and S. Thomas. Acta Cryst. (2011). E67, o2945-o2946.

[7] Y. Sun and H.-H. Zhang. Acta Cryst. (2009). E65, o1647.

[8] Naveen, S., Basappa., Sridhar, M.A., Shashidhara Prasad, J and Rangappa K.S. Acta Cryst. (2007). E63, o642–o643.

[9] D.-H. Wang, M.-H. Zhou and X.-R. Hu. *Acta Cryst.* (2006). E**62**, o3527-o3528.

[10] D.-H. Wang and Y.-J. Pan. Acta Cryst. (2006). E62, o768-o770.

[11] K. Ravikumar, B. Sridhar, S.G. Manjunatha and S. Thomas. *Acta* Cryst. (2005). E**61**, o2515-o2517.

[12] Yathirajan, H.S., Narasimhamurthy, T., Nagaraj, B., Nagaraja, P., Narasegowda, R.S. and Ravindranath S. Rathore. Acta Cryst. (2005). E61, o356-o358.

[13] O.M. Peeters, N. M. Blaton and C. J. De Ranter. Acta Cryst. (1993). C49, 1698-1700.

[14] W.I. Jottier, H.L. De Winter, O.M. Peeters, N.M. Blaton and C.J. De Ranter. *Acta Cryst.* (1992). C**48**, 1827-1830.

[15] P. Domiano and C. Branca. *Acta Cryst.* (1990). C**46**, 510-512.

[16] J.N. Lisgarten and R.A. Palmer. *Acta Cryst.* (1988). C**44**, 2013-2016.

RADIO-NUCLEAR POWER AND RECENT STRUCTURE STUDIES

Dr. S. Santhosh Kumar
Avvaiyar Govt. College for Women, Karaikal – 609 602, U. T. of Puducherry
(Current Address: Bharathidasan Govt. College for Women, Puducherry)

Abstract

Radioactive nuclei in the fields of industry and unmanned spacecrafts are the potential applications today with the well known medical and agricultural uses. The phenomenon of emitting particles by radioisotopes in the region of superheavy is discussed by considering the kinetic energy of the alpha particle emitted and thus to be useful in half-life prediction. The sphericity and magicity in this region is also discussed by predicting the most probable region of spherical isotopes.

Introduction

Researchers in nearly all fields of science use radioisotopes in their work. Radiation processing is a physical process in which food and agricultural commodities are exposed to controlled doses of radiant energy to achieve desirable effects such as inhibition of sprouting, ripening and destroying insect pests, parasites, pathogenic and spoilage bacteria. Food irradiation kills bacteria, insects and parasites that can cause food-borne diseases, such as salmonella, trichinosis and cholera. It does not make the food radioactive, and it does not affect food's attributes such as nutritional adequacy, flavour, aroma and safety.

In addition to the well known applications of radioactive elements in agriculture and medicine, today, practically every industry uses radiation in some way. Radioisotopes are used as imaging devices, to inspect finished goods for weaknesses and flaws, as tracers in process materials. These are also used in industry to inspect metal parts and welds for defects; to measure, monitor and control the thickness of sheet metal, textiles, paper napkins, newspaper, plastics, photographic film and other products; to calibrate instruments; to manufacture ceramics and glassware; and to generate heat or power for remote weather stations, space satellites and other special applications.

Unmanned spacecraft rely on radioisotope thermoelectric generators (RTGs) for the power they need for space exploration. RTGs use heat from plutonium to generate electricity. They are safe, reliable and long-lived, even in the harsh climate of our solar system. For example, Voyager 1, (launched in 1977), is at the edge of the solar system is still transmitting data. In addition to Voyager 1 & 2, RTGs have powered the missions like Galileo, Ulysses, Cassini and New Horizons spacecraft, etc. RTGs are essential for exploration in deep space, where spacecrafts are too far from the sun to use solar power. Hydrogel, Master-Slave Manipulator, Indian Environmental Radiation Monitoring Network and Dip N Drink Membrane Pouch are the other technological developments in nuclear industry.

To know about the phenomenon of nuclear radioactivity, it is very essential to have a knowledge about its location in the nuclear chart, its production and possible decay modes. While formation of the compound nucleus either by fusion or by bombardment it will be in excited state and which tries to come to its stable state by emitting either alpha, beta, gamma radiations or any particle or by fission. The knowledge about the structure of the nucleus and its alpha decay and the stability against fission or decay may provide the knowledge about the radioactive process. The structural effect on the stability or magicity of the nuclei located in the upper right end corner of the nuclear chart is discussed in the following sections.

Alpha Decay of Superheavy Nuclei

The prediction of the existence of superheavy nucleus (SHN) in 1960s, created an enthusiasm in synthesis and identification of

SHN, worldwide. A number of theories have been applied to predict the most stable nucleus in the superheavy region. But the location of the closed shell in the island of stability is still uncertain. Beyond the closed spherical shells at Z=82 & N=126, deformed shell closures at Z=108 & N=162 has been identified [1], but the next spherical shell closure is still open and different theoretical approaches predicted different spherical shell closures, depending on the model employed. While the macro-micro models favour Z=114 & N=184, the relativistic mean-field approaches generally prefer Z=120 & N=172 and self consistent Skyrme Hatree-Fock calculations focus at Z=126 & N=184. From the results obtained in recent years it is expected that there is a resemblance of lighter region of the nuclear chart in the upper right end corner.

Besides shell effects in the stability of SHN, the α-decay or spontaneous fission (SF) took important role. SHN with atomic number beyond 110 predominantly undergo sequential α-decay terminated by SF. In experiment, the measurement is mainly α-decay Q-values and half-lives, while the major goal of the theory is to predict the half-lives to serve the experimental design. Q-value, one of the crucial quantity for a quantitative prediction of decay half-life, affects strongly the calculation of the half-life due to the exponential law, i.e., α-decay rates exhibit an exponential dependence (Geigger – Nuttall) on emission energy. Therefore it is extremely important and necessary to obtain an accurate theoretical Q-value for a reliable half-life prediction. In fact, it is a challenge to interpret the existing decay data in literature, with theoretical models in order to better understanding the complex nuclear structure phenomena and reaction mechanism. For the study of SHN, mostly, macroscopic-microscopic approach is used [2] and some mass formulae were proposed that combine the liquid-drop ideology with the shell-model corrections of Strutinsky or Mayers-Swiatecki[3] and some empirical formulae. In order to improve the agreement with experiment, different corrections were introduced in the mass formula by different authors, but it is claimed that the original simple physical sense will be lost and question its adequacy to the fulfillment of the requirements of experiment.

In recent experiments, α decay has been indispensable for the identification of new nuclides. During the experimental design the values of the α-decay half-lives have to be evaluated and hence it is quite important and necessary to investigate the α decay of SHN theoretically. Although α-decay is very useful for the study of the nuclei, a quantitative description of them with a satisfying accuracy is difficult. Initially the α decay was interpreted as a consequence of quantum penetration of α-particle. At present, many theoretical approaches have been being used to describe the α-decay in fission theories. The half-life is extremely sensitive to the α-decay Q-value and an uncertainty of 1 MeV in Q-value corresponds to an uncertainty of α-decay half-life ranging from 10^3 to 10^5 times in the heavy element region [4].

Alpha Decay Q-value

Alpha decay is one of the most important properties of atomic nuclei, which is a powerful tool for the study of nuclei at the limit of stability (drip line), the closed shell nuclei and of heavy and superheavy nuclei. For the SHN, the α decay plays a key role since it determines the limit of their existence and allows to identify new elements.

The mass of the nuclei is calculated by computing the existing binding energy formula, $\Delta W(A,Z) = \alpha A - \beta A^{2/3} - \gamma Z^2/A^{1/3} - \xi((A/2)-Z)^2/A + \delta A^{-3/4}$, with the parameters, α=15.75MeV, β=17.8MeV, γ=0.71MeV, ξ=94.8MeV and $|\delta|$=34MeV, and hence the mass, $M(A,Z) = Zm_p + (A-Z)m_n - \Delta W(A,Z)$, where m_p and m_n are the proton and neutron masses respectively. The α-particle energy, $E_\alpha = [M(A,Z) - M(A-4, Z-2) - M(^4He)]c^2$. In order for α-decay to occur, energy must be conserved, such that Q-values for α-decay can be determined [5]

$$Q_\alpha = A E_\alpha/(A-4) + [6.53(Z-2)^{7/5} - 8(Z-2)^{2/5}]10^{-5}.$$

The discrepancy appeared between the calculated Q_α values with the $Q_{\alpha exp}$ is corrected with the term, $(-ln2)$ and is shown in Fig.1 And

hence the calculation is extended further to 290 nuclides in the SHN region (e-e, e-o, o-e, o-o) with $110 \leq Z \leq 128$, and the Q_α are plotted against Z, which is shown in Fig.3.

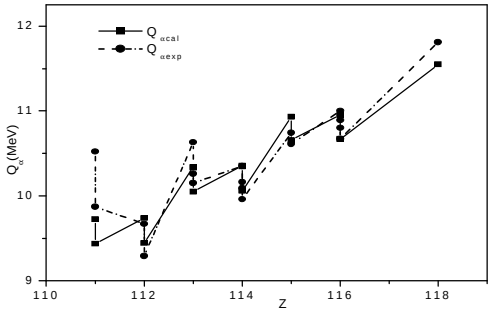

Fig. 1 Q_α modified and Experimental Q_α

The Q-value of the α-decay for odd Z nuclei are higher than even Z up to Z=120 and vice versa for Z >120, i.e., a major shift in the Q-value is observed, which is greatly influenced by shell effects. This may indicate the signature of sub-shell closure at Z=120, similar to the relativistic mean field prediction of next spherical shell closure [6]. Thus the existence of a shell effect (shell closure) is predicted at Z=120. Then, the obtained decay energies are used for the calculation of the decay half-lives using Viola-Seaborg formula [7].

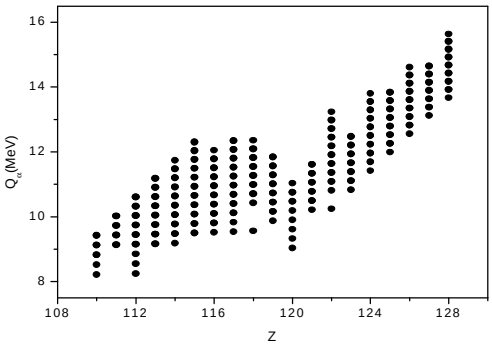

Fig. 2. Predicted Q_α for Superheavy Nuclei, $110 \leq Z \leq 128$.

Nuclear Structure in Superheavy region

The superheavy nuclei differ from stable nuclei by their larger charge and mass number. The strong coulomb potential induces significant changes in the proton shell structure. The large mass number of superheavy nucleus leads to a high average density of single particle levels and a small shift in position of it can influence the strength of single particle gaps and be crucial for determining shell stability of the nucleus. The large negative shell correction energy obtained for superheavy elements may responsible for the stability of the superheavy nuclei.

The formation of superheavy nuclei is either through hot or cold nuclear fusion and during this process the internal excitation of the single particles is to be considered effectively. Hence treating the system as a thermodynamical one is more suitable to find out the deformation of the system at different parametric consideration and so the statistical model is followed. Shell corrections to the nuclear free energy are temperature dependent. Nuclear structure effects upon the value of the level density parameter have been considered by the inclusion of shell corrections, pairing correlations and collective excitations.

Among the range of nuclei considered, from Z=120 to Z=126 with N=156 to 210, the shape of the nuclides around mass number A=290-320 for the systems Z=120-123 are spherical and for Z=124-126, the nuclides with A>300 show spherical configuration. Considering the shape transition, the range of the superheavy nuclei from 120-126 may be divided into two parts as, 120-123 and 124-126. The neutron number dependence for all the studied seven systems gave similar effects. The nuclei with Z=120, 121, 122 are having shape transition from prolate deformed to oblate deformed via spherical with increasing neutron number, while the nuclei from Z=124 to Z=126, transition is like a circle such as, triaxial, oblate, spherical, oblate and triaxial($\gamma = -160^o$; $\delta = 0.2$); no prolate deformation is observed in this region. Only Z=123 changes its shape from triaxial to oblate via spherical with increase in neutron number.

The nucleus Z=120 behaves as spherical when N=168-200, and further increase of N makes the nucleus deformed ($\delta = 0.1$) in oblate ($\gamma = -180^o$) shape. The nucleus $^{290\text{-}324}122$ is spherical

in shape and decrease in N makes the nucleus prolate deformation (δ = 0.1; γ = - 120^o) and increase of N makes it oblate deformed (δ = 0.1; γ = - 180^o). Compared to the nuclei Z = 120 - 122, the nuclei with Z = 123 - 126 are more oblate deformed (δ = 0.2; γ = -180^o).

As per the neutron separation energy obtained from the relation $S_N = -\sum_i [n_i^N \lambda_n n_i^N + (1-n_i^N) \lambda_n (1-n_i^N)]$ where n_i^N is the average occupation probability for neutron, for the nucleus Z=122, the most stable isotope is ^{302}122, compared to all other isotopes from A= 282 - 320 which coincides with the report of Patra et al.[9].

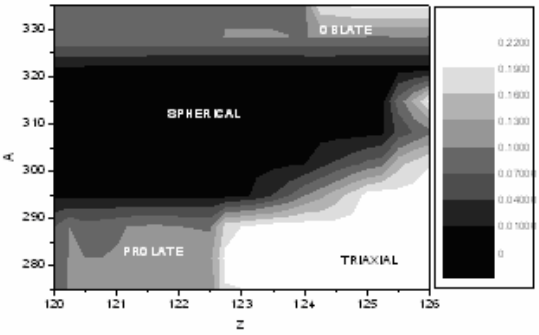

Fig. 3. Calculated ground state quadrupole deformation for SHN

The grouping of the ground state quadrupole deformation effect of around 350 nuclides in the superheavy region from Z = 120-126 is plotted in Fig.3. The higher deformations are obtained only either oblate or triaxial state. From the plot it is evidenced that the nucleus Z = 120 is having more isotopes with zero deformation at their ground state than the nucleus Z = 126. Hence, by considering the shape of the nucleus, among the nuclei studied from A = 120 to A = 126, the more stable nucleus seems to be Z = 120 rather than Z = 126, which may be correlated with the next proton shell closure beyond ^{208}Pb; which is in agreement with Adamian et al [10].

Summary

The radioactive properties and its applications in the new fields such as industry, and space missions are discussed. The most possible decay mode in the superheavy region, the alpha decay, is analysed by modifying the Q-value according to the experimental results and the calculations for around 290 isotopes are predicted. Since the role of deformation causing structural changes took a major role in predicting the next magic nucleus, the statistical theory is coded and the quadrupole deformation effect of 350 isotopes are predicted and grouped together to obtain the most probable region of occurrence of next magicity and from our calculations Z=120 will be having more number of spherical isotopes compared to the neighbouring nuclei. The change in shape with respect to angular momentum is also discussed. Since the deformed magic nuclei in the superheavy region is quite common, the neutron separation energy calculations performed reveals that the next most stable isotope may be ^{302}122.

References

[1] J. Dvorak et al., Phys. Rev. Lett. 97, 242501 (2006).
[2] P. Moller and J.R. Nix, J. Phys. G.20, 1681 (1994).
[3] W. D. Myers and W. Swiatecki, Nucl. Phys. 41, 1 (1966).
[4] P. Moller, et al., At. Data Nucl. Data Tables 66, 131 (1997).
[5] A. Aliotta, "Nuclear Physics 4 course notes", Edinberg University, 2012.
[6] M.Bender et al., Phys. Rev. C60, 034304 (1999)
[7] V.E.Viola and G.T.Seaborg, J. Inorg. Nucl. Chem. 28, 741 (1966).
[8] K. Rutz, et al., *Phys. Rev.* C**56** 238 (1997).
[9] S.K. Patra et al., Phys. Rev. **C80**, 034312 (2009).
[10] G.G. Adamian, et al., Phys. Rev. **C79**, 054608 (2009).

ALKALINE POLYMER ELECTROLYTE FUEL CELLS

V. Marypradeepa

Assistant Professor, Department of Physics, Bon Secours College for Women, Thanjavur.

Abstract

In recent decades, fuel cell technology has been undergoing revolutionary developments, with fundamental progress being the replacement of electrolyte solutions with polymer electrolytes, making the device more compact in size and higher in power density. Nowadays, acidic polymer electrolytes, typically Nafion, are widely used. Despite great success, fuel cells based on acidic polyelectrolyte still depend heavily on noble metal catalysts, predominantly platinum (Pt), thus increasing the cost and hampering the widespread application of fuel cells. Here, we report a type of polymer electrolyte fuel cells (PEFC) employing a hydroxide ion-conductive polymer, quaternary ammonium polysulphone, as alkaline electrolyte and nonprecious metals, chromium-decorated nickel and silver, as the catalyst for the negative and positive electrodes, respectively. In addition to the development of a high-performance alkaline polymer electrolyte particularly suitable for fuel cells, key progress has been achieved in catalyst tailoring: The surface electronic structure of nickel has been tuned to suppress selectively the surface oxidative passivation with retained activity toward hydrogen oxidation. This report of a H_2–O_2 PEFC completely free from noble metal catalysts in both the positive and negative electrodes represents an important advancement in the research and development of fuel cells.

FUEL CELLS

A fuel cell is a device that converts the chemical energy from a fuel into electricity through a chemical reaction with oxygen or another oxidizing agent.[1] Hydrogen is the most common fuel but hydrocarbons such as natural gas and alcohols like methanol are sometimes used. Fuel cells are different from batteries in that they require a constant source of fuel and oxygen to run, but they can produce electricity continually for as long as these inputs are supplied.

Overall reaction: $2H_{2(gas)} + O_{2(gas)} \rightarrow 2H_2O$ + energy

Because hydrogen and oxygen gases are electrochemically converted into water, fuel cells have many advantages over heat engines. These include: high efficiency, virtually silent operation and, if hydrogen is the fuel, there are no pollutant emissions. If the hydrogen is produced from renewable energy sources, then the electrical power produced can be truly sustainable.

Alkaline Fuel Cell Technology

Alkali fuel cells operate on compressed hydrogen and oxygen and generally use a solution of potassium hydroxide in water as their electrolyte. Operating temperatures inside alkali cells are around 90 to 100 degrees C. In these cells, hydroxyl ions (OH-) migrate from the cathode to the anode.

At the anode hydrogen gas reacts with the OH- ions to produce water and release electrons.[2] Electrons generated at the anode supply electrical power to an external circuit then return to the cathode. There are electrons react with oxygen and water to produce more hydroxyl ions that diffuse into the electrolyte. Cathode reaction faster in alkaline electrolyte leads to high performance, and low cost components these are advantages of alkaline fuel cell. One major advantage of alkaline fuel cell is they were used in Apollo space craft to produce both electricity and drinking water.

Alkaline fuel cell:

Anode reaction: $2H_2 + 4OH^- \rightarrow 4H_2O + 4e^-$

Cathode reaction: $O_2 + 4e^- + 2H_2O \rightarrow 4OH^-$

Overall reaction: $2H_2 + O_2 \rightarrow 2H_2O$

The Oxygen reduction in alkaline environments is more favourable than in acid environments, i.e., the voltage drop is lower. It yields the highest voltage at comparable current densities, leading to a higher efficiency of the system.

Consequently, the use of smaller amounts of noble metal electrocatalysts and the use of non-noble metal catalysts is more favourable in an AFC than in any other system. AFC_s also

operate well at room temperature and have a good cold start capability.

However, a major disadvantage is the CO_2 sensitivity of the alkaline electrolytes as alkaline electrolytes as carbonates are formed. In strong alkaline environments, the solubility of carbonates is rather poor.

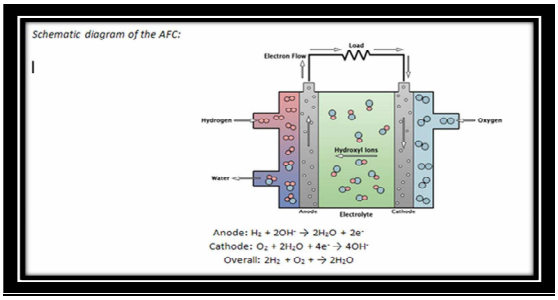

Fig. 1

This leads to the formation of carbonate crystals, capable of blocking electrolyte pathways and electrolyte pores.

$$CO_2 + 2OH^- \rightarrow CO_3^{2-} + H_2O$$

Alkali fuel cells operate at efficiencies up to 70 percent and, like other fuel cells, create little pollution. Because they produce potable water in addition to electricity, they have been a logical choice for spacecraft. A major drawback, however, is that alkali cells need very pure hydrogen or an unwanted chemical reaction forms a solid carbonate that interferes with chemical reactions inside the cell.[3] Since most methods of generating hydrogen from other fuels produce some carbon dioxide, this need for pure hydrogen has slowed work on alkali fuel cells in recent years. Another drawback has been the need for large amounts of a costly platinum catalyst to speed up the reaction. Researchers have worked to reduce the amount of platinum needed, and have eliminated the metal entirely from some designs.

Applications of Alkaline fuel cells

- **Fuel cells are efficient:** They convert hydrogen and oxygen directly into electricity and water, with no combustion in the process. The resulting efficiency is between 50 and 60%, about double, that of an internal combustion engine.[4]
- **Fuel cells are clean:** If hydrogen is the fuel, there are no pollutant emissions from a fuel cell itself, only the production of pure water. In contrast to an internal combustion engine, a fuel cell produces no emissions of sulphur dioxide, which can lead to acid rain, nor nitrogen oxides which produce smog or dust particulates.[4]
- **Fuel cells are quite:** A fuel cell itself has no moving parts, although a fuel cell system may have pumps and fans. As a result, electrical power is produced relatively silently. Many hotels and resorts in quite locations, for example, could replace diesel engine generators with fuel cells for both main power supply or for backup power in the event of power outages.
- **Fuel cells are modular:** That is, fuel cells of varying sizes can be stacked together to meet a required power demand. As mentioned earlier, fuel cells can provide power over a large range, from a few watts to megawatts.
- **Fuel cells are environmentally safe:** they produce no hazardouswaste products, and their only by-product is water (or carbon dioxide in the case of methanol cells).[4]

Fuel cells may give us the opportunity to provide the world with sustainable electrical power.

Alkaline polymer electrolyte

In recent decades, fuel cell technology has been undergoing revolutionary developments, with fundamental progress being the replacement of electrolyte solutions with polymer electrolytes, making the device more compact in size and higher in power density. Nowadays, acidic polymer electrolytes, typically Nafion, are widely used.

NAFION

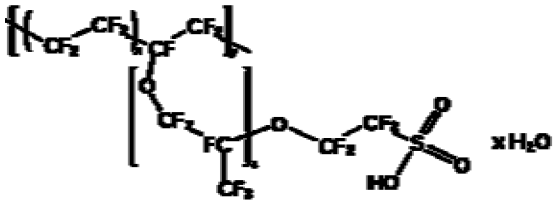

2.1

Nafion is a sulfonatedtetrafluoroethylene based fluoropolymer-copolymer discovered in the late 1960s by Walther Grot of DuPont.[5] It is the first of a class of synthetic polymers with ionic properties which are called ionomers. Nafion's unique ionic properties are a result of incorporating perfluorovinyl ether groups terminated with sulfonate groups onto a tetrafluoroethylene (Teflon) backbone.[6]Nafion has received a considerable amount of attention as a proton conductor for proton exchange membrane (PEM) fuel cells because of its excellent thermal and mechanical stability.

The chemical basis of Nafion's superior conductive properties remain a focus of research. Protons on the SO_3H (sulfonic acid) groups "hop" from one acid site to another. Pores allow movement of cations but the membranes do not conduct anions or electrons. Nafion can be manufactured with various cationic conductivities.

Nomenclature and molecular weight

Nafion can be produced as both a powder resin and a copolymer. It has various chemical configurations and thus several chemical names in the IUPAC system. Nafion-H, for example, includes the following systematic names:

- From Chemical Abstracts: ethanesulfonyl fluoride, 2-[1-[difluoro-[(trifluoroethenyl)oxy]methyl]-1,2,2,2-tetrafluoroethoxy]-1,1,2,2,-tetrafluoro-, with tetrafluoroethylene
- tetrafluoroethylene-perfluoro-3,6-dioxa-4-methyl-7-octenesulfonic acid copolymer

The molecular weight of Nafion is uncertain due to differences in processing and solution morphology.[11] The structure of a Nafion unit, shown at the top of the page, illustrates the variability of the material; for example, the most basic monomer contains chain variation between the ether groups (the z subscript). Conventional methods of determining molecular weight such as light scattering and gel permeation chromatography are not applicable because Nafion is of course insoluble, although the molecular weight has been estimated at 10^5–10^6 Da. Instead, the equivalent weight (EW) and material thickness are used to describe most commercially available membranes.

The EW is defined as the weight of Nafion (in molecular mass) per sulfonic acid group.[7] For example, Nafion 117 represents 1100 g EW + 0.007 inch in thickness. In contrast equivalent weight, conventional ion-exchange resins are usually described in terms of their ion exchange capacity (IEC) which is the multiplicative inverse or reciprocal of the equivalent weight.

$$IEC = 1/EW$$

Preparation

Nafion derivatives are first synthesized by the copolymerization of tetrafluoroethylene (TFE) (the monomer in Teflon) and a derivative of a perfluoro (alkyl vinyl ether) with sulfonyl acid fluoride. The latter reagent can be prepared by the pyrolysis of its respective oxide or carboxylic acid to give the olefinated structure.[8]

The resulting product is an $-SO_2F$-containing thermoplastic that is extruded into films. Hot aqueous NaOH converts these sulfonyl fluoride ($-SO_2F$) groups into sulfonate groups ($-SO_3^-Na^+$). This form of Nafion, referred to as the neutral or salt form, is finally converted to the acid form containing the sulfonic acid ($-SO_3H$) groups. Nafion can be cast into thin films by heating in aqueous alcohol at 250 °C in an autoclave. By this process, Nafion can be used to generate composite films, coat electrodes, or repair damaged membranes. [8]

Properties

The combination of the stable Teflon backbone with the acidic sulfonic groups gives Nafion its characteristics: [9]

- It is highly conductive to cations, making it suitable for many membrane applications.
- It resists chemical attack. According to DuPont, only alkali metals (particularly sodium) can degrade Nafion under normal temperatures and pressures.
- The Teflon backbone interlaced with the ionic sulfonate groups gives Nafion a high operating temperature, e.g. up to 190°C, however, in membrane form, this is not possible due to the loss of water and mechanical strength.

- It is a superacid catalyst. The combination of fluorinated backbone, sulfonic acid groups, and the stabilizing effect of the polymer matrix make Nafion a very strong acid, with pK_a ~ -6. In this respect Nafion resembles the trifluoromethanesulfonic acid, CF_3SO_3H, although Nafion is a weaker acid by at least three orders of magnitude.
- It is selectively and highly permeable to water.

Result and discussion

POWER MEASUREMENT

Cyclic voltammetry is the only electrochemical technique that may be used for evaluation of the kinetic parameters of heterogeneous electron transfer processes. The kinetic energy of oxidation reduction reactions obtained from cyclic voltammetry may be utilized to predict the utility of a given catalyst in catalyzing certain electrochemical processes.

The main factor for the increased fuel cell performance with temperature is the increase of electrolyte conductivity and not to enhanced electrode kinetics. Operation of the fuel cell at higher temperature might lead to the fuel cell performance.

The effect of KOH concentration on the ionic conductivity of Nafions 115 polymer electrolyte could be attributed decreased crystallinity of Nafion115 polymer with increasing KOH concentration. This is also increased the concentration conductive OH^- ions in the polymer matrix. The optimum concentration was controlled at 40-60 wt % in Nafion matrix and higher pt leading is more suitable for obtaining high performance.

The graph 1 shows that in the alkaline polymer electrolyte voltage decreases the current also decreases, at a particular voltage current attain a peak value and suddenly decreased. In this graph there is no intersection. Because Nafion matrix and higher pt leading is more suitable for obtaining high performance. And the graph 2 is similar to 1 but in the alkaline fuel cell with nickel electrode some fluctuations occur due to the temperature. This shows that alkaline polymer electrolyte membrane fuel cells gave a better result when compared to alkaline fuel cells.

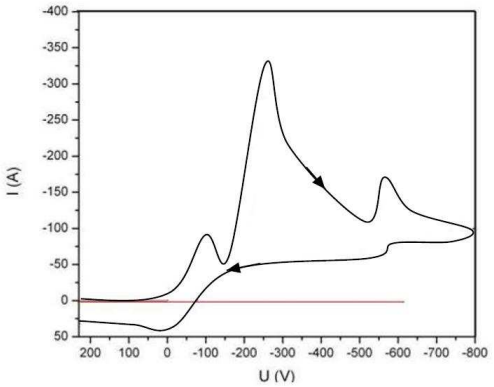

Fig. 1

U(V)	I(A)
230	0
0	0
-100	-80
-150	-64
-160	-64.7
-210	-124
-257.69	-328
-295	-217
-400	-158
-512	-113.5
-568.2	-149.62
-714	-114
-754	-102.59
-800	-100
-754	-94.58
-714	-83
-568.2	-75.9
-512	-59.21
-400	-51.81
-295	-47.38
-257.69	-43.99
-210	-40.16
-160	-35.44
-150	-26.59
-100	-13.2
0	44
230	31.82

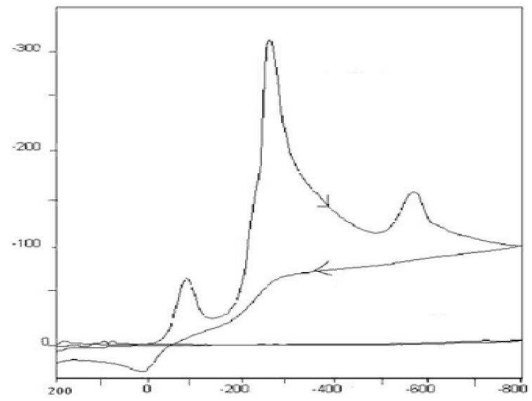

Fig.2

U(V)	I(A)
230	0
0	0
-100	-79.80
-150	-67.36
-160	-64.81
-210	-123.91
-257.69	-342.57
-295	-219
-400	-159
-512	-116.0
-568.2	-142.31
-714	-109.0
-754	-104.65
-800	-99.9
-754	-96.21
-714	-85.06
-568.2	-74.11
-512	-58.64
-400	-52.00
-295	-49.47
-257.69	-43.25
-210	-39.96
-160	-35.00
-150	-21.68
-100	-12.83
0	48.00
230	30.52

CONCLUSION

Ionic conductivity of membrane was measured at 80·C and reached maximum value for the thickness of Nafion115 doped with 4M KOH solution. Result showed excellent current-voltage characteristics from cyclic voltammetry test. The performance of the APEM system investigated shows a strong dependence on electrolyte concentration. The optimum conditions for the system investigated are 80·C and 4M dm^{-3} KOH gave performance of 60 W cm^{-2}at 25V.

References

1. Khuruni R.S **material science**, 5th Edition, ISBN 10:8121901464, publisher S. Chand & Company Ltd (2013).
2. Kordesh,]Gsellmann and B.Kraotschna **Power Sources** 9, 379(1983).
3. K.V. Kordesh and G. Simadee, **'Fuel Cells and their Applications'**, Wiley, Weinheim, New York, Tokyo (1996).
4. Larminie. J & Dicks A. (2000) **Fuel cell systems** explained, John Wiley & Sons.
5. Church, Steven (January 6, 2006). Del. firm installs **fuel cell, The News Journal** .p.B7.
6. Heitner-Wirguin, C. (1996). **"**Recent advances in **perflourinater dionomer membrances: structure, properties and applications"**. Journal of Membrane Science 120: 1-33.doi:10.1016/0376-7388 (96) 00155-X PMID 15669162.
7. Connoly, D.J.; Longwood; Gresham, W.F. (1996). **Fluorocarbon vinyl ether polymers** U.S. Patent 3,282,875.
8. Perma Pure LLC (2004 F). **"Nafion Physical properties** - Technical Notes and Articles. Retrieved 2006-03-22.
9. Schuster, M., Ise, M., Fuchs, A., Kreuer, K.D., Maier, J. (2005). **Proton and water Transport in Nano-separated Polymer membranes**. Germany: Max Planck-Institutfur Festkorperforschung, n.d..

GLOSSARY

FC : Fuelcells
AFC : Alkaline Fuelcells
APMFC: Alkaline Polymer Membrane Fuelcells
KOH : Potassium hydroxide

IEM : Ion Exchange Membrane
TFE : Tetrafluroethylene
PTFE : Polytetrafluroethylene
EW : Equivalent Weight
CV : Cyclic Voltammetry

A STUDY ON RADIATIONS EMITTED FROM MOBILE TOWERS AND ITS BIOLOGICAL EFFECTS

M. Anusha Devi[1] & N. Rajarajeswari[2]

[1]M.Sc. Physics,

[2]Head, Dept. of Physics, Bon Secours College for Women, Thanjavur-613 006.

Abstract

During the last three decades, a rapid growth in various areas of technology has been noticed especially in wireless communications, which has a large role in facilitating human life. Cell phone technology has revolutionized the telecommunication scenario in the world. The number of cell phones and cell towers keep on increasing exponentially without consideration to its disadvantages especially to the human users and the environment. All over the world, people have been debating about associated health risks due to electromagnetic radiation from cell phones and cell towers. The study was done on radiation emitted from cell phone towers and the preventive measures from the radiations emitted from cell phone towers were listed in order save human life.

***Key words**: Mobile phones, radiations, health hazards.*

INTRODUCTION

Cell phone technology has several advantages and has grown rapidly in the last decade. In India, there are nearly 80 crores cell phone subscribers and around 4.5 lakhs cell phone towers. Numbers of cell phones and cell towers are increasing without considering its disadvantages. All over the world, people have been debating about associated health risks due to electromagnetic radiation from cell phones and cell towers. There are several reports in the media and scientific literature.

A cell phone transmits 1 to 2 Watt of power in the frequency range of 824 to 849 MHz (CDMA), 890 to 915 MHz (GSM900), 1710 to 1780 MHz (GSM1800) and 1920 – 1980 MHz (3G). Radiation from cell phone is defined by its SAR (Specific Absorption Rate) value. In USA, SAR limit for cell phones is 1.6W/Kg, which is actually for 6 minutes per day use. It has a safety margin of 3 to 4, so a person should not use cell phone for more than 18 to 24 minutes per day. This information is not commonly known to the people in India, so crores of people use cell phones for more than an hour per day without realizing its associated health hazards. Majority of the people have reported that if they use cell phones for more than 20 minutes, their ear lobes get warm, which is due to heating of blood by microwave energy of cell phones. The problem starts with a pain in the ear that gradually develops into tinnitus or a ringing sensation which finally leads to hearing loss and ear tumor. Also, overuse of cell phones leads to drying of the skin and fluid in the eyes, sleep disorder, lack of concentration, memory loss, and even cancer.

International Agency for Research in Cancer (IARC), part of WHO (World Health Organization), designated cell phones as ***"Possible Human Carcinogen"***. They found evidence of increase in glioma and acoustic neuroma brain cancer for excessive cell phone users.

At many places, cell phone towers are mounted on the roof top of residential/ commercial buildings. Even though antenna radiates less power vertically down but the distance between the antenna and top floor is usually a few meters, so the radiation level in the top two floors remain very high.

EXPERIMENTAL WORK

Intensity of the radio frequency radiation can be defined as the Radiant energy emitted, reflected, transmitted or received, per unit time.

This is sometimes also called "radiant power" it is measured in watt (W *or* J/s).

Table 1.1 shows the measured values of radiation emitted from a cell phone tower

Distance in meter	Radiation in watt
5	1052.7
10	982.6
15	980.0
20	843.7
25	758.9
30	704.1
35	686.2
40	622.1
45	590.9
50	543.5
55	524.4
60	480.1
65	447.7
70	421.6
75	395.4
80	975.4
85	356.9
90	327.4
95	319.2
100	286.4

Table 1.1

Table 1.2 shows the measured values of radiation emitted from a cell phone tower for two floors.

Distance in meter	Radiations emitted from mobile tower from		
	Ground floor	First floor	Second floor
1	478.8	976.4	1242.2
2	352.9	796.4	1261.7
3	245.7	670.9	1182.8
4	276.1	500.9	1112.5
5	335.7	666.3	1066.3
6	272.9	558.1	992.4
7	215.7	484.8	976.6
8	178.6	421.9	975.2
9	263.5	382.2	937.5
10	252.9	581.7	1012.6
11	164.1	522.3	1261.7
12	146.4	454.5	1242.2

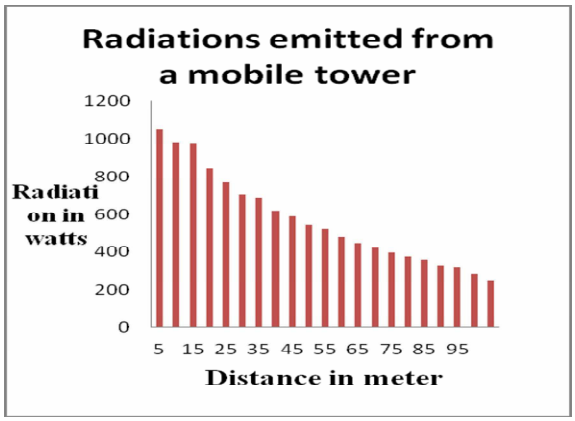

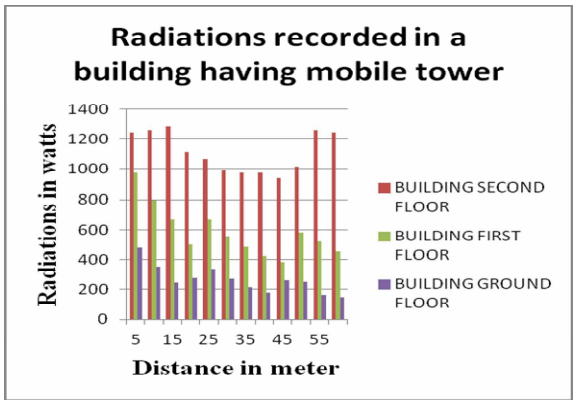

BIOLOGICAL EFFECTS

Increase in cancer risk

Heavy use of mobile phones can cause cancer. Use of mobile phones for >10 years give a consistent pattern of increased risk for brain cancer glioma (cancer of the glial cells that support the central nervous system) and acoustic neuroma (a benign tumor in the brain on a nerve related to hearing).

The risk is highest for ipsilateral (on the same side of the head where the cell phone is held) exposure. Children and teenagers, before the age of 20 are five times more likely to get brain cancer, as their brain is not fully developed and radiation penetration is much deeper. It is possible that today's young people may suffer an "epidemic" of the disease in later life. Besides increase in brain tumour and acoustic neuroma, there is an increased risk of several other types of cancers following prolonged exposure to mobile phone/ tower radiation, such as, Salivary gland tumors, uveal melanoma, lymphoma,

facial nerve tumors, skin, blood, testicular and breast cancer. Interphone study has also found a 'significantly increased risk' of some brain tumors for heavy users of mobile phones (> 20 minutes per day) for a period of 10 years or more. It is suggested that children should be discouraged from using mobile phones and restrict use to emergency while adults should "keep calls short".

DNA Damage

Cellular telephone frequencies can lead to damaged DNA. Studies show that microwave exposure at levels below the current FCC exposure standard, produces single and double strand breaks in DNA. EMR causes membrane leakage due to loss of calcium ions. Leaks in the membranes of lysosomes (small bodies in living cells packed with digestive enzymes) release DNAase (an enzyme that destroys DNA), which explains the fragmentation of DNA seen in cells exposed to mobile phone signals.

Microwave radiation can also interfere with the natural processes involved in DNA replication and repair, by subtly altering molecular conformation (architecture). Another possibility of DNA damage is via free radical formation inside cells. Free radicals kill cells by damaging macromolecules, such as DNA, protein and membrane and are shown to be carcinogenic. Several reports have indicated that electromagnetic fields (EMF) enhance free radical activity in cells as shown in Figure 3.2. The Fenton reaction is a catalytic process of iron to convert hydrogen peroxides, a product of oxidative respiration in the mitochondria, into hydroxyl free radical, which is a very potent and toxic free radical. Thus EMF affects the DNA via an indirect secondary process.

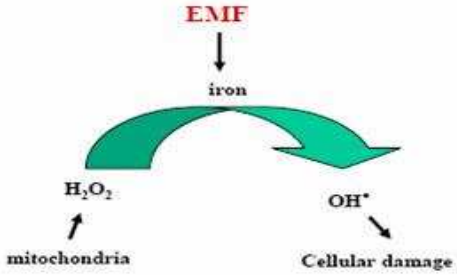

Damage to DNA is a central mechanism for developing tumors and cancer. When the rate of damage to DNA exceeds the rate at which DNA can be repaired, there is the possibility of retaining mutations and initiating cancer. DNA damage in brain cells can affect neurological functions and also possibly lead to neurodegenerative diseases."In old people, the gene repair system is not as effective as it is in younger people, makes them more vulnerable."

Risk to children and pregnant women

Children are more vulnerable to cell phone radiation as they:

- Absorb more energy than adults from the same phone owing to their smaller head and brain size, thinner cranial bones and skin, thinner, more elastic ears, lower blood cell volume, as well as greater conductivity of nerve cells and the energy penetrate more deeply. Tumors in the mid brain are more deadly than in the temporal lobe,
- Children's cells reproduce more quickly than adults which makes cancers more deadly,
- There immune system is not as well developed as adults hence are less effective against fighting cancer growth,
- Children have longer life time exposure.

Absorption of electromagnetic radiation from a cell phone (Frequency - GSM 900 MHz) is shown in Fig. 5 by an adult, 10 year old and a 5 year old child. When radiation hits the head, it penetrates the skull. The yellow area at the bottom is the location of the cell phone by the ear. The radiation penetrates the skull of an adult (25%), 10 year old (50%) and a 5 year old (75%).

Figure 3.1 Absorption of electromagnetic radiation from a cell phone based on age (Frequency GSM 900 MHz)

The younger the child, the deeper is the penetration due to the fact that their skulls are thinner and still developing. For these reasons it is critical that children under the age of 16 use cell phones only for short essential calls as they have much bigger danger of getting a brain tumor. Brain tumors have now taken over leukemia as the biggest cause of death amongst children. Due to these reasons countries like Belgium, France, Finland, Germany, Russia and Israel have publicly discouraged use of cell phones by children. An Independent research in Sweden last year concluded there was an Astonishing 420 percent increased chance of getting brain cancer for cell phone users who were teenagers or younger when they first started using their phones. A pregnant woman and the fetus both are vulnerable because of the fact that these RF radiations Continuously react with the developing embryo and increasing cells. Microwave radiation can damage the placental barrier; the membrane which prevents the passage of some materials between the maternal and fetal blood, protecting the fetus, implying that pregnant woman should avoid cell phone or use during emergency.

In a recent finding, an association was found between a mother's cell phone use during pregnancy and greater likelihood for spontaneous abortion, congenital malformations and behavioral problems in their children. It is believed that the eggs, which form the embryo, are affected and the damage will become apparent after the child reaches puberty. The Russian National Committee on Non-Ionizing Radiation Protection says that use of the phones by both pregnant women and children should be "limited". It concludes that children who talk on the handsets are likely to suffer from "disruption of memory, decline of attention, diminishing learning and cognitive abilities, increased irritability" in the short term, and that long-term hazards include "depressive syndrome" and "degeneration of the nervous structures of the brain".

CONCLUSION

The seriousness of the health hazards due to radiation from the cell phones and cell towers has not been realized among the common man. Cell operators continue to claim that there are no health issues. Even organizations like WHO, ICNIRP, FCC, etc. have not recommended stricter safe radiation guidelines. Cell phone/tower radiation is worse than smoking; as one cannot see it or smell it, and its effect on health is noted after a long period of exposure. Therefore, most of people tend to have casualness towards personal protection. Unfortunately, ignorance and non-awareness adds to this misery and all of us are absorbing this slow poison unknowingly. Even if people are aware of the radiation hazard, they may not have the choice to move away from it if the tower is installed near their office or residential building.

The radiations emitted from cell phone tower is more dangerous. We can't avoid the usage of cell phones. But we can reduce the usage of mobile phone by availing landlines, e-mails, letters etc. we can avoid installation of towers near residential buildings, schools, hospitals and reduce the usage of cell phone for living long live.

References

[1] "Cell death induced by GSM 900 MHz and DCS 1800 MHz mobile telephony radiation," Panagopoulos DJ, Chavdoula ED, Nezis IP, Margaritis LH,Mutation Research, 626 (1–2):69–78, 2007.

[2] "Genetic Damage in Mammalian Somatic Cells Exposed to Radiofrequency Radiation: A Meta-analysis of Data from 63 Publications, 1990–005" Vijayalaxmi, Radiation Research, 169(5):561–574, 2008.

[3] "Handheld Cellular Telephone use and Risk of Brain Cancer," Muscat JE, JAMA; the journal of the American Medical Association 284.23:3001-7, 2000.

[4] "Cellular telephone use and risk of acoustic neuroma," Christensen H C, Schüz J,Kosteljanetz M, Am J Epidemiol, 159:277– 83, 2004.

[5] "Cellular Phone Use and Risk of Benign and Malignant Parotid Gland Tumors – A Nationwide Case-Control Study," 6. S. Sadetzki, A. Chetrit, A. Jarus-Hakak, E. Cardis, Y.Deutch, S. *Duvdevani, A. Zultan, I. Novikov, L. Freedman, and M. Wolf, Am. J. Epidemiol.,* 167, 4, February 15, 2008, pp. 457-467.

[6] Agarwal A, Deepinder F, Sharma R, Randga G, Li J. "Effect of cell phone usage on semen analysis in men attending infertility clinic: an observational study", *Fertil Steril.*2007 May 3.

[7] "Permeability of the blood-brain barrier induced by 915 MHz electromagnetic radiation, continuous wave and modulated at 8, 16, 50 and 200 Hz", Salford L, Brun A, Eberhardt J, Malmgren,Persson B, *Microsc Res Tech.* 1994; 27(6):535-542.

[8] "A population-based prospective cohort study of personal exposure to magnetic fields during pregnancy and the risk of miscarriage", Li D, Odouli R, Wi S, et al. *Epidemiology* 2002; 13:9-20.

[9] "Neurobehavioral Effects Among Inhabitants Around Mobile Phone Base Stations", Abdel-Rassoul, et al. *Neurotoxicology* 2006 Aug 1.

[10] "Magnetic Fields and Cancer in Children Residing Near Swedish High Voltage Power Lines", Feychting M, Ahlbom A. *Am J Epidemiology* 1993; 138:467-481.

[11] "Epidemiological Evidence for a Health Risk from Mobile Phone Base Stations", Vini G. Khurana, Lennart Hardell, Joris Everaert, Alicja Bortkiewicz, Michael Carlberg, Mikko Ahonen, Int J Occup Environ Health 2010;16:263–267.

[12] The Biological Effects of Weak Electromagnetic Fields", Andrew Goldsworthy*, 2007*

[13] "Possible effects of Electromagnetic Fields (EMF) on Human Health", Scientific Committee on Emerging and Newly Identified Health Risks, 21 March 2007.

[14] IEEE Standard for Safety Levels with Respect to Human Exposure to Radio Frequency Electromagnetic Fields, 3 kHz to300Ghz;10.1109/ IEEESTD.1992.101091.

[15] American National Standard Safety Levels with Respect to Human Exposure to Radio Frequency Electromagnetic Fields, 300 kHz to 100 Ghz; 10.1109/IEEESTD. 1982. 81021.

[16] IEEE Standard for Safety Levels with Respect to Human Exposure to Radio Frequency Electromagnetic Fields, 3 kHz to 300 Ghz;10.1109 / IEEESTD. 1999. 89423.

[17] IEEE Standard for Safety Levels with Respect to Human Exposure to Radio Frequency Electromagnetic Fields, 3 kHz to 300 Ghz; Amendment 2: Specific Absorption Rate (SAR) Limits for the Pinna;10.1109/IEEESTD.2004.95603

[18] IEEE Standard for Safety Levels with Respect to Human Exposure to Radio Frequency Electromagnetic Fields,3 kHz to 300 Ghz; References:

[19] Cell phone linked to Brain Tumours, IEEE Spectrum, December 2004.

[20] What effects do mobile phones have on people's health? Health Evidence Network, WHO-200639.

[21] Mobile Phones and Health, Independent Expert Group on Mobile Phones – 2000

[22] Comar-Technical Information Statement-Radiofrequency Interference with Medical Devices-1998.

[23] Proceedings of the 20th Annual International Conference of the IEEE Engineering in Medicine and Biology Society, Vol. 20, No 6,1998-HEALTH AND SAFETY OF RADIO FREQUENCY RADIATION: U.S. MILITARY RESEARCH AND EXPOSURE STANDARDS -Michael R. Murphy and James H. Merritt Radio Frequency Radiation Branch, Directed Energy Bioeffects Division, Human Effectiveness Directorate, U.S. Air Force Research Laboratory .

[24] Federal Communications Commission Office of Engineering & Technology – Questions and Answers about Biological Effects and Potential Hazards of Radiofrequency Electromagnetic Fields.

[25] Cancer morbidity in subjects occupationally exposed to high frequency (radiofrequency and microwave) electromagnetic radiation - Stanislaw Szmigielski-1996, The Science of the Total Environment 180 (1996) 9-17.
[26] Electrical wiring configurations and childhood cancer, Wertheimer N, Leeper E Published in: Am J Epidemiol 1979; 109 (3): 273-284.
[27] "Handbook of Biological Effects of Electromagnetics Fields", edited by Frank S.Barnes, Ben Greenebaum, third edition, CRC Press.

SYNTHESIS, GROWTH AND THE INFLUENCE OF ALOE VERA'S NATURAL AMINO ACID ON STRUCTURAL, THERMAL, MECHANICAL AND SURFACE MORPHOLOGICAL PROPERTIES OF POTASSIUM DIHYDROGEN ORTHO PHOSPHATE

R. Manimekalai[a], G. Anuradha[b], C. Ramachandra Raja[c*]

[a]*Department of physics, A.V.V.M. Sri Pushpam College, Poondi, Thanjavur-613 503, India.*

[b]*Department of Physics, Kunthavai Naachiyar Govt. Arts College for Women (autonomous), Thanjavur -613 007.*

[c]*Department of physics, Govt. Arts College, (autonomous),Kumbakonam-612 001,India.*

Corresponding author: maniabi64@gmail.com

Abstract

Single crystals of Aloe vera's natural amino acid added with potassium dihydrogen orthophosphate (abbreviated as ANAKDP) have been grown by slow evaporation method at ambient temperature. Good quality single crystals of dimensions 2.5x0.5x0.5 cm³ were grown within the time span of 20-25 days. The extract is taken from the three years old Aloevera leaves and is subjected to High Performance Liquid Chromatography (HPLC) for the identification of amino acids present in the extract. The presence of amino acids in the grown ANAKDP crystals is confirmed by Thin Layer Chromatography (TLC) technique. The grown crystals were subjected to single crystal X-ray diffraction for the determination of unit cell dimensions and powder XRD for crystalline nature of the grown crystal. The thermal analyses namely TGA, DTA and DSC reveal the thermal stability. The Vickers micro hardness test was done to know about its mechanical strength. The mechanical properties of the crystal show that this material belongs to the category of hard material.

Key words: *Solution growth, optical crystal, high performance liquid chromatography, thin layer chromatography, scanning electron microscope, micro hardness.*

Introduction

Non linear optics has emerged as one of the most attractive field of current research in view of its vital applications in the area of optical modulation, optical switching, optical logic, frequency shifting, high-speed information processing, optical communications and optical data storage for developing technologies in telecommunication and signal processing and different optoelectronics applications [1, 2]. In the last years much attention has been paid to organic NLO materials due to their large nonlinear response, extremely fast switching time and convenient optimization routes through molecular engineering compared to the inorganic materials as the promising applications in optoelectronics [3,4]. Hence, the new types of NLO materials have been built from organic–inorganic complexes, in which the high optical nonlinearity of a purely organic compound is combined with the favourable mechanical and thermal properties of inorganic materials [5]. The very first material to be used and exploited for its nonlinear optical (NLO) and electro-optic (EO) properties is potassium dihydrogen phosphate (KDP). Its isomorphs are representative of hydrogen bonded materials that posses important piezoelectric, ferroelectric, electro-optic and nonlinear optical properties. They have [6,7] attracted interest of many theoretical and experimental researchers probably because of their comparatively simple structure and very fascinating properties associated with a hydrogen bond system involving a large isotope effect, broad transparency range, a high optical damage threshold and relatively low production cost [8-10].

Nowadays, the amino-acid family single crystals are gaining importance because they are highly feasible second-order NLO materials. They exhibit specific features of interest such

as permanent magnetic dipole moment, molecular chirality, which secures non-centro symmetric crystallographic structure, the absence of strong conjugated bonds, which lead to the wide transparency ranges in the visible and uv regions and the zwitter ionic nature of molecules, which favors the mechanical strength of the crystal for applications in devices [11]. Aloe vera is the most important traditional herbal medicineIts botanical name is "Aloe Barbadensis Miller". The invention of X-rays and atom bomb brought Aloe vera into popularity as it protected against radiation burns. From the literature [12-17]. It is found that the Aloevera contains amino acids, so we have extracted the natural amino acids from it, moderately at low cost.

EXPERIMENTAL

2.1. Phyto-chemical analysis

2.1.1. Aloe Vera amino acid extracts preparation

For this investigation the disease free, 3 years old plant leaves are selected. The leaf consists of four layers namely rind, sap, mucilage and gel. The gel portion is taken from the sterilized leaf. Five grams of gel is kept in 10 ml ethanol solvent. Then these are grind with the help of mortar and pestle and it is subjected to centrifugation for 10-15 min at 10,000 rpm. The supernatant is collected after filtration through what Mann no.1 filter paper and stored for further studies [18].

2.1.2. High Performance Liquid Chromatography (HPLC)

HPLC analysis was carried out by using scimadzu- **spintron HPLC-530**. Fig. (1) shows the HPLC graph of (time-voltage) natural amino acid extract of Aloe Vera. From this analysis it is seen that there are five different peaks (among five peaks, **one is unidentified**) with various retention times, heights and areas. From the recorded HPLC spectrum, the amino acids present in our extract are identified as homo cystine, isoleucine, serine and tyrosine by matching the retention times with the known compounds, under similar conditions [19].

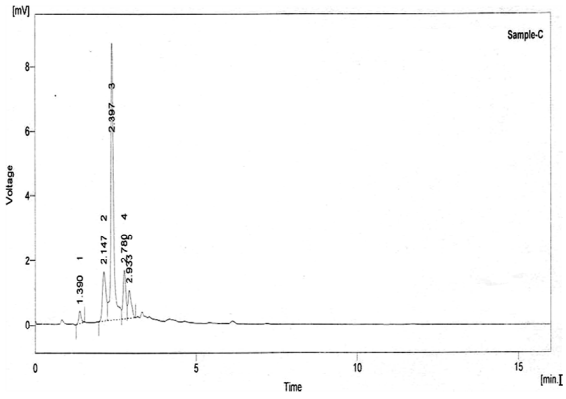

Fig. 1 High performance liquid chromatography (HPLC) of Aloe vera amino acid extract

2.2. Crystal Growth

The saturated solution of KDP (analar grade) was prepared and then added with Aloe Vera amino acids extract in equal weight proportions. It was stirred well using magnetic stirrer. That solution is filtered and transferred to crystal growth vessel and crystallization was allowed to take place by slow evaporation technique. Well-defined, transparent bio crystals were harvested within the time span of 20-25 days. Hereafter the grown natural amino acid of Aloe Vera added KDP crystals are named as ANAKDP.

RESULTS AND DISCUSSION

3.1. X-ray diffraction analysis

In order to obtain the unit cell parameters of our grown ANAKDP crystals, single crystal X-ray diffraction is recorded by using BRUKER NONIUS CAD4 single crystal X-ray diffractometer and powder XRD pattern was recorded using XPERT-PRO powder diffractometer with Cu K_α. radiation (λ=1.5405Å). It is noted that the addition of Aloe vera amino acid with KDP changed the crystal system and it belongs to monoclinic system, with the lattice parameters a = 6.318(4) Å, b = 10.549(1)Å and C= 6.307(4) Å also volume V=387.1(5) $Å^3$, the angles $\alpha=\gamma$ =90° and β=112.97(5)°. From the literature [20-23], is noted that KDP crystallize into tetragonal system. Hence it is clear that the addition of Aloe vera amino acid extract with

KDP changes the crystal system from tetragonal into monoclinic.

The powder XRD pattern is depicted in fig. (2). The crystalline nature is also confirmed by it and the peaks are indexed by using a computer programme, TJB Holland and SATRED FERN 1995. The unit cell parameters are also calculated from it. It is in good agreement with the single crystal XRD data and is shown in table. (2).

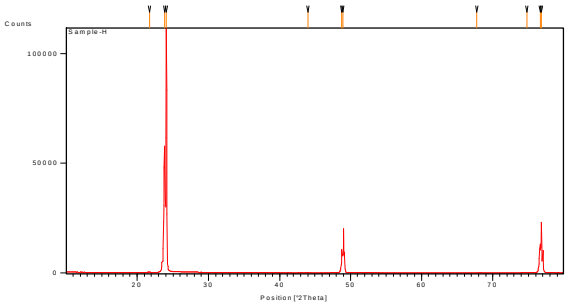

Fig.(2). Powder XRD pattern of ANAKDP

Table 2 Unit cell parameters of ANAKDP crystal

Unit cell parameters from powder XRD	Unit cell parameters from single crystal XRD	Unit cell parameters of pure KDP from single crystal XRD
a=6.4615Å ; b=10.49Å ; c=6.2872Å α=γ=90°; β=113.13° V=391.8953 Å³ Monoclinic system	a=6.318(4)Å ; b=10.549(1)Å ; c=6.037(4)Å ; α=γ=90°; β=112.97(5)° V=387.1(5) Å³ Monoclinic system	a= 7.434 Å b=7.434 Å c=6.945 Å Tetragonal system

3.2. Thermal analysis

The thermo gravimetric analysis (TGA), differential thermal analysis (DTA) and differential scanning calorimetry (DSC) were carried out to determine the thermal stability of the sample using **universal V4.TATA** instrument under nitrogen atmosphere.

The weight of the sample taken for the analysis was 2.6380 mg. The thermo grams (TGA and DTA} are recorded (fig.3a) in a same chart. The weight loss starts at 126.37°C and ends at 224.91°C. The weight loss is occurring in three steps [24,25]. At 224.91°C, the weight loss is about 99.41%. The observed weight loss below the melting point is due to dehydration. The second stage starts at 219.65°C and ends at 359.18°C. In DTA trace, there is an endothermic peak, which coincides with the TGA graph at 268.03°C. This temperature corresponds to the melting point of the sample. The melting of the ANAKDP is crystal is greater than that of pure KDP crystal.

There is one exothermic peak in DSC curve (fig.3b) nearly at 260.3°C, that corresponds to the melting point of the ANAKDP crystal. The minute deviation may be due to the presence of impurities in the sample. The third step in TGA is starting at 359.18°C and closes at nearly 1150°C. The successive plateaus correspond to the formation of anhydrous salt. The residue at the final temperature is about 84.16%.

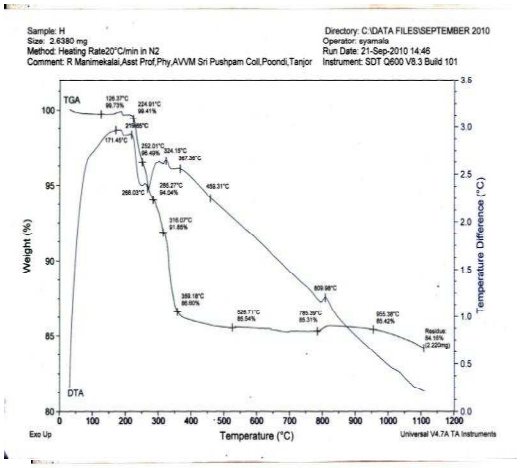

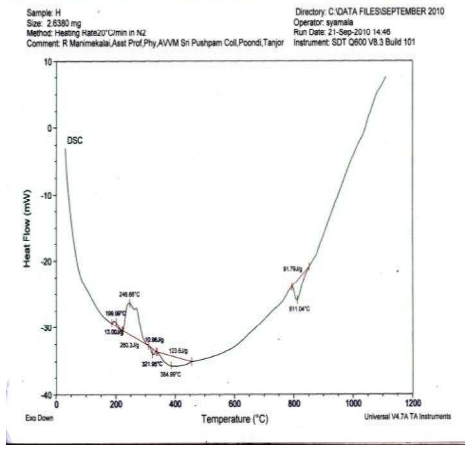

Fig. 3(a) TGA and DTA of ANAKDP
Fig. 3(b) DSC of ANAKDP

3.3. Thin Layer Chromatography (TLC) Analysis

The presence of amino acids in our grown crystal is confirmed by qualitative phyto-chemical analysis. The RF (resolution front or retention factor) values of the compound were calculated using the following formula (26).

R_F = Distance travelled by solute / Distance travelled by solvent

The RF value of the above results are compared with the standard values and the presence of amino acids was confirmed (fig.4) and is shown in the table 3.

Confirmation of Amino acid by Thin Layer Chromatography (TLC)

Amino acid

Amino acid

Table: 3 Amino acid analysis of *Aloe vera* crystal using TLC

S. No.	Compound	Color of the *spot*	Present (+)	RF value
1	Amino acid	Pink	+	0.73

3.6. Micro hardness measurement

One of the important properties of any device material is its mechanical strength, represented by its hardness. Physically hardness is the resistance offered by a material to localized plastic deformation caused by scratching or by indentation. Our grown crystal with smooth surface was selected for micro hardness study. Indentations were made and the average value of diagonal length was used to calculate micro hardness [28]. Vickers micro hardness value was determined using $Hv = 1.8544\ p/d^2$ in Kg/mm^2. The hardness value was found to decrease with the load and its work hardening co-efficient is 1.5.

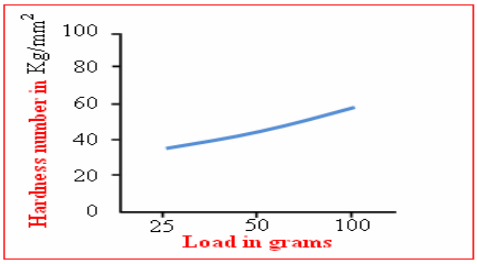

Fig.4 Vicker's Micro hardness of grown crystals

Conclusion

The slow evaporation technique is used to grow natural amino acid of Aloe Vera added KDP (ANAKDP) single crystals. Aloe Vera amino acid extract is taken from the three years old plant leaf. The High performance liquid chromatography (HPLC) is used to analysis the amino acids present in the extract. The unit cell parameters of the grown crystals are determined by single crystal XRD and are compared with the results obtained by Powder XRD data and the peaks are indexed by the computer programme. TJB Holland SATRED FERN 1995. The thermal properties of the sample are studied from TGA, DTA and DSC thermo grams. The presence of amino acids in the grown crystals is qualitatively confirmed by thin layer chromatography (TLC). Its mechanical properties are understood by micro hardness studies.

Acknowledgements

The authors are thankful to M.K. University, Madurai for their help extended in getting single crystal X-ray diffraction results. The support rendered by St. Josephs' college, Trichy, India; Gowri Biotech Private limited, Thanjavur, India; Central Electrochemical Research Institute, Karaikudi, India; Sastra University, Thanjavur, India in our research work are also full heartedly acknowledged.

References

[1] M.A. Bader, H.M. Keller, G. Marowsky, Opt. Mater., 9 (1998) 334.

[2] C. Ramachandra Raja, K. Ramamurthi, R. Manimekalai, Spectrochimca Acta Part A: Molecular and Biomolecular Spectroscopy. 99(2012) 23-26.

[3] Xiue Ren, Xu Dongli, Dongfeng Xue, J. Cryst. Growth 310 (2008) 2005–2009.
[4] Keyan Li, Xingtao Wang, Fangfang Zhang, Dongfeng Xue, Phys. Rev. Lett. 100 (2008) 235504.
[5] N.R. Dhumane, S.S. Hussaini, V.V. Navarkhale, and M. D. Shirsat, Cryst. Res. Technol. 41, 897(2006).
[6] S. Selvakumar, S.M. Ravikumar, K. Rajarajan, A. Joseph Arulpragasam, S.A. Rajasekar, K. Thamizharasan, andP. Sagayaraj, Cryst. Growth Des. 6, 2607 (2006).
[7] C.K. Lakshmana Perumal, A. Arulchakkaravarthi, N.P. Rajesh, P. Santhanaghavan, and P. Ramasamy, Mat. Lett.56, 578 (2002).
[8] V. Kannan, R. Bairava Ganesh, R. Sathyalakshmi, N.P. Rajesh, and P. Ramasamy, Cryst. Res. Technol. 41, 678(2006).
[9] J.J. DeYorea, A.K. Burnham, and P.K. Whiitman, Int. Mat. Rev. 47, 113 (200
[10] S. Uttayakumar, E. Srinivisa, D. P. Paul, D. Prabhakaran, R. Jayaval, C. Subramanian, and P. Ramasamy, PhysicaC 341, 659 (2000).
[11] D.S. Chemla, J. Zyss, in: J.F.Nicoud, R.J. Twieg (Eds), Non-Linear Optical Properties of Organic Molecules and Crystals, Academic Press, London, Volume1 (1987)277.
[12] The essential Aloe Vera, the actions and the evidence by Dr.Peter Atherton, 2 nd edition, 1997.
[13] Aloe vera: A scientific Approach by Robert H Davis, Ph.D., 1997.
[14] Urch, David, Aloe vera Nature′s Gift (Great Britain: Black down Publications, 1999),p-17.
[15] Baker, O.T, The Amazing Ancient to Modern Useful Plant Aloe Vera: Amazing Plant of the Magic Valley, (Lemon Gove, CA: R. Prevost 1975), p.13-16.
[16] A chemical Investigation of Aloe Barbedensis Miller, G.R. Waller, S. Mangiafico and C.R. Ritchey 1978. Proc. Okla. Acad. 58, (1978)69.
[17] Chemical studies of Aloe Vera Juice-Amino Acid Analysis, Gunmar Gjerstad, Advancing frontiers of plant sciences. Vol.28 (1969).
[18] Satyavathi G.V., Medicinal Plants of India, ICMR publications, New Delhi, India.
[19] Lindsay.S, Kealey.D, HPLC. J. Am. Chem. Soc. 110(1988)11.
[20] B. Morosin, G.A. Samara, Ferroelectrics 3(1971)49.
[21] R. Robert, C. Justin Raj, S. Krishnan, S. Jerome Das, Physica B 405(2010)20.
[22] Dongli Xu, Dongfeng Xue, J.Crys.Growth 310(2008) 1385.
[23] Fernando Loretta, T. Josephine Rani, P.Selvarajan, S. Perumal and S. Ramalingom, World Journal of Science and Technology 1(3):01-06(2011), ISSN: 2231-2187.
[24] Tanusri Pal, T. Kar, Xin-Qiang Wang, J. Cryst. Growth, 235(2002)523.
[25] S. Hirota, H. Miki, K. Fukui, K. Maeda, J.Cryst.Growth, 235(2002)541.
[26] Wagner.H, Bladt.S, Plant Drug Analysis, A Thin Layer Chromatography, 384(1996) 45.
[27] Anie Roshan S, Cyriac Joseph, M.A. Ittyachen, Materials Letters, 49(2001)299-302.
[28] K. Srinivasan, P. Ramasamy, A. Cantoni, G. Bocelli, Materials Science and Engineering, B52 (1998)129.

CHARACTERIZATION OF SPRAY DEPOSITED MANGANESE OXIDE THIN FILMS FABRICATED AT TWO DIFFERENT SUBSTRATE TEMPERATURES

D. Vanitha

Assistant Professor, Bon Secours College for Women, Thanjavur

Abstract

Thin films of MnO are well suited for opto-electronic applications, such as solar energy conversion due to its optical and electrical properties as well as its chemical and mechanical stability. MnO thin films were prepared on glass substrate using simple and low-cost chemical spry pyrolysis at different substrate temperature. The MnO films were characterized by X-ray diffraction (XRD), photoluminescence (PL) and ultraviolet-visible (UV-VIS) Optical spectroscopy. The XRD pattern reveals that MnO films possess cubic structure, the average crystallite size was 26.509nm. Photoluminescence activity of the sample was carried out. The optical band gap was calculated and compared to the band gap energy determined from the optical transition involved in the material and is found to be 2.33eV.

Key words: *Manganese oxide, Spray pyrolysis, XRD, Bandgap, PL spectra*

1. INTRODUCTION TO MANGANESE OXIDE THIN FILMS

Manganese oxide (MnO) is a transitional material having interesting physical and chemical properties. It has triggered opto-electronic applications. It is used as electrode materials, electrochemical capacitors, rechargeable batteries, catalysts, sensors, magneto electronic devices MnO was used as a substrate in the synthesis of magnetic oxide perovskite compounds, which have a variety of electrical and magnetic properties like metal-insulator transistors and a colossal magneto resistance. Manganese Oxide is transition metal oxide. Cubic Mn_2, tetragonal Mn_3O_4 and cubic MnO structures could be obtained from MnO_2 by varying the post annealing conditions. Among these oxides, MnO_2 is most stabe. Such varieties in their structures and hence in physical properties and technological applications. Manganese can hold a number of oxidation states, +2, +3, and +4 being the most common for the oxides. Nominal compositions of such phases are MnO, Mn_3O_4, Mn_2O_3, MnO_2 but non stoichiometry has been observed for some these phases. Moreover, except for MnO, two or more crystalline modifications are known for each composition. Several of the MnO_2 phases need the presence of foreign components such as hydroxide, water or on alkali constituent in order to be formed. All manganese oxides are semiconductors, the lowest resistivity being found at the MnO_2 composition. Manganese dioxide is successfully used as a layer material in tantalum thin film capacitors. It is furthermore used as catalyst for oxidation of hydrocarbons, oxidation and reduction of nitric oxide, and decomposition of ozone. Moreover it has interesting electro chromic properties, but most conmmonly manganese dioxide is used in batteries.

1.1. PROPERTIES

MOLECULAR FORMULA	MNO
Molar mass	70.9374g/mol
appearance	Green crystals or powder
Density	5.43g/cm^3
Melting point	195℃, 2218K, 3533℉
Solubility in water	Insoluble
solubility	Soluble in acid
Refractive index	2.16
Crystal structure	Halite (cubic0, CF8
Space group	Fm3m, No.225
Coordination geometry	Octahedral (Mn^{2+}), Octahedral (O^{2-})

1.3. CRYSTAL STRUCTURE

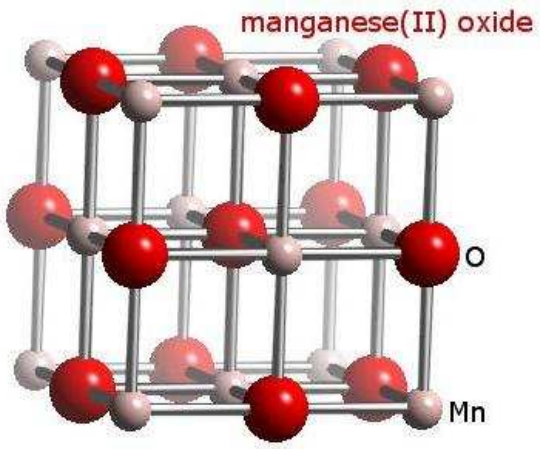

MnO has the NaCl, rock salt structure, where cations and anions are both octahedral coordinated. The composition of MnO can vary from MnO to $MnO_{1.045}$. Below 118k MnO is antiferromagnetic. MnO has the distinction of being one of the first compounds to have is magnetic structure determined by neutron diffraction in 1951. This study showed that the Mn^{2+} ions form a face centred cubic magnetic sub-lattice where there are ferromagnetically coupled sheets which are antiparallel with adjacent sheets.

1.4. APPLICATIONS

1. Manganese Oxide is a component of fertilizer and feed additives. Many thousands of tons are consumed annually for this purpose.
2. A Catalyst in the manufacture of allyl alcohol, ceramics, paints, coloured glass bleaching tallow and textile printing.
3. MnO has triggered Opto-electronic applications.
4. MnO is added to Electrode materials, Electro chemical capacitors, Rechargeable batteries, Catalysts, Sensors, Magneto-electronic devices.
5. Manganese dioxide is successfully used as layer material in tantalum thin film capacitors. Moreover it has interesting electro chromic properties, but most commonly manganese dioxide is used in batteries.

1.5. SPRAY PYROLYSIS TECHNIQUE

Thin films are of increasing interest owing to their numerous applications in all kinds of scientific, industrial and technological applications. For this reason, there are always growing and urgent needs to find new, economical and simple techniques to prepare thin films. Also, a specific need appears for methods of preparation of thin films with large areas used in photovoltaic applications. To respond to this need, several workers have worked in recent years on the preparation and characterization of the thin oxide films. The monoxides are very difficult to evaporate, because of their high melting temperature. To overcome this problem, several techniques were developed for films of such compounds. Among these techniques, the spray pyrolysis technique seems to be more suited for the commercial fabrication of materials of this kind.

Spray pyrolysis has been developed extensively by Chamberlin and co-workers [5]. After that many research articles and review articles related to spray pyrolysis processing and the range of thin films deposited by this method for various applications have appeared. Recently a comprehensive review of all possible thin film materials that could be deposited by spray pyrolysis technique for various applications has been published [6]. Amongst all the deposition techniques to coat thin films, spray pyrolysis is simple, quick, economical and suitable method for large area deposition for many binary and ternary semiconducting thin films. The growth can easily be controlled by preparative parameters such as spray rate, substrate temperature, concentration of solution, nozzle frequency, etc. distribution of droplets the spray cone mainly depend on the geometry of the spray nozzle.

SUBSTRATE TEMPERATURE EFFECT

Since the dynamics of the evaporation and pyrolytic reactions are strongly temperature-dependent process, the substrate temperature has the most significant effect on the quality of the films. The role of the substrate temperature on film formation and microstructure are

investigated by Viguie et al. Films grown at lower temperature are amorphous, whereas deposited at higher temperature are polycrystalline.

Usually slow reactions at lower temperatures would yield foggy and diffusively scattering films. High substrate temperature yield thinner, continuous and hard films. At still higher temperature, re-evaporation of anionic species may take place, resulting in metal rich deposits. Clearly, if the deposition conditions are not optimum, obtained films are powdery, non-adherent and low dense.

SUBSTRATE EFFECT

Neutral surfaces are not taking part in pyrolytic reactions and the choice of such surface is limited to glass, quartz, ceramics, oxide/nitride/carbide coated substrate, Ge, Si, etc. Oxide films on Si sometimes induce etching and in general, deposition of coherent films on metallic substrate is difficult. Even if the substrate is chemically inactive, it may contain mobile alkali and other rare earth ions, which will be readily incorporated in the film.

FILM COMPOSITION

Film composition is expected to depend on the kinetics of the spray process and the thermodynamics of the pyrolytic processes. Incomplete pyrolytic reactions yield intermediate compounds, which is trapped as impurity in the film. The impurity concentration decreases with increasing substrate temperature during pyrolysis. For chloride salts, addition of HCl to the solution has been found to reduce the chlorine content in the film. The conductivity of TO film is attributed to the multivalency tin ions and/or chlorine ions. The deviation from stochiometry is controlled by the water and alcohol content in the spray solution. Water molecules provide oxygen and alcohol acts as a reducing agent. Use of a carrier gas does not seem to affect the concentration of incorporated oxygen vacancies.

PARAMETERS AND FILM QUALITY

The preparation parameters involved in this spray method are many, whose interaction or even existence is sometimes difficult to access. The spraying method involves the decomposition of a mineral compound such as tin chloride penta hydrate or indium chloride dissolved in a solution of water and alcohol. Water is used as an oxidizing agent. The most important parameters of preparation are the nature and the temperature of the substrate, the time of deposition, the composition of the solution to be sprayed and the gas flow rate.

CARRIER GAS PRESSURE

The carrier gas is used to atomize the solution into fine particles. Higher pressure yields fine particles increasing which can produce mist of the particles. By controlling the pressure, the required size could be obtained but to have uniformity in the size, corona spray should be adopted. This pressure also affects the substrate temperature and hence to be optimized.

NOZZLE-SUBSTRATE DISTANCE

Heterogeneous reaction is critically decided by this parameter. Closer to the substrate will lower the substrate temperature resulting to powdery deposits. The area of spray increases as this distance increases but not constantly. The flow rate and compressed air pressure will also affect the area along with this parameter.

THE SOLUTION AND ITS CONCENTRATION

Higher concentrations of the solution will yield most powdery deposits. There is a chance of the nozzle to be blocked when the hotness of the substrate reaches it at lower flow rates. Lower concentrations will alter the substrate temperatures and hence to be optimized. The stochiometry of the film formed depends completely on the concentration and its ratio of the various species in it.

Other parameters like nozzle diameter, the type of carrier gas, and rate of flow of the solutions, time of spray and the volume of the solutions also affect the film and its quality. The texture of the films, its transparency and the thickness could be controlled by controlling these parameters.

PRESENT WORK

In this work Manganese oxide thin films were deposited onto glass substrates using Manganese acetate as the precursor salt. Films were coated at two different substrate temperatures of 200℃ and 225℃ respectively. This films were characterized structurally, morphologically, electrically and optically to bring their active properties towards the fabrication of various applications

2. THIN FILM CHARACTERIZATION TECHNIQUES

2.1. THICKNESS MEASUREMENT

Thickness plays an important role in the film properties unlike bulk materials and almost all the properties of the films are thickness dependent are Reproducible properties are achieved one when the film thickness and the deposition parameters are kept constant.

PROFILOMETER (STYLUS TECHNIQUE)

It measures the height of a step from the substrate surface to the film surface step is formed by masking during deposition. Stylus scans length of several centimeters with a resolution of less than 0.2 microns and measures height of greater than 100Å. Sensitivity of the apparatus depends on surface roughness, flatness, and abruptness of the step.

2.2 WEIGHT GAIN METHOD

This method depends on the increase in weight of a film due to its mass increase. From the knowledge of its density and the deposited areas, film thickness (t) can be calculated from the relation

$$T = (w2-w1)/\varrho A$$

Where,

W1 is the weight of the substrate before coating,

W2 is the weight of the substrate after coating,

A is the deposited area of the film

Thickness is the most important film parameter, which controls the film properties. Hence, precise knowledge of the film thickness is necessary for the intensive study of the properties of thin films. Wide varieties of methods are available for measuring thin film thicknesses. Some of the thickness measurement methods available are Stylus profilometry, multiple beam interferometry, ellipsometry, spectrometry, x-ray microanalysis, microgravimetry and cross-sectional scanning electron microscopy (SEM). Complete information about merits and demerits of these methods, measuring range and accuracy can be found in any of the literature [60-62]. Piegari and Masetti [63] have made qualitative comparison of the available techniques [64-66]. The type of deposit, deposition technique and the nature of the substrate dictate the choice of the method.

The Mitutoya surf test SJ-301 is a stylus type surface roughness and thickness-measuring instrument. It can be used to measure the thickness of thin film coatings on any uniform surface. The stylus of the SJ-301 detector unit traces the minute irregularities of the vertical displacement of the fine needle, when the detector traversing over the film surface irregularities. For measuring film thickness, the stylus is placed over the uncoated surface and made to move towards the coating. Then it steps over the coating surface and moves over it. The vertical displacement gives the thickness of the coating. The thicknesses of the prepared thin film samples were found using this instrument. It is a non-destructive technique and the coatings may be used for further studies without any damage. The picture of the device along with the stylus is shown in Fig. 3.2 and their technical specifications are listed below:

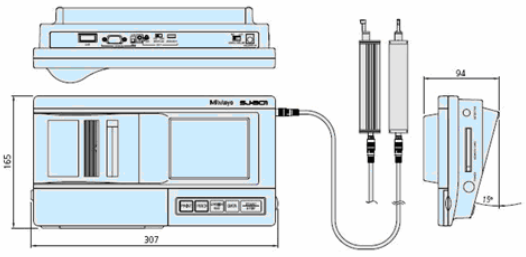

Fig 3.2 External view of the surface profiler SJ-301

Model number	: SJ-301 4 m N type
Measuring range x-axis	: 12.5 mm
z-axis	: 350 μm
Measuring speed	: 0.5 mm/s
Stylus tip radius	: 5 μm
Stylus tip material	: Diamond

Measuring force : 4 mN
Detecting method : Differential inductance
Recording magnification : x10-1,00,000

2.3. TWO PROBE TECHNIQUE

In this technique, a constant current 'I' is passed through two aluminium strip contacts separated by a distance 'd' and the voltage 'V', between these strips is measured by using a high impedance voltmeter as shown in Fig. 3.3. For a thin film sample of thickness 't' and breadth 'b' placed between these two aluminium strips, the resistivity is derived from the following equations given by:

Resistance $R = \frac{V}{I}$ (3.1)

Resistivity ρ=R x (Cross sectional area/Length)

$$\rho = \frac{V}{I}\frac{t}{l}b \ \Omega cm \quad (3.2)$$

In thin film technology, the ratio between the resistivity of the film material to the thickness of the thin film specimen 't' is termed as sheet resistance 'R_{sh}' and thus:

$$R_{sh} = \frac{V}{I}\frac{b}{l} \ \Omega/ \quad (3.3)$$

Hence, for a square specimen l = b, the resistance of one square of a film is its sheet resistance R_{sh}, which is independent of the size of the square but depends only on resistivity and film thickness. In such case:

$$\rho = R_{sh}\, t \ \Omega cm \quad (3.4)$$

Further, the activation energy can be calculated from the measured resistivity of the sample. Activation energy measures the thermal or other form of energy required to raise electrons from the donor levels 'E_d' to the conduction band or to accept electrons by the acceptor levels 'E_a' from the valence band respectively for n and p-type materials and this corresponds to the energy height difference (E_c-E_d) and (E_a-E_v) respectively. On measuring the variation of σ or ρ with temperature, the activation energy E_a can be determined from the slope of the straight line obtained by plotting $\ln(\rho)$ against $\frac{1}{T}$.

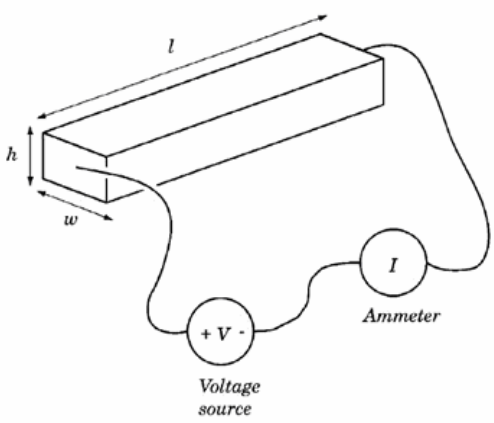

Fig 3.3 Two probe setup

For the present study, the four probe resistivity measurements were carried out on cobalt oxide films using an OSAW AC-DC Four point probe unit, in conjunction with a UNI-INSTA DC power supply. The voltage and current were measured using a HIL 2161 Digital multimeter and a Keithley 2000 multimeter respectively.

2.4. STRUCTURAL CHARACTERIZATION

When high-frequency electromagnetic waves are selected to have a wavelength in the order of interplanar spacing of crystals, they are diffracted according to Bragg's law [16]. The typical inter-atomic spacing in crystal is in the order of 2-10 Å. So, the wavelength of the radiation used for crystal diffraction should be in the same range. X-rays have wavelengths in this range and thus diffracted by crystals. Hence, an excellent experimental verification for the crystal structures can be availed by x-ray diffraction [17]. This method is an important technique for the characterization of thin films, since it gives a very broad range of information about the material such as crystal structure, composition and defects in the films.

In the present work, X-ray diffraction studies were carried out on cobalt oxide thin films deposited at different substrate temperatures. The technical details of the x-ray diffractometer used in the present study are:

Model : X'pert PRO
X-ray source : 1.8 KW ceramic copper tubes

Operation potential : 40 kV, 30 mA
Filter : Nickel
Radiation used : CuK_α - 1.54056 Å
Detector : Xe proportional counter

In this sophisticated diffractometer, diffracted beams are collected by the Xecelator detector, whose output is directly fed into a chart recorder. The beam of the x-ray source is automatically rotated with the help of a motor so that the x-ray beam incident angle can be precisely recorded. The detector, collecting the diffracted beam is mounted co-axially with source rotator and coupled to it in such a way that the source moves through an angle of 'θ', the detector moves through an angle of '2θ', so that it is in the right position to collect the diffracted x-rays from crystalline samples. The chart recorder plots the diffracted x-ray intensity as a function of '2θ'. The plot consists of a series of peaks of different intensities depending on the magnitude of the diffracted x-ray intensity in that direction.

From the XRD pattern one can determine the interplanar spacing (d), lattice parameters and hence the structure of the films. Usually, the diffraction peak positions are compared with the data from JCPDS cards. In the present case, the JCPDS standard data were compared with the obtained cobalt oxide data for fixing the structure of the prepared films.

In general, diffraction peak from a lattice plane is labeled as Miller indices (h k l) and these indices are related to inter-atomic spacing or'd' spacing. For an orthogonal system (i.e., $\alpha = \beta = \gamma = 90^\circ$), the 'd' spacing for any set of planes is given by the formula:

$$\frac{1}{d_{hkl}^2} = \frac{h^2}{a^2} + \frac{k^2}{b^2} + \frac{l^2}{c^2} \qquad (3.19)$$

Where, 'a', 'b' and 'c' are the cell edges.
For hexagonal crystals,

$$\frac{1}{d_{hkl}^2} = \frac{4}{3}\left(\frac{h^2 + hk + k^2}{a^2}\right) + \frac{l^2}{c^2} \qquad (3.20)$$

For tetragonal crystals,

$$\frac{1}{d_{hkl}^2} = \left(\frac{h^2 + k^2}{a^2}\right) + \frac{l^2}{c^2} \qquad (3.21)$$

Using these relations, the Miller indices are assigned for each diffraction peak obtained in a diffractogram.

The width of the diffraction peak depends on the phase of the diffracted rays from each plane. If each plane in a crystal diffracts exactly one wavelength later than the preceding plane, all diffracted beams are in phase and constructive interference occurs, resulting zero peak width. If there is a phase lag of slightly greater than one wavelength $\lambda+\delta\lambda$, for rays diffracted from subsequent planes, a cumulative phase lag $\Sigma\delta\lambda = \lambda/2$ occurs at $(j+1)^{th}$ plane, ie: $j\delta\lambda = \lambda/2$. Then planes 1 and $(j+1)$ are exactly 'π' out of phase for radiations that is incident and diffracted at 'θ_1' and therefore cancel each other. The angular range between the Bragg peak 'θ' to 'θ_1' is the range over which the intensity of the diffracted beam falls from a maximum, at 'θ' to zero, at 'θ_1'. A similar lower limiting angle 'θ_2', occurs for which rays diffracted from adjacent planes have a phase difference of λ-dλ. The magnitude of the angular range 'θ_1' to 'θ_2' and hence the breadth of the diffraction peak, is governed by the number of planes 2j, and hence the crystal thickness. If the number of planes is very large, no significant broadening occurs, because '$\delta\lambda$' and therefore $(\theta_2-\theta_1)$ is negligibly small. The commonly accepted formula for particle size broadening is the Scherrer formula [18]:

$$D = \frac{0.94\,\lambda}{\beta\cos\theta} \qquad (3.22)$$

where, 'D' is the grain size, 'β' is the full width at half maximum (FWHM) of the respective peak, and 'θ' is the corresponding Bragg's angle.

Stress on the deposited film can also be measured from the x-ray diffraction peaks. Due to compressive stress, the whole x-ray diffraction pattern may be shifted to lower d-spacing such that a contraction of unit cell occurs. If the stress is non-uniform, different parts of the film may be deformed to different degrees and the

diffracted lines become broadened. Commonly, both effects occur and lines may be both displaced and broadened. The average internal stress developed in the film is determined by the relation [2]:

$$S = \frac{E}{2\delta}\left(\frac{a_o - a}{a_0}\right) \quad (3.23)$$

where, 'E' is the Young's modulus of the film, 'δ' is the Poisson's ratio of the film, 'a_o' is the bulk lattice constant, and 'a' is the lattice constant of the film.The origin of the strain is also related to the lattice mismatch and may be calculated from the slope of β cosθ vs. sinθ plot using the relation [19]:

$$\varepsilon = \frac{\lambda}{D\sin\theta} - \frac{\beta}{\tan\theta} \quad (3.24)$$

Where, 'D' is the grain size, 'β' is the full width at half maximum of the peak, and 'θ' is the corresponding Bragg's peak.

The dislocation density 'δ' ie, the dislocation lines per unit area of the crystal can also be evaluated from the grain size 'D' using the formula [20]:

$$\delta = \frac{1}{D^2}\text{ lines} / \text{m}^2 \quad (3.25)$$

Also using grain size 'D' and film thickness 't', number of crystallites 'N' has been estimated using the relation:

$$N = \frac{t}{D^3} / \text{ unit area} \quad (3.26)$$

2.5. OPTICAL CHARACTERIZATION

In early days, the study of the interactions of light with matter laid the foundations for quantum theory. Today, optical methods are among the most important tools for elucidating the electron structure of matter. Among the many available tools, spectrophotometer, photoluminescence spectrometer and Raman spectrometer are used to explain all the possible transitions such as band-to-band, exactions, between sub bands, between impurities and bands. In addition, the transitions by free carrier within a band and the resonances due to vibrational states of the lattice and of the impurities can be understood.

2.6. UV-Vis-NIR spectrophotometer

The measurement of transmission or reflection of a sample provides a satisfactory way to determine the form of the absorption edge. The absorption edge and energy band gap can be determined from the transmission measurement [21]. Hence, the optical transmittance properties of the films are analyzed with the Hitachi-3400 UV-Vis-NIR spectrophotometer. Technical specification of the instrument is listed below.

Model : Hitachi-3400 (double beam)
Wavelength range: 200 – 2500 cm^{-1}

When light radiation is incident on a thin film material with energy equal or greater than that of the band gap, absorption of photons can take place and electrons are raised in energy from the valance band to the conduction band, creating electron-hole pairs. The ability of a material to absorb photons of a given wavelength is measured quantitatively by the optical absorption co-efficient (α), measured in units of reciprocal distance [22].

$$\alpha(\lambda) = \frac{1}{t}\ln\left\{\frac{\left[1 - R(\lambda)\right]^2}{T(\lambda)}\right\} \quad (3.27)$$

where, 't' is the film thickness, 'R' and 'T' are the reflection and transmission co-efficient respectively.

There are two major types of intrinsic absorption processes involved in determining α, they are the direct and indirect absorption. As a general rule, the larger the band gap, the smaller is the value of 'α' for a given wavelength but absorption co-efficient also depends on the density of states in the conduction and valence bands. The optical absorption co-efficient is related to energy band gap and it is given by the following equation [23]:

$$\alpha h\nu = B\,(h\nu - E_g)^n \quad (3.28)$$

Where, 'B' is a constant and 'E_g' is the optical band gap. For crystalline materials, the exponent n is 1/2, 3/2, 2 and 3, when the transition is direct allowed, direct forbidden, indirect allowed and indirect forbidden respectively. Apparently, the plot of $(\alpha h\nu)^2$ or $(\alpha h\nu)^{1/2}$ against (hν) provides the nature and 'E_g' value of a particular film. The magnitude of 'n' can be estimated

from the slope of the graph of log (α) vs. (hν) and hence can suggest the type of transition. The direct optical absorption is illustrated in Fig. 3.5.

Direct optical absorption is a first order process, involving only the absorbed photon and can be represented approximately as a vertical line on the energy versus wave vector (k) plot. The absorption transition conserves energy so that $\Delta E = h\nu$ and there is no change in 'k' between initial and final states except for the small momentum of the photon. An indirect optical transition is a second order process involving both the absorbed photon and a simultaneously absorbed or emitted phonon, which occurs when the minimum of the conduction band and the maximum of the valence band occur at different values of the wave vector 'k' as illustrated in Fig. 3.6.

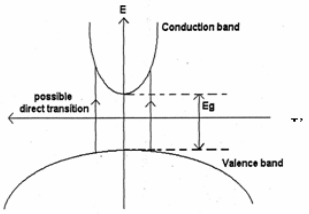

Fig 3.5 Direct transition from valence band to conduction band

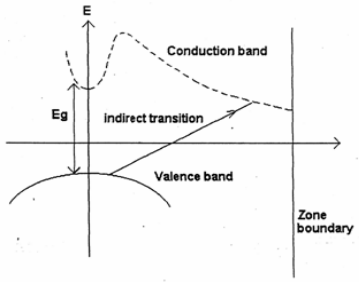

Fig 3.6 Indirect transition from valence band to conduction band

Here the absorption transition conserves energy by requiring $\Delta E = h\nu + E_p$ where, 'E_p' is the photon energy and the change in 'k' between the initial and final states 'Δk' is just equal to the value of 'k' of the phonon involved.

2.7. SURFACE MORPHOLOGICAL STUDIES

Scanning probe microscopes (SPM) are very different from optical microscopes in the sense that they operate with an extremely small probe tip, barely touching the surface, sensing different properties at close to atomic resolution in all three dimensions. Both the scanning electron microscopy as well as atomic force microscopy has been used in the present work for the surface morphological studies.

Scanning Electron Microscopy (SEM)

To study the surface morphology of thin film samples, the reflection mode of the optical microscope can be used. But this technique is limited in spatial resolution to a few tens of a millimeter. Very high resolution is required in electron beam technique. The most versatile among these is the scanning electron microscope. The main components of the instrument and the optical system are shown schematically in Fig. 3.7.

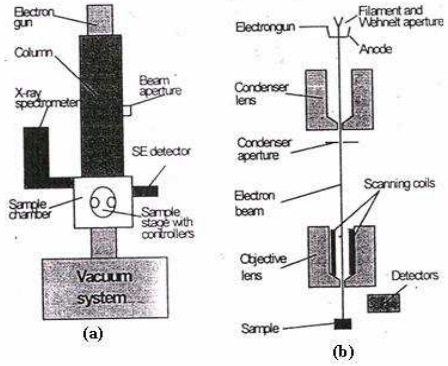

Fig 3.7 Main component of SEM together with optical system

An electron beam is generated by an electron gun at the top of the column. This beam is focused by two magnetic lenses inside the column and strike the sample in the sample chamber in a very small spot. When these electrons penetrate into the sample, some electrons are scattered back out of the sample and are collected by a suitable detector. These electrons are used to obtain information on the mean atomic number in the part of the sample from which they originated, relative to other part. Secondary electrons with very low energy also be released and are used to obtain information on the topography of the sample.

Usually, the electron beam is not left stationary on the sample, but scans across certain area in a raster pattern. The signal from one of the detector is selected and used to modulate the intensity on a viewing screen, which is scanned synchronously with the primary beam in the column. Thereby an image

is generated on the viewing screen with high brightness in areas with a strong signal from the detector, and darker areas where weak signals are detected. In this way, an enlarged image of the sample is obtained on the screen. To vary the magnification, the size of the scanned area of the sample is varied while the scanning width on the viewing screen is constant. The scanned image is particularly useful for examining the morphology of thin films of semiconductors, insulators and crystalline materials as well. Electrically insulating samples usually have to be given a conducting coating. In the present study, HITACHI Model S-3000H model is used, which is capable of taking magnified pictures of solid, dry, conducting and non-conducting specimen. Its technical specifications are listed below.

Model number : HITACHI Model S-3000H
Scanning probe diameter : 20 Å
Resolution : 60 Å at 30 kV
Magnification : 20 – 65,000
Voltage : 1 kV – 39 kV
Required specimen size : 5 x 5 mm^2 with 1 mm thickness

Using this instrument, SEM studies have been carried out to identify the morphology of the deposited oxide films. The SEM micrographs provide the nature of the surface (uniformity, smoothness and cracks) and the nature of the grains (Shape, particulate and grain size) [24].

3. RESULTS AND DISCUSSION

Thin films of manganese oxide are suited for Opto electronic applications. Such as solar energy conversion due to its optical and electrical properties as well as its chemical and mechanical stability.

Manganese oxide can exist in a number of oxidation such as +1,+2,+3 and +4. It can also easily change its oxidation state. This ability to accept or donate electrons has to led to many applications in MnO in catalysts, Li ion battery technology, electronic and magneto properties of Manganese oxides are also important for colossal magneto resistance effects.

All the manganese oxides are semi conductors, the lowest resistivity being found at the MnO composition. Generally resistivities of MnO fall in the range 1000 to 0.1Ω cm.

3.1. FILM DEPOSITION

Manganese acetate was used as the precursor salt for preparing thin films 0.05M of manganese acetate was dissolved in 40ml of de-ionized water. Few drops of acetic acid were added to a clear solution. Then the solution was sprayed on to preheated glass substrates at 200ºC and 225ºC respectively pyrolytic decomposition of the solution takes place and blackish colored films of manganese deposited on the substrates.

3.2. THICKNESS MEASUREMENT

Thickness plays an important role in the film properties. Unlike bulk material and all the properties of the films are thickness dependent. Reproducible particle are achieved only in the film thickness and deposition parameter are kept constant Thin film manganese oxide are suited for opto electronic applications.

WEIGHT GAIN METHOD

This method depends on the increase the increase weight of the films are due to mass increased. From the knowledge of its density and deposited area films thickness (t) can be calculated from the relation

$$T = (w_2 - w_1)/\varrho A$$

The film thickness was found to be equal to 0.043μm and 0.274μm for the films coated at 200ºC and 225ºC respectively. It was observed that as the substrate temperature increases the film thickness increases.

3.3. XRD STUDIES

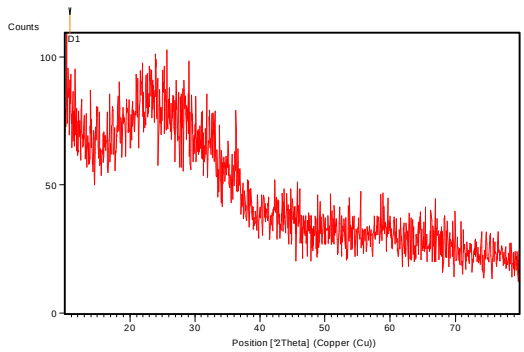

Fig (a)

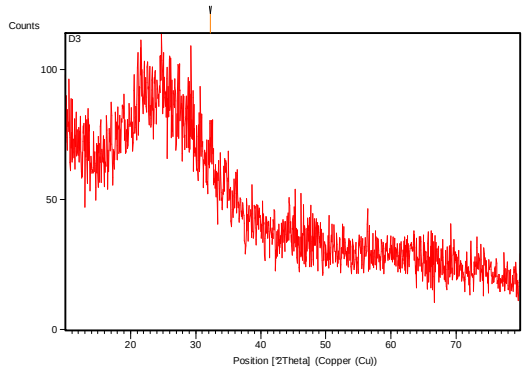

Fig(b)

Fig(a,b) shows the XRD patterns of MnO films coated at 200ºC and 225ºC.

The XRD patterns showed that the films are amorphous in nature without any peak being observed. This is the nature of MnO thin films coated at low substrate temperatures.

3.4. MORPHOLOGICAL STUDIES SCANNING ELECTRON MICROSCOPY

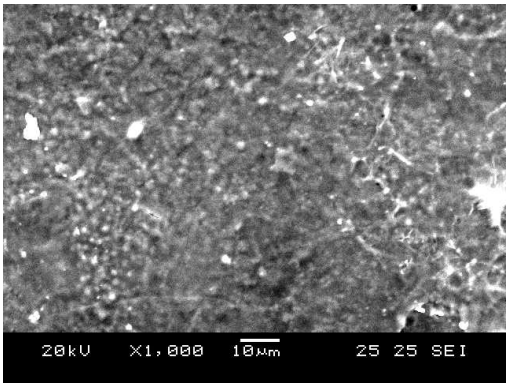

Fig(a)

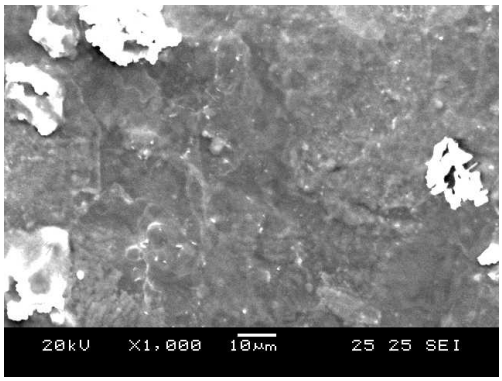

Fig(b)

Fig(a,b) shows the MnO thin films coated at 200ºC and 225ºC respectively. No grains were observed for the film coated at 200ºC, with small patches on the film surface. For film coated at 225ºC, clusters of small grains were observed and patches being minimized, which might be due to increased temperature.

3.5. ATOMIC FORCE MICROSCOPY

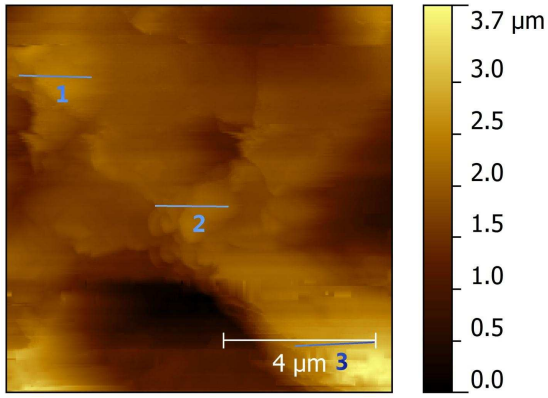

Fig(a)

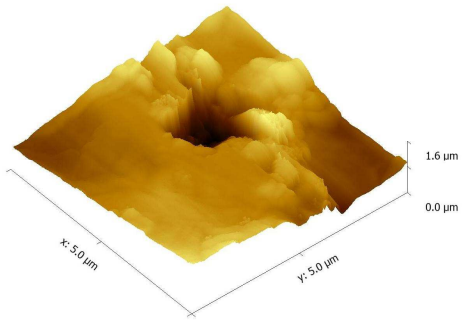

Fig(b)

Fig (a,b) shows the thin films coated at 200ºC and 225ºC respectively. No grains were observed for the film coated at 200ºC with small patches on the film surface. For film coated at 225ºC, clusters of small grains were observed and patches being minimized, which might be due to increased temperature.

3.5. OPTICAL STUDIES

Fig(a) shows that optical transmission spectrum of MnO films coated at two different substrate temperatures. Film coated at 200ºC have a transmittance of about 52% where as

film coated at 225ºC shows a transmittance nearly equal to 32%. The transmittance increases with the decrease in the substrate temperature which might be due to increased thickness of the films coated with high temperature.

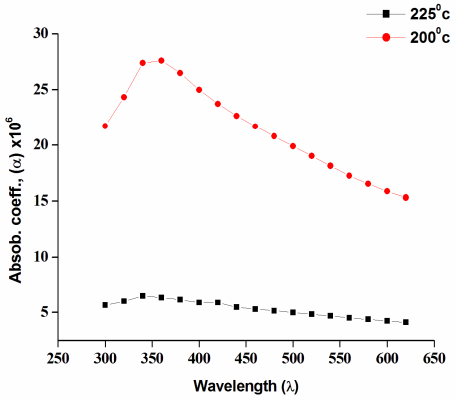

Fig(b)

The variation in α as a function of wave length is shown in fig(b). from the fig it is clear that α increases rapidly with increasing wavelength from 320 to 570nm for 200ºC and 320 to 460nm for 225ºC respectively, after that the value of α remains constant.

Fig(c)

Fig(c) shows the variation of $(\alpha h\gamma)^2$ Vs hγ graph of MnO thin films coated at 200ºC and 225ºC respectively. The bandgap energy of MnO thin films were found to be equal to 2.8eV and 2.3eV for the films coated at 225ºC and 200ºC respectively. The band gap energy increases with increase in substrate temperatures.

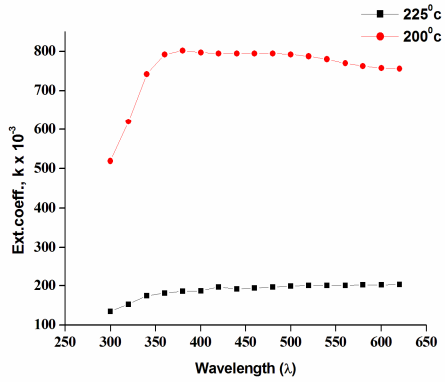

Fig(d)

Fig(d) shows that variation of extinction coefficient with wavelength of MnO thin film from the graph it is observed that the variation of K is similar to that of absorption coefficient α.

3.6. ELECTRICAL STUDIES

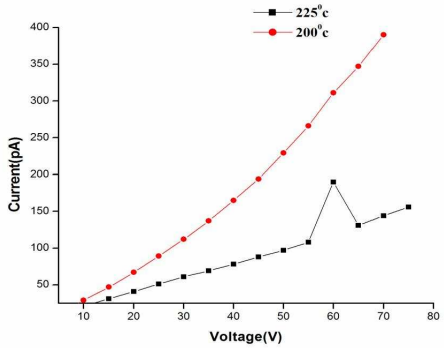

Fig(a)

The V-I characteristics curves of MnO thin films prepared using two different substrate temperatures is shown in fig(a). For both films current decreases with increases in voltage. The conductivity value decreases from 6.04 x 10^{10} to 2.08 x 10^{10} mho as temperature increases from 200ºC to 225ºC.

4. CONCLUSION

Manganese oxide thin films were prepared by spray pyrolysis technique at two different substrate temperatures. The films were slightly blackish in color. The coated films were characterized by XRD, SEM and Optical absorption studies showed that films were amorphous with low intensity peaks, and patches being minimized, which might be due to increased temperature. Optical sorption studies shows that the films coated has a transmittance of nearly equal to 52%where as the films coated transmittance of nearly equal to 32%, and the Bandgap energy of MnO films were found to be 2.3ev for films coated at 225º and 200º temperature respectively. The electrical studies showed that conductivity value decreases with increase in temperature.

REFERENCE

[1] J.CZ. Nardi, J. Electrochem. Soc.132, 1787 (1985).

[2] L. Sanchez, J. Faray, J.P. Pereira-Ramos, L. Herman, J. Morales, L. Tirado, J. Mater. Chem.6, 37 (1996).

[3] R.N. Reddy, R.G. Reddy, J. power source. 132, 315 (2004).

[4] R.N. Reddy, R.G. Reddy, Electrochemical capacitor and hybrid powder sources, in: Brodd RJ, et al., (Eds), the electrochemical society proceeding series, PV 2002-7 Pennington NJ, 197 (2002).

[5] C-N Xu, K. Miyazaki, T. Watanable, Sensors and Actuators B 46,87 (1998).

[6] K.J. Kim, Y.R. Park. J.Cryst. Growth 270, 162 (2004).

[7] C.N. R. Rao, A.K. Cheetham, Adv. Mater. 9, 1009 (1997).

[8] R. Von Helmolt, J. Weeker, B. Holzapfel, L. Schultzl, K. Samwer, phys. Rev. Lett. 71, 2331 (1993).

[9] M. Regulski, R. Prezenioslo, L. Sosnowska, D. Hohlewein, R.S. Schneider, J. Alloy. Comp.362, 236 (2004).

[10] P.Fau, J.P. Bonino, A. Rousset, Appl. Sci. 78, 203 (1994).

[11] R.M. Vaalletta, W.A. Pliskin, J. Electrochem. Soc. 114, 944, (1967).

[12] T.Seike, J. Nagai, Sol. Energy Mater. 22, 107 (1991).

[13] H.Yang, H. al-Brithen, A.R. Smith, J.A. Borchers, R.L. Cappelletti, M.D. Vaudin, Appl Phys. Lett. 78, 3860 (2001).

[14] O. Nilsen, H. Fjellvag, A. Kjekshus, Thin Solid Films 444, 44 (2003).

[15] S.A. Chhamblers, Y. Liang, Surf. Sci. 123, 420 (1999).

[16] L.W. Guo. H. Makino, H.J. Ko, Y.F. Chen, T. Hanada, D.L. Peng, K. Inaba, T. Yao, J. Cryst Growth 955,227 (2001).

[17] M. Chigane, M. Ishikawa, J. Electrochem. Soc. 148, D96 (2001).

[18] A.K.M. Farid UI Islam, R. Islam, K.A. Khan, Renew. En. 30, 2289 (2005).

[19] R.M. Valletta, J. Makris, W.A. Pliskin, Proc. Electron. Compon. Conf. 16, 31 (1966).

[20] K. Wang Joo Kim, Young. Ran Park, J. Crystal Growth 270, 162 (2004).

[21] Y.J. Park, J.G. Kim, H.T. Chung, H.G. Kim, Solid State Ionics 130, 203 (2000).

[22] R.W. Landrof, S.J. Licht, J. Electrochem. Soc. 114 (1967) 944.

[23] R.M. Valletta, J. Makris, W.A. Pliskin, Proc. Electron. Compon. Conf. 16 (1966) 31.

[24] J. Ma, G.K. Chuah, S. Jaenicke, R.Gopalakrishnan, K.L. Tan, Ber. Bunsen-Ges. 100 (1996) 585.

[25] R. Cracium, N. Dulamita, Catal. Lett. 46 (1997) 229.

[26] L. Singoredjo, R. Korver, F. Kapteijn, J. Moulijn, Appl. Catal. BI (1992) 297.

[27] L.Chen, T. Horiuchi, T. Mori, Catal. Lett. 60 (1999) 237.

[28] S.T. Oyama, Catal . Rev.-Sci. Eng. 42 (2000) 279.

[29] T. Maruyama, Y. Osaki, J. Eectrochem. Soc. 142 (1995) 3137.

[30] F. Garnich, P.C. Yu, C.M. Lampert, Sol. Energy Mater. 20 (1990) 265.

[31] L.D. Burke, O.J. Murphy, J. Electroanal. Chem. 109 (1980) 373.

[32] B.A. Lopez de Mishima, Ohtsuka Toshiaki, Sato Norio, J. Electroanal. Chem. 243 (1988) 219.

[33] S.I. Coroda de Torresi, A. Gorenstein, Electrochim. Acta 37 (1992) 2015.

[34] T. Seike, J. Nagai, Sol. Energy Mater. 22 (1991) 107.

[35] D. Boden, C.J. Venuto, D. Wisler, R.B. Wylie, J. Electrochem, Soc. 114 (1967) 415.

[36] J. McBreen, Electrochim. Acta 20 (1975) 221.

[37] [a b c d e]Greenwood. Narman N; Earnshaw, Alan (1997). Chemistry of the Elements (2nd ed.). Butterworth – Heinemann. ISBN 0-471-93620-0.

[38] J.E. Greedom, (1994), Magnetic oxides in Encyclopedia of Inorganic Chemistry Ed. R. Bruce King, John Wiley & Sons ISBN 0-471-93620-0

[39] Neutron Diffraction by Paramagnetic and Antiferromagnetic Substances C.G. Shull, W.A. Strauser, and E.O. Wollan, Phys. Rev. 83,333-345 (1945), doi:10.1103/physRev.83.333.

STUDIES ON ZINC DOPED CADMIUM OXIDE THIN FILMS PREPARED BY SPRAY PYROLYSIS TECHNIQUE

V. Rathna

Assistant Professor, Bon Secours College for Women, Thanjavur.

Abstract

Znx Cd1-xO thin films were prepared on glass substrates by spray pyrolysis technique. The precursor solutions were obtained by varying the concentration of Zn(NO3)2.6H2O and Cd(NO3)2. 4H2O in bi-distilled water. The structural properties have been studied using X-ray diffraction spectra. All the structures include the basic compounds, i.e. ZnO and CdO. The orientation and the crystalline phases of the deposited films were specified. With the addition of Zn to the precursor solution, we can observe the preferential orientation of the CdO in the [200] direction. The electrical measurements were performed using method of four contacts. Thin films transmittances, in the 1.5-4.3eV range, for different compositions have been measured and the oprical gaps have been determined. The variations are explained considering the gaps of the two pure films. The influence of increased Cd concentration in the films on the structural, electrical and optical properties is investigated in this study.

Key words: *Thin films; Spray pyrolysis; Zinc oxide; Cadmium oxide; Optical; Electrical Properties.*

INTRODUCTION TO CADMIUM OXIDE THIN FILMS

Cadmium oxide (CdO) is an important semiconductor material for the development of various technologies of solid state device, (panel display, optoelectronic, components, thermally insulating glass, etc)[1-3].CdO films show a high transparency in the visible region of the solar spectrum, as well as high ohmic conductivity. the intensity of optical and electrical effects of Cdo depends on the derivation from the ideal CdO stoichiometry, as well as on the size and shape of the particle [4].bulk cdo is an n-type broad bandgap (2.3ev) semiconductor, with an indirect bandgap of1.36ev [5]. Cadmium oxide (CdO) is one of the promising transparent conducting oxides (tco) from ii to vigroup of semiconductors having high absorption and emission capacity of radiation in the energy ga [6.thin films of co have bee used in wide variety of applications such as photodiodes [7], phototransistors [8], photovoltaic cell [9], transparent electrodes [10], liquid crystal displays, IR detectors and anti reflection coatings [11]. Cadmium and Zinc oxides and many others are transparent conducting oxides (TCO), which continue to attract attention in many solar cells and optoelectronic applications. Both are n-type semiconductor components [12]. In particular, zinc oxide is a promising material as gas sensor [13-16] varistors [17,18] and due to its large bandgap (of 3.3eV), it is evidently used as an active window component of photovoltaic hetrojunction thin film solar cells (TFSCO) [19,20]. In this role, it could directly combine the function emitter with that of a conducting layer. This is the concept of absorber material like CuInSe2 (CIS) thin film cells [21,22]. Its bandgap is wide enough to transmit most of the useful solar radiation in solar cells [23].

STRUCTURE

Cadmium oxide is an inorganic compound with the formula CdO. It is one of the main precursors to other cadmium compounds. It crystallizes in a cubic rocksalt lattice like sodium chloride, with octahedral cation and anion centers. [24] It occurs naturally as the rare mineral monteponite. Cadmium oxide can be found as a colorless amorphous powder or as brown or red crystals. [25]Cadmium oxide is an n-type semiconductor [26] with a band gap of 2.16 eV at room temperature [27].

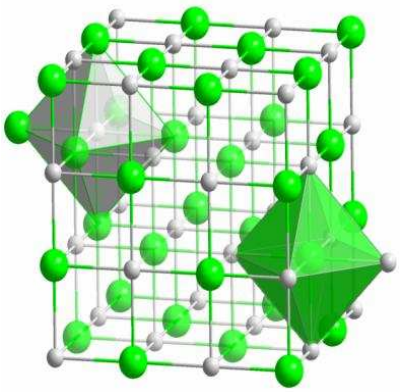

PROPERTIES

Molecular formula	CdO
Molar mass	128.41 g mol^{-1}
Appearance	Colorless powder (alpha form) red-brown crystal (beta form) [1]
Odor	Odorless
Density	8.150g/cm^3(crystalline), 6.95 g/cm^3 (amorphous)[2] solid.
Melting point	900–1000 °c (decomposition of amorphous
Boiling point	1559 °c, 1832 k, 2838 °f (sublimation[3])
Solubility in water	Insoluble
Solubility	Soluble in dilute acid slowly soluble in ammonium salts insoluble in alkalies
Band gap	2.5 ev
Electron mobility	531 cm^2/vs
Magnetic susceptibility	-3×10^{-5} cm^3/mol
Thermal conductivity	0.7 w/m-k

SPRAY PYROLYSIS TECHNIQUE

Thin films are of increasing interest owing to their numerous applications in all kinds of scientific, industrial and technological applications. For this reason, there are always growing and urgent needs to find new, economical and simple techniques to prepare thin films. Also, a specific need appears for methods of preparation of thin films with large areas used in photovoltaic applications. To respond to this need, several workers have worked in recent years on the preparation and characterization of the thin oxide films. The monoxides are very difficult to evaporate, because of their high melting temperature. To overcome this problem, several techniques were developed for films of such compounds. Among these techniques, the spray pyrolysis technique seems to be more suited for the commercial fabrication of materials of this kind.

Spray pyrolysis has been developed extensively by Chamberlin and co-workers [5]. After that many research articles and review articles related to spray pyrolysis processing and the range of thin films deposited by this method for various applications have appeared. Recently a comprehensive review of all possible thin film materials that could be deposited by spray pyrolysis technique for various applications has been published [6]. Amongst all the deposition techniques to coat thin films, spray pyrolysis is simple, quick, economical and suitable method for large area deposition for many binary and ternary semiconducting thin films. The growth can easily be controlled by preparative parameters such as spray rate, substrate temperature, concentration of solution, nozzle frequency, etc. distribution of droplets the spray cone mainly depend on the geometry of the spray nozzle.

SUBSTRATE TEMPERATURE EFFECT

Since the dynamics of the evaporation and pyrolytic reactions are strongly temperature-dependent process, the substrate temperature has the most significant effect on the quality of the films. The role of the substrate temperature on film formation and microstructure are investigated by Viguie et al. Films grown at lower temperature are amorphous, whereas deposited at higher temperature are polycrystalline.

Usually slow reactions at lower temperatures would yield foggy and diffusively scattering films. High substrate temperature yield thinner, continuous and hard films. At still higher temperature, re-evaporation of anionic species may take place, resulting in metal rich deposits.

Clearly, if the deposition conditions are not optimum, obtained films are powdery, non-adherent and low dense.

SUBSTRATE EFFECT

Neutral surfaces are not taking part in pyrolytic reactions and the choice of such surface is limited to glass, quartz, ceramics, oxide/nitride/carbide coated substrate, Ge, Si, etc. Oxide films on Si sometimes induce etching and in general, deposition of coherent films on metallic substrate is difficult. Even if the substrate is chemically inactive, it may contain mobile alkali and other rare earth ions, which will be readily incorporated in the film.

FILM COMPOSITION

Film composition is expected to depend on the kinetics of the spray process and the thermodynamics of the pyrolytic processes. Incomplete pyrolytic reactions yield intermediate compounds, which is trapped as impurity in the film. The impurity concentration decreases with increasing substrate temperature during pyrolysis. For chloride salts, addition of HCl to the solution has been found to reduce the chlorine content in the film. The conductivity of TO film is attributed to the multivalency tin ions and/or chlorine ions. The deviation from stoichiometry is controlled by the water and alcohol content in the spray solution. Water molecules provide oxygen and alcohol acts as a reducing agent. Use of a carrier gas does not seem to affect the concentration of incorporated oxygen vacancies.

PARAMETERS AND FILM QUALITY

The preparation parameters involved in this spray method are many, whose interaction or even existence is sometimes difficult to access. The spraying method involves the decomposition of a mineral compound such as tin chloride penta hydrate or indium chloride dissolved in a solution of water and alcohol. Water is used as an oxidizing agent. The most important parameters of preparation are the nature and the temperature of the substrate, the time of deposition, the composition of the solution to be sprayed and the gas flow rate.

CARRIER GAS PRESSURE

The carrier gas is used to atomize the solution into fine particles. Higher pressure yields fine particles increasing which can produce mist of the particles. By controlling the pressure, the required size could be obtained but to have uniformity in the size, corona spray should be adopted. This pressure also affects the substrate temperature and hence to be optimized.

NOZZLE-SUBSTRATE DISTANCE

Heterogeneous reaction is critically decided by this parameter. Closer to the substrate will lower the substrate temperature resulting to powdery deposits. The area of spray increases as this distance increases but not constantly. The flow rate and compressed air pressure will also affect the area along with this parameter.

THE SOLUTION AND ITS CONCENTRATION

Higher concentrations of the solution will yield most powdery deposits. There is a chance of the nozzle to be blocked when the hotness of the substrate reaches it at lower flow rates. Lower concentrations will alter the substrate temperatures and hence to be optimized. The stoichiometry of the film formed depends completely on the concentration and its ratio of the various species in it.

Other parameters like nozzle diameter, the type of carrier gas, rate of flow of the solutions, time of spray and the volume of the solutions also affect the film and its quality. The texture of the films, its transparency and the thickness could be controlled by controlling these parameters.

PRESENT WORK

In this work undoped and Zn doped cadmium oxide thin films were deposited onto glass substrates using cadmium acetate and Zinc acetate precursor salts at 325ºC.Zn doped films were fabricated with 2, 5, 10, wt % of Zn concentration .The films were characterized

structurally, morphologically, electrically and optically to study its effect of Zn on undoped CdO films.

THIN FILM CHARACTERIZATION TECHNIQUES

THICKNESS MEASUREMENT

Thickness plays an important role in the film properties unlike bulk materials and almost all the properties of the films are thickness dependent are Reproducible properties are achieved one when the film thickness and the deposition parameters are kept constant.

PROFILOMETER (STYLUS TECHNIQUE)

It measures the height of a step from the substrate surface to the film surface step is formed by masking during deposition. Stylus scans length of several centimeters with a resolution of less than 0.2 microns and measures height of greater than 100Å. Sensitivity of the apparatus depends on surface roughness, flatness, and abruptness of the step.

WEIGHT GAIN METHOD

This method depends on the increase in weight of a film due to its mass increase. From the knowledge of its density and the deposited ares, film thickness (t) can be calculated from the relation

$$T = (w2-w1)/\rho A$$

Where,

W1 is the weight of the substrate before coating,

W2 is the weight of the substrate after coating,

ρ is the density of the film,

A is the deposited area of the film

Thickness is the most important film parameter, which controls the film properties. Hence, precise knowledge of the film thickness is necessary for the intensive study of the properties of thin films. Wide varieties of methods are available for measuring thin film thicknesses. Some of the thickness measurement methods available are Stylus profilometry, multiple beam interferometry, ellipsometry, spectrometry, x-ray microanalysis, microgravimetry and cross-sectional scanning electron microscopy (SEM). Complete information about merits and demerits of these methods, measuring range and accuracy can be found in any of the literature [60-62]. Piegari and Masetti [63] have made qualitative comparison of the available techniques [64-66]. The type of deposit, deposition technique and the nature of the substrate dictate the choice of the method.

The Mitutoya surf test SJ-301 is a stylus type surface roughness and thickness-measuring instrument. It can be used to measure the thickness of thin film coatings on any uniform surface. The stylus of the SJ-301 detector unit traces the minute irregularities of the vertical displacement of the fine needle, when the detector traversing over the film surface irregularities. For measuring film thickness, the stylus is placed over the uncoated surface and made to move towards the coating. Then it steps over the coating surface and moves over it. The vertical displacement gives the thickness of the coating. The thicknesses of the prepared thin film samples were found using this instrument. It is a non-destructive technique and the coatings may be used for further studies without any damage. The picture of the device along with the stylus is shown in Fig. 3.2 and their technical specifications are listed below:

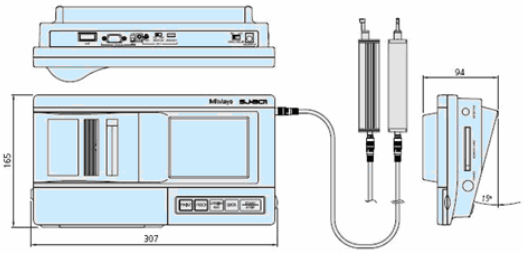

Fig 3.2 External view of the surface profiler SJ-301

Model number	: SJ-301 4 m N type
Measuring range x-axis	: 12.5 mm
z-axis	: 350 μm
Measuring speed	: 0.5 mm/s
Stylus tip radius	: 5 μm
Stylus tip material	: Diamond
Measuring force	: 4 mN
Detecting method	: Differential inductance
Recording magnification	: x10-1,00,000

TWO PROBE TECHNIQUE

In this technique, a constant current 'I' is passed through two aluminum strip contacts separated by a distance 'd' and the voltage 'V', between these strips is measured by using a high impedance voltmeter as shown in Fig. 3.3. For a thin film sample of thickness 't' and breadth 'b' placed between these two aluminum strips, the resistivity is derived from the following equations given by:

$$\text{Resistance} \quad R = \frac{V}{I} \qquad (3.1)$$

Resistivity ρ = R x (Cross sectional area/Length)

$$\rho = \frac{V}{I}\frac{t}{l}b \ \Omega\text{cm} \qquad (3.2)$$

In thin film technology, the ratio between the resistivity of the film material to the thickness of the thin film specimen 't' is termed as sheet resistance 'R_{sh}' and thus:

$$R_{sh} = \frac{V}{I}\frac{b}{l} \ \Omega/ \qquad (3.3)$$

Hence, for a square specimen *l* = b, the resistance of one square of a film is its sheet resistance R_{sh}, which is independent of the size of the square but depends only on resistivity and film thickness. In such case:

$$\rho = R_{sh}\, t \ \Omega\text{cm} \qquad (3.4)$$

Further, the activation energy can be calculated from the measured resistivity of the sample. Activation energy measures the thermal or other form of energy required to raise electrons from the donor levels 'E_d' to the conduction band or to accept electrons by the acceptor levels 'E_a' from the valence band respectively for n and p-type materials and this corresponds to the energy height difference (E_c-E_d) and (E_a-E_v) respectively. On measuring the variation of σ or ρ with temperature, the activation energy E_a can be determined from the slope of the straight line obtained by plotting $\ln(\rho)$ against $\frac{1}{T}$.

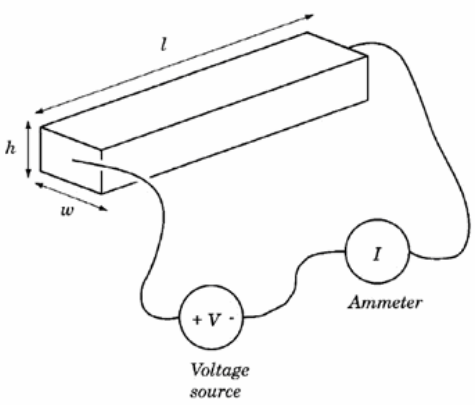

Fig 3.3 Two probe setup

For the present study, the four probe resistivity measurements were carried out on cobalt oxide films using an OSAW AC-DC Four point probe unit, in conjunction with a UNI-INSTA DC power supply. The voltage and current were measured using a HIL 2161 Digital multimeter and a Keithley 2000 multimeter respectively.

STRUCTURAL CHARACTERIZATION

When high-frequency electromagnetic waves are selected to have a wavelength in the order of interplanar spacing of crystals, they are diffracted according to Bragg's law [16]. The typical inter-atomic spacing in crystal is in the order of 2-10 Å. So, the wavelength of the radiation used for crystal diffraction should be in the same range. X-rays have wavelengths in this range and thus diffracted by crystals. Hence, an excellent experimental verification for the crystal structures can be availed by x-ray diffraction [17]. This method is an important technique for the characterization of thin films, since it gives a very broad range of information about the material such as crystal structure, composition and defects in the films.

In the present work, X-ray diffraction studies were carried out on cobalt oxide thin films deposited at different substrate temperatures. The technical details of the x-ray diffractometer used in the present study are:

Model	: X'pert PRO
X-ray source	: 1.8 KW ceramic copper tube
Operation potential	: 40 kV, 30 mA

Filter : Nickel
Radiation used : CuK_α - 1.54056 Å
Detector : Xe proportional counter

In this sophisticated diffractometer, diffracted beams are collected by the Xecelator detector, whose output is directly fed into a chart recorder. The beam of the x-ray source is automatically rotated with the help of a motor so that the x-ray beam incident angle can be precisely recorded. The detector, collecting the diffracted beam is mounted co-axially with source rotator and coupled to it in such a way that the source moves through an angle of 'θ', the detector moves through an angle of '2θ', so that it is in the right position to collect the diffracted x-rays from crystalline samples. The chart recorder plots the diffracted x-ray intensity as a function of '2θ'. The plot consists of a series of peaks of different intensities depending on the magnitude of the diffracted x-ray intensity in that direction.

From the XRD pattern one can determine the interplanar spacing (d), lattice parameters and hence the structure of the films. Usually, the diffraction peak positions are compared with the data from JCPDS cards. In the present case, the JCPDS standard data were compared with the obtained cobalt oxide data for fixing the structure of the prepared films.

In general, diffraction peak from a lattice plane is labeled as Miller indices (h k l) and these indices are related to inter-atomic spacing or 'd' spacing. For an orthogonal system (i.e., $\alpha = \beta = \gamma = 90^{o}$), the 'd' spacing for any set of planes is given by the formula:

$$\frac{1}{d_{hkl}^2} = \frac{h^2}{a^2} + \frac{k^2}{b^2} + \frac{l^2}{c^2} \qquad (3.19)$$

Where, 'a', 'b' and 'c' are the cell edges.
For hexagonal crystals,

$$\frac{1}{d_{hkl}^2} = \frac{4}{3}\left(\frac{h^2 + hk + k^2}{a^2}\right) + \frac{l^2}{c^2} \qquad (3.20)$$

For tetragonal crystals,

$$\frac{1}{d_{hkl}^2} = \left(\frac{h^2 + k^2}{a^2}\right) + \frac{l^2}{c^2} \qquad (3.21)$$

Using these relations, the Miller indices are assigned for each diffraction peak obtained in a diffractogram.

The width of the diffraction peak depends on the phase of the diffracted rays from each plane. If each plane in a crystal diffracts exactly one wavelength later than the preceding plane, all diffracted beams are in phase and constructive interference occurs, resulting zero peak width. If there is a phase lag of slightly greater than one wavelength $\lambda+\delta\lambda$, for rays diffracted from subsequent planes, a cumulative phase lag $\Sigma\delta\lambda = \lambda/2$ occurs at $(j+1)^{th}$ plane, ie: $j\delta\lambda = \lambda/2$. Then planes 1 and $(j+1)$ are exactly 'π' out of phase for radiations that is incident and diffracted at 'θ_1' and therefore cancel each other. The angular range between the Bragg peak 'θ' to 'θ_1' is the range over which the intensity of the diffracted beam falls from a maximum, at 'θ' to zero, at 'θ_1'. A similar lower limiting angle 'θ_2', occurs for which rays diffracted from adjacent planes have a phase difference of λ-$d\lambda$. The magnitude of the angular range 'θ_1' to 'θ_2' and hence the breadth of the diffraction peak, is governed by the number of planes 2j, and hence the crystal thickness. If the number of planes is very large, no significant broadening occurs, because '$\delta\lambda$' and therefore $(\theta_2-\theta_1)$ is negligibly small. The commonly accepted formula for particle size broadening is the Scherrer formula [18]:

$$D = \frac{0.94\,\lambda}{\beta\cos\theta} \qquad (3.22)$$

where, 'D' is the grain size, 'β' is the full width at half maximum (FWHM) of the respective peak, and 'θ' is the corresponding Bragg's angle.

Stress on the deposited film can also be measured from the x-ray diffraction peaks. Due to compressive stress, the whole x-ray diffraction pattern may be shifted to lower d-spacing such that a contraction of unit cell occurs. If the stress is non-uniform, different parts of the film may be deformed to different degrees and the diffracted lines become broadened. Commonly, both effects occur and lines may be both displaced and broadened. The

average internal stress developed in the film is determined by the relation [2]:

$$S = \frac{E}{2\delta}\left(\frac{a_o - a}{a_0}\right) \quad (3.23)$$

where, 'E' is the Young's modulus of the film, 'δ' is the Poisson's ratio of the film, 'a_o' is the bulk lattice constant, and 'a' is the lattice constant of the film. The origin of the strain is also related to the lattice mismatch and may be calculated from the slope of βcosθ vs. sinθ plot using the relation [19]:

$$\varepsilon = \frac{\lambda}{D\sin\theta} - \frac{\beta}{\tan\theta} \quad (3.24)$$

Where, 'D' is the grain size, 'β' is the full width at half maximum of the peak, and 'θ' is the corresponding Bragg's peak.

The dislocation density 'δ' ie, the dislocation lines per unit area of the crystal can also be evaluated from the grain size 'D' using the formula [20]:

$$\delta = \frac{1}{D^2}\text{ lines / m}^2 \quad (3.25)$$

Also using grain size 'D' and film thickness 't', number of crystallites 'N' has been estimated using the relation:

$$N = \frac{t}{D^3}\text{ / unit area} \quad (3.26)$$

OPTICAL CHARACTERIZATION

In early days, the study of the interactions of light with matter laid the foundations for quantum theory. Today, optical methods are among the most important tools for elucidating the electron structure of matter. Among the many available tools, spectrophotometer, photoluminescence spectrometer and Raman spectrometer are used to explain all the possible transitions such as band-to-band, exactions, between sub bands, between impurities and bands. In addition, the transitions by free carrier within a band and the resonances due to vibrational states of the lattice and of the impurities can be understood.

UV-Vis-NIR spectrophotometer

The measurement of transmission or reflection of a sample provides a satisfactory way to determine the form of the absorption edge. The absorption edge and energy band gap can be determined from the transmission measurement [21]. Hence, the optical transmittance properties of the films are analyzed with the Hitachi-3400 UV-Vis-NIR spectrophotometer. Technical specification of the instrument is listed below.

Model : Hitachi-3400 (double beam)
Wavelength range : 200 – 2500 cm^{-1}

When light radiation is incident on a thin film material with energy equal or greater than that of the band gap, absorption of photons can take place and electrons are raised in energy from the valance band to the conduction band, creating electron-hole pairs. The ability of a material to absorb photons of a given wavelength is measured quantitatively by the optical absorption co-efficient (□), measured in units of reciprocal distance [22].

$$\alpha(\lambda) = \frac{1}{t}\ln\left\{\frac{\left[1 - R(\lambda)\right]^2}{T(\lambda)}\right\} \quad (3.27)$$

where, 't' is the film thickness, 'R' and 'T' are the reflection and transmission co-efficient respectively.

There are two major types of intrinsic absorption processes involved in determining α, they are the direct and indirect absorption. As a general rule, the larger the band gap, the smaller is the value of 'α' for a given wavelength but absorption co-efficient also depends on the density of states in the conduction and valence bands. The optical absorption co-efficient is related to energy band gap and it is given by the following equation [23]:

$$\alpha h\nu = B\,(h\nu - E_g)^n \quad (3.28)$$

Where, 'B' is a constant and 'E_g' is the optical band gap. For crystalline materials, the exponent n is 1/2, 3/2, 2 and 3, when the transition is direct allowed, direct forbidden, indirect allowed and indirect forbidden respectively. Apparently, the plot of $(\alpha h\nu)^2$ or $(\alpha h\nu)^{1/2}$ against (hν) provides the nature and 'E_g' value of a particular film. The magnitude of 'n' can be estimated from the slope of the graph of log (α) vs. (hν) and hence can suggest the type of transition. The direct optical absorption is illustrated in Fig. 3.5.

Direct optical absorption is a first order process, involving only the absorbed photon and can be represented approximately as a vertical line on the energy versus wave vector (k) plot. The absorption transition conserves energy so that $\Delta E = h\nu$ and there is no change in 'k' between initial and final states except for the small momentum of the photon. An indirect optical transition is a second order process involving both the absorbed photon and a simultaneously absorbed or emitted phonon, which occurs when the minimum of the conduction band and the maximum of the valence band occur at different values of the wave vector 'k' as illustrated in Fig. 3.6.

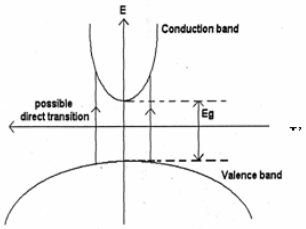

Fig 3.5 Direct transition from valence band to conduction band

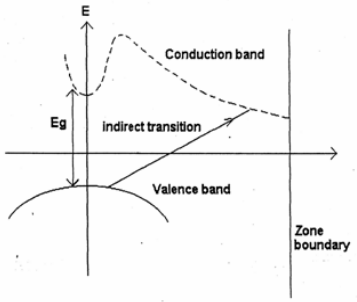

Fig 3.6 Indirect transition from valence band to conduction band

Here the absorption transition conserves energy by requiring $\Delta E = h\nu + E_p$ where, 'E_p' is the photon energy and the change in 'k' between the initial and final states 'Δk' is just equal to the value of 'k' of the phonon involved.

SURFACE MORPHOLOGICAL STUDIES

Scanning probe microscopes (SPM) are very different from optical microscopes in the sense that they operate with an extremely small probe tip, barely touching the surface, sensing different properties at close to atomic resolution in all three dimensions. Both the scanning electron microscopy as well as atomic force microscopy has been used in the present work for the surface morphological studies.

Scanning Electron Microscopy (SEM)

To study the surface morphology of thin film samples, the reflection mode of the optical microscope can be used. But this technique is limited in spatial resolution to a few tens of a millimeter. Very high resolution is required in electron beam technique. The most versatile among these is the scanning electron microscope. The main components of the instrument and the optical system are shown schematically in Fig. 3.7.

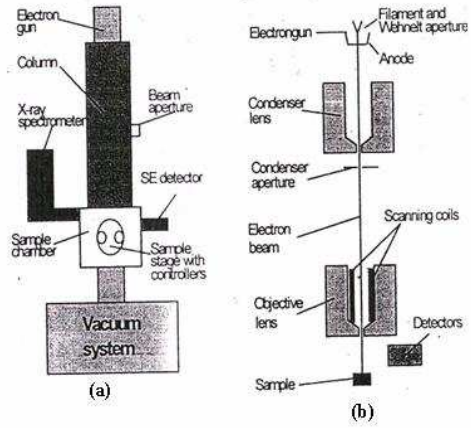

Fig 3.7 Main component of SEM together with optical system

An electron beam is generated by an electron gun at the top of the column. This beam is focused by two magnetic lenses inside the column and strike the sample in the sample chamber in a very small spot. When these electrons penetrate into the sample, some electrons are scattered back out of the sample and are collected by a suitable detector. These electrons are used to obtain information on the mean atomic number in the part of the sample from which they originated, relative to other part. Secondary electrons with very low energy also be released and are used to obtain information on the topography of the sample.

Usually, the electron beam is not left stationary on the sample, but scans across certain area in a raster pattern. The signal from one of the detector is selected and used to modulate the intensity on a viewing screen, which is scanned synchronously with the

primary beam in the column. Thereby an image is generated on the viewing screen with high brightness in areas with a strong signal from the detector, and darker areas where weak signals are detected. In this way, an enlarged image of the sample is obtained on the screen. To vary the magnification, the size of the scanned area of the sample is varied while the scanning width on the viewing screen is constant. The scanned image is particularly useful for examining the morphology of thin films of semiconductors, insulators and crystalline materials as well. Electrically insulating samples usually have to be given a conducting coating. In the present study, HITACHI Model S-3000H model is used, which is capable of taking magnified pictures of solid, dry, conducting and non-conducting specimen. Its technical specifications are listed below.

Model number : HITACHI Model S-3000H
Scanning probe diameter : 20 Å
Resolution : 60 Å at 30 kV
Magnification : 20 – 65,000
Voltage : 1 kV – 39 kV
Required specimen size : 5 x 5 mm^2 with 1 mm thickness

Using this instrument, SEM studies have been carried out to identify the morphology of the deposited oxide films. The SEM micrographs provide the nature of the surface (uniformity, smoothness and cracks) and the nature of the grains (Shape, particulate and grain size) [24].

RESULTS AND DISCUSSION

Cadmium oxide is an n-type wide band gap semiconductor, and it shows very high electrical conductivity even without doping due to the existence of shallow donors caused by intrinsic interstitial cadmium atoms and oxygen vacancies [1]. Cadmium hydroxide can be used as a precursor of CdO film. The ability to synthesize CdO nanocrystals with controlled shape, composition, and structure would enable a variety of size-dependent physical properties to be explored, including structural, electronic, and magnetic phase transitions as a function of size, composition, and shape. To improve chemical and physical properties of CdO thin films, researchers are trying to modify the synthesis procedure. Cadmium oxide received less attention because of their narrow band gap (direct band gap ~2.5ev, indirect band gap ~2.1ev) However, these films show higher mobility value (μ=130 cm^3/vs).which is necessary for high conductivity TCO materials, especially when low free carrier absorbance is desired.

1. R. Haul, D.Just, J. Appl. Phys. 33 (1962)487.

FILM FORMATION

The undoped and Zn doped Cadmium oxide thin films. were prepared by the cost effective spray technique using different precursor (cadmium acetate and zinc acetate) salts at 325°C substrate temperature .The micro structural, morphological, optical and electrical properties of the coated films have been investigated and the results are presented here.

THICKNESS MEASUREMENT BY WEIGHT GAIN METHOD

Thickness plays an important role in the film properties unlike bulk materials and almost all the properties of the films are thickness dependent are Reproducible properties are achieved one when the film thickness and the deposition parameters are kept constant. This method depends on the increase in weight of a film due to its mass increase. From the knowledge of its density and the deposited ares, film thickness (t) can be calculated from the relation

$$T = (w2-w1)/\rho A$$

W1 - Weight of the substrate before coating
W2 - Weight of the substrate after coating
ρ - Intensity of the film
A - Deposited area
T - Thickness of the film

The film thickness was found to equal to 0.34μm, 0.276μm, 0.484μm for undoped and zinc doped cadmium oxide thin films prepared using cadmium acetate and zinc acetate precursor.

XRD STUDIES

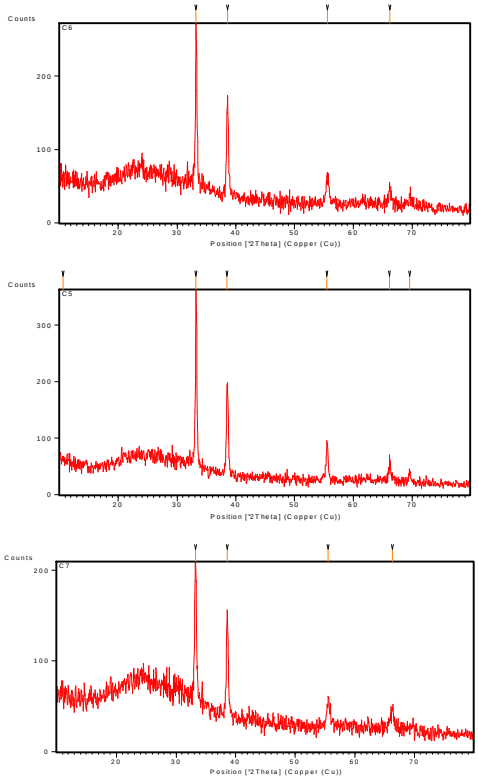

MORPHOLOGICAL STUDIES

AFM Analysis

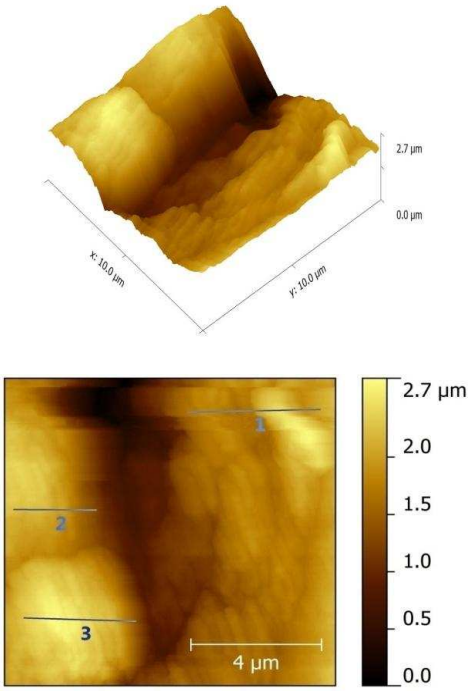

The two dimensional and three dimensional AFM images of 5wt% Zn doped CdO films.

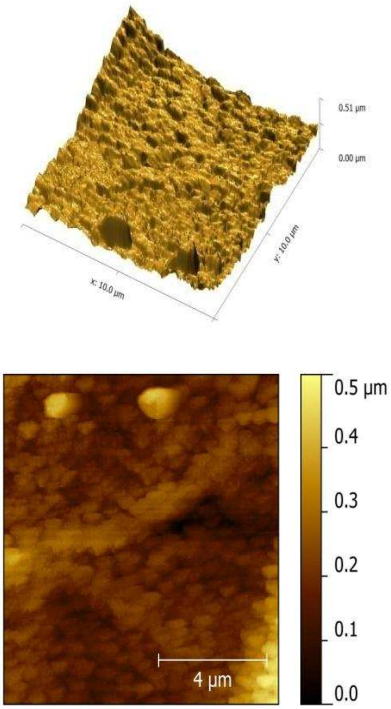

The two dimensional and three dimensional AFM images of 10wt% Zn doped CdO films, from this AFM image it was observed that the substrate fully covered with larger grain size without any cracks which shows the improved crystallinity of 5wt% Zn doped CdO thin films are evident from XRD analysis.

SEM analysis

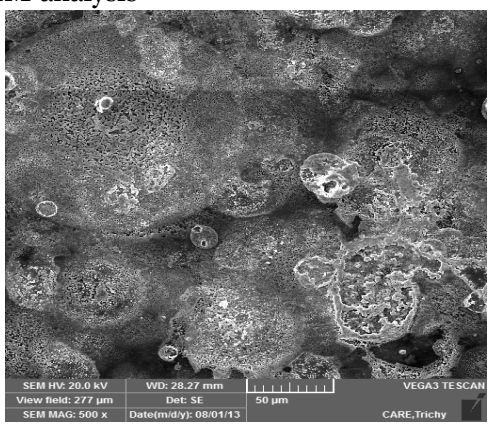

Mixture of small and larger products due to low Zn concentration.

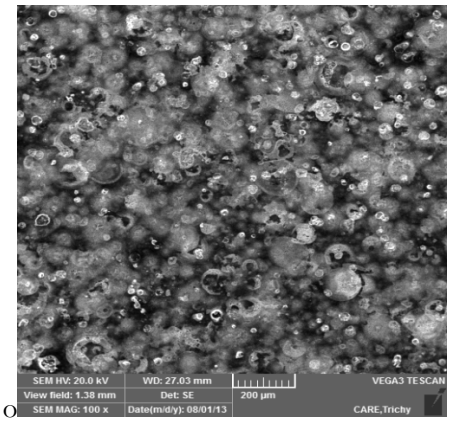

O

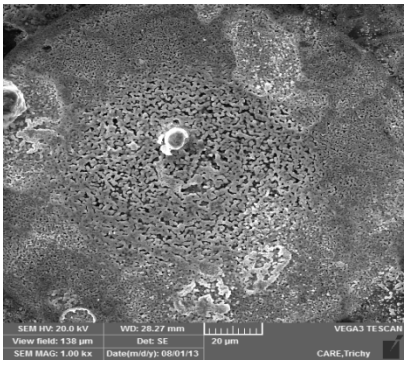

Cluster of grains were found throughout the surface with no cracks indicating better orientation of grains.

No grains were observed in the sample because more Zn concentration might have decreased the orientation of film growth.

OPTICAL STUDIES

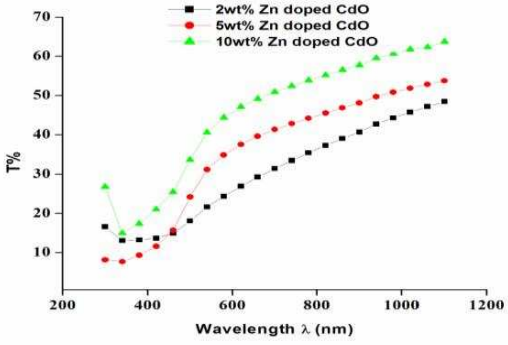

Transmittance spectra of Zn doped CdO thin films.

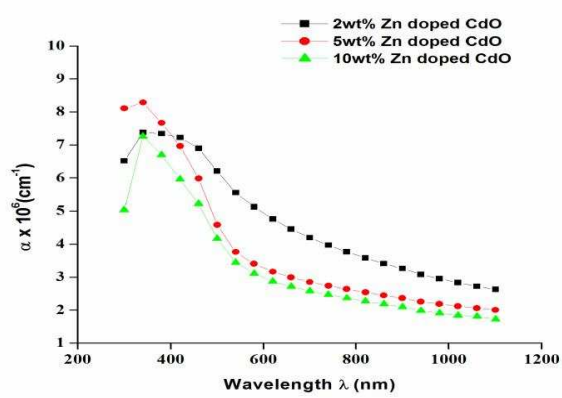

Absorption coefficient decreases with increase in Zn concentration.

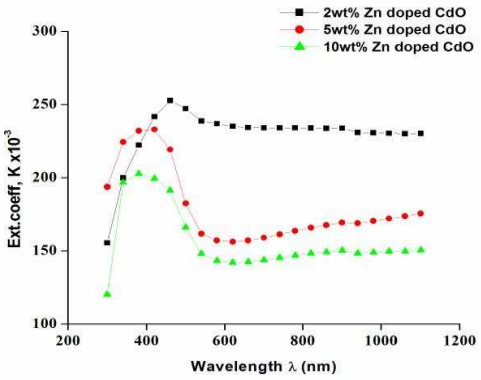

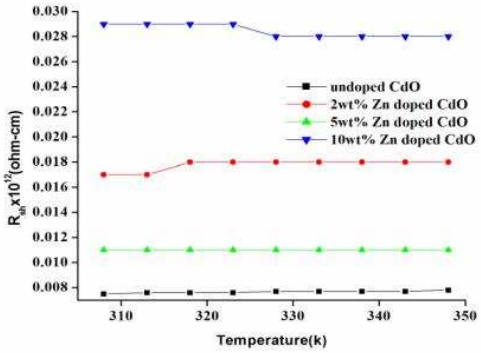

Variation of extinction coefficient with wavelength of Zn doped CdO thin films from the graph it is observed that the variation of k is similar to the absorption coefficient.

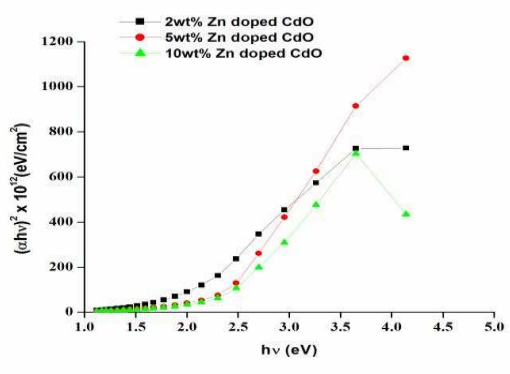

ELECRTICAL STUDIES

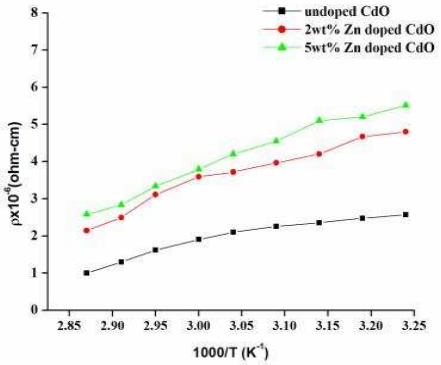

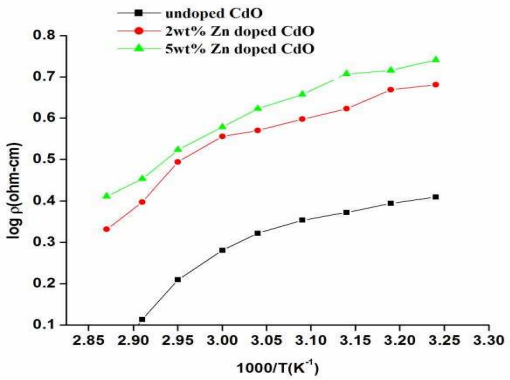

Conclusion

Zndoped CdO thin films were fabricated at 325°C by spray pyrolysis technique. The Zn concentration was varied as 2wt%, 5wt%, 10wt% of weight of the Cadmium acetate used to coat undoped CdO thin films. The films were characterized structurally, morphologically, electrically and optically, structural studies reveals that all the films are polycrystalline along (111) plane. Morphological studies shows that in AFM images the substrate fully covered with larger grain size without any cracks. In SEM image no grains were observed in the sample because more Zn concentration of film grow might have decreases the orientation of film growth. Optical studies show that transmittance decrease with decrease in Zn concentration absorption coefficient were absorbed to be equal ($10^{-6}cm^{-1}$) absorption coefficient decreases with increase in Zn concentration extinction coefficient bandgap was estimated 1.8eV, 2.0eV, 2.3eV for the films. Electrical studies shows that all films resistivity decreases with increase in substrate temperature indicating the semiconducting behaviour of CdO films.

Reference

[1] T. Suda N, Nasu K, Nasu K, Fujimori A, Siratori K(2000)Electronic Conduction In Oxides, Springer-Verla Berlin-Heidelberg-New Yrk.

[2] Chopra Cl, Das Sr 919830 thinfilm Solar Cells, Plenum Pree, New Yoek-London.

[3] Maissel Li. Glong R (1970) Handbook of Thin Films Technology, McGraw Hill, New York.

[4] M. Risti, S, Poporic and S. Music, Mater Lett 58, 2494 (2004).

[5] K. Gurumurugan. D. Mangaraj and Sa. K. Narayndass J. Cryst Growth 147, 355 (1995).

[6] B.Roy, Ii-Vi Compounds, Pergamon Press, Oxford 1969.

[7] R.Kondh, H.Dichimura, Y,Sakai, Jpn.J.Appl.Phy.10(1971)

[8] L.M. Su, N. Grote, F. Schmitt, Electron Let 20(1984)717.

[9] C.H. Champness, K. Ghoneim, J.K Chen, Can J Phys. 63 (1985) 767.

[10] F.A. Benko, F.P. Koffyberg, Solid State Commun. 57 (1986) 901.

[11] R.Ferro, et al., Phys. Stat. Sol. (A) 177(2000) 477

[12] K.L. Chopra, S.Major, D.K.Panday, Thin Solid Films 102 (1989) 1

[13] J. Muller, S. Weissenrider, J. Ana. Chem. USSR 349 (1994)380

[14] F.C.Lin Y.Shimizu, M.Egashira, J. Am. Ceram. Soc. 78 (1995) 2301
[15] J.F.Guillemoles, D.Lincot, P.Cowache, J.Vedel, Proceeding of the 10th EC Photovoltaic Solar Energy Conference, Lissabon, Portugal, 1991, p. 609.
[16] K. Sato, Takada, J.Appl.Phys. 53 (1982), p.609
[17] F.C.Lin, Y.Takao, Y.Shimizu, M.Egashira, Sens Actuators B 24-25 (1995) 843.
[18] J.Kessler, M.Ruckh, D. Hariskos, U.Rihle, R. Menner, H.W. Schock, Proceeding of the 23rd IEEE, Photovoltaic Specialists Conference, Louisville, KY, 10-14 May, 1993, IEEE Picataway, 447 pp.
[19] M.Krunks, E.Mellikov, Thin Solid Films 270 (1995) 33-36.
[20] S.Breheme, L.Elstner, F.Fenske, W.Henerion, V.Hoffmann, M.Poschenrieder, F.Schafer, B.Selle, I.Sieber, Mat. 1-4 (1995).
[21] M.Contreeas, B.Egaas, K.Ramanathan, J.Hiltner, F.Hasoon, R.Noufi, Prog. Photovoltaics 7 (1999) 311.
[22] R.Sheer, T.Walter, H.W.Schock. M.L.Fearheily, H.J.Lawrenz, Appl. Phys. Lett. 63 (1993) 3294.
[23] T.L.Chu, S.Chu Shirley, J.Electronic Matter. 19 (1990) 1002.
[24] R.Ferro, J.A. Rodriguez, Thin Films 347 (1999) 295.
[25] A.A.AI Quaraini, C.H.Champness, Proceedings of the 26th IEEE Photovoltaic Specialists conference, Anaheim, CA, 1997, p. 415
[26] C.H. Champness, C.h. Chan, Solar Energy Matter. Solar Cells 37 (1995) 75.
[27] I.M. Ocampo, Am.Ferandez,P/J Sabastion, Semicond. Sci. Technol
[28] Wells, A.F.(1984) Structural Inorganic Chemistry, Oxford: Clarendon Press. ISBN 0-19-855370-6.
[29] Lewis, Richard J.,Sr., Hawley's condensed chemical dictionary,13th ed., 1997, p.189
[30] T.L.Chu and Shirley S.Chu (1990). "Degenerate cadmium oxide films for electronic devices". Journal of Electronic Materials 19(9): 1003-1005.doi:10.1007/BF02652928.
[31] P.H Jefferson et al. (2008)."Bandgap and effective mass of epitaxial cadmium oxide". Applied Physics Letters 92 (2):022101
[32] K.L. Chopra, S. Ranjana Das. Thin Film Solar Cells, Plenum Press, New York, 1993.
[33] Y.S.Choi, C.G.Lee, S.M.Cho, Thin Solid Films 289 (1996) 153.
[34] C.T.Troy, Photonics Spectra 31 (1997) 34.
[35] Y.Sato, S.Sati, Thin Solid Films 281 (1996) 445.
[36] W.C. Shih, M.S. Wu, J. Crystal Growth 137 (1994) 319.
[37] M.Dinesau, P.Verardi, Appl. Surf. Sci. 106 (1996) 149.
[38] C.Messaoudi, D.Sayah, Abd-Lefdil, Phys. Stat. Sol.A.151 (1995) 93.
[39] Pushparajar, A.K. Arof, S. Radhakrishna, J.Phys. D27 (1994) 1518.
[40] S.Major. A.Benerjee, K.L. Chopra, Thin Solid Films 108 (1983) 333.
[41] D.J. Goyal, C.Agashe , M.G. Takwale, B.R.Marathe, V.G.Bhide, J.Matter.Sci, 27 (1992) 4705.
[42] A.J.C. Fiddes, K. Durose, A.W. Brinkman, J. Woods, P.D. Coats, A.J. Banister, J. Crystal Growth 159 (1996) 1996.
[43] P.S. Nayar, A.Catalano, Appl. Phys. Lett. 39 (1981)105.
[44] H.Nanto, T.Minami, S.Schooji, S.Takato, J.Appl. Phys. 55 (1984) 1029.
[45] T.Minami, H.Nanto, S.Takata, Thin Solid Films 124 (1985) 43.
[46] P.Petron, R.Singh, D.E. Brodie, Appl. Phys. Lett. 35 (1979) 390.
[47] C.Sravani, K.T.R. Reddy, P.J.Reddy, P.J. Reddy Semicond. Sci. Technol. 6. (1991) 1036.
[48] J.Hu, R.G.Gordon, J. Appl. Phys. 71 (1992) 880.
[49] H.Sato. T. Minami, T.Miyata, S. Takata, Ishii, Thin Solid Films 246 (1994) 65.
[50] S.N. Qiu, C.x. Qiu, I.Shis, Solar Energy Mater. 16 (1987) 471-475.
[51] G.Santana, A.Morales-Acevedo, O.Cruz, G. Contreras-Puente, L. Vaillant, Superficies Vacio 9 (1999) 300-302.
[52] J.Aranovich, A.Ortiz, R.H. Bude, J. Vac.Sci Technol. 16.(1979) 994.

[53] H.Tabet-Derraz*, N.Benramdane, D.Nacer, A.Bouzidi, M.Medles
[54] Jinho Chang, Rajaram S.Mane, Dukho Ham,Wonjoo Lee,Byng Won Cho,Joong Ki Lee , Sung-Hwan Han*
[55] C.Dantus*, R.S.Rusu, G.I.Rusu

STRUCTURAL AND PHOTOLUMINESCENCE CHARACTERISATION OF ISILAR DEPOSITED UNDOPED AND IN DOPED CdS THIN FILMS

K. Kalpana

Asst. Professor of Physics, Bon Secours College for Women, Thanjavur.

Abstract

In this Present work CdS thinfilms have been prepared by ISILAR technique. Structural and Photoluminescence properties were studied under different doping level of In. The physical properties of the films were analyzed to understand the influence of In doping level on these properties. The calculated crystallite size of CdS films found to decrease with the increase in In doping level from 54.80 nm to 23.65 nm.PL spectra Confirm good crystalline nature of CdS: thin films with lesser defect density. Hence CdS : In thin films which lead to prospective application in Photovboltaic application.

Key words: *CdS thinfilms, ISILAR technique, Structural and Photoluminescence*

1. INTRODUCTION TO CDS THIN FILMS AND DEPOSITION TECHNIQUES

1.1. INTRODUCTION

CdS is a semiconductor material due to its very important role on the photovoltaic technique and optoelectronic devices. It has been used as a partner of several types of thin film solar cells such as CdTe,Cu_2 S CuInSe for the fabrication. Cds has suitable band gap, high absorbtion Coefficient and considerable energy conversion efficiency for solar cells.

The highest efficiency for this type of solar cell is about 16.5%. As several authors have pointed out, the good performance of solar cells depends on several aspects such as growth technique, grain size, optical range of absorption, quality of the interface, crystalline structure, among others. It is not an easy task to control and maintain these properties as constant when the photovoltaic devices are industrially produced. These aspects need to be considered to improve efficiency of the solar cells and on the final cost of the devices. Different growth techniques have been implemented to prepare each one of the materials in order to obtain better performance both in cost as in preparation facilities.

Chemical bath deposition (CBD), has demonstrated to be a simple and low cost technique to prepare CdS films as optical windows for solar cells, with 2.42 eV as band gap energy, which is considered as the ideal partner of the CdTe for solar cells. As a wide band-gap semiconductor, cadmium sulphide has been widely used in the fields of solar cells for photoelectric conversion, light-emitting diodes for flat-panel displays, sensors, and photo catalysis. In this present work cadmium sulphide have been prepared by ISILAR method.

1.2. BASIC MECHANISM OF SILAR METHOD

In SILAR method, to prepare thin films substrates are immersed into separately placed cationic and anionic precursors and precipitate formation in the solution, i.e. The wastage of the material was thus avoided. Also SILAR can be used to deposit compound material on a variety of substrate such as insulator, semiconductor and metal.

One SILAR cycle contained four steps

The substrate was immersed into first reaction containing the aqueous cation precursors.

- Rinsed with water.
- Immersed into the anion solution.
- Rinsed with water.

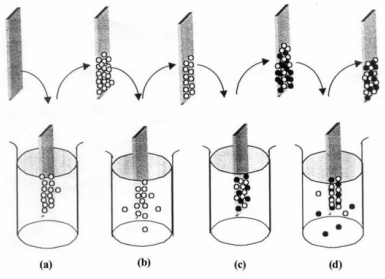

The deposition parameters employed for the preparation of In doped CdS thin films are presented as follows.

Source for Cadmium	Cadmium Chloride (0.1M)
Source For sulphur	Thiourea (0.1M)
Source For Indium	Indium Chloride (2,4,6,8 at. %)
S/Cd ratio	1:1
pH value	11
Dipping Time(sec)	(anionic and cationic solutions 10 s^+ Water 15 s)
Dipping Cycles	100

2. CHARACTERIZATION TECHNIQUES: STRUCTURAL AND PHOTOLUMINESCENCE STUDIES

2.1. INTRODUCTION

In the past years the advancement in science has taken place mainly with the discovery of new materials. Characterization is an important step in the development of exotic materials. The complete characterization of any material consists of phase analysis, compositional characterization, structural and surface characterization, which have strong bearing on the properties of materials. In this section different analytical technique used to characterize our thin films are described with relevant principles of their operation and working.

2.2. X-RAY DIFFRACTION (XRD) TECHNIQUE

X-ray Diffraction is a non-destructive analytical technique which provides detailed information about the internal lattice of crystalline substances, including unit cell dimensions, bond-lengths, bond-angles, and details of site-ordering. The data generated from the X-ray analysis is interpreted and refined to obtain the crystal structure.

X-ray diffraction (XRD) is a powerful technique for determination of crystal structure and lattice parameters. The basic principles of X-ray diffraction are found in textbooks e.g by Buerger, Klug and Alexander, Cullity Tayler, Guinier, Barrett and Massalski. Much of our knowledge about crystal structure and the structure of molecules as complex as DNA in crystalline form comes from the use of x-rays in x-ray diffraction studies. A basic instrument for such study is the Bragg spectrometer.

2.3. BRAGG'S LAW AND SCHERR'S FORMULA

Diffraction in general occurs only when the wavelength of the wave motion is of the same order of magnitude as the repeat distance between scattering centers. This condition of diffraction is nothing but Bragg's law and is given as,

$$2d\sin\theta = n\lambda$$

Where,

d= interplaner spacing
θ= diffraction angle
λ= wavelength of x-ray
n= order of diffraction

For thin films, the powder technique in conjunction with diffractometer is most commonly used. In this technique the diffracted radiation is detected by the counter tube, which moves along the angular range of reflections. The intensities are recorded on a computer system. The X-ray diffraction data thus obtained is printed in tabular form on paper and is compared with Joint Committee Power Diffraction Standards (JCPDS) data to identify the unknown material. The sample used may be powder, single crystal or thin film.

The crystallite size of the deposits is estimated from the full width at half maximum (FWHM) of the most intense diffraction line by Scherrer's formula as follows,

$$D = 0.9\,\lambda/\beta\cos\theta$$

Where,

D is the crystallite size, λ is wavelength of X-ray used, β is full width at half maximum (FWHM) in radians, θ is Bragg's angle. The X-ray diffraction data can also be used to determine the dimension of the unit cell. This technique is not useful for identification of individuals of multilayer or percentage of doping material.

2.4. PHOTOLUMINESCENCE SPECTROSCOPY

2.4.1. INTRODUCTION

Photoluminescence (PL) is a non-destructive optical technique used for the characterization, investigation, and detection of point defects or for measuring the band-gaps of materials. Photoluminescence involves the irradiation of the crystal to be characterized with photons of energy greater than the band-gap energy of that material. It is contactless technique of probing the electronic structure of Material. Light is directed onto a sample, where it is absorbed and impact excess energy into the material in a process called photo-excitation. One way this excess energy can be dissipated by the sample is through the emission of light, or luminescence. In the case of photo-excitations this luminescence is called photoluminescence.

2.4.2. PRINCIPLE OF PHOTOLUMINESCENCE

The general concept of PL measurement is easy to grasp as outlined by the figure. Light of energy in excess of the fundamental band gap (here blue) is directed on a semiconductor sample where it gets absorbed, thereby generating photoelectrons and holes. These carrier release part of their energy by nonradiative processes until they reach a local ground state, from they may radiatively recombine upon emission of a new photon. The energy of the emitted light, which is called luminescence, relates to the energy difference of the electronic states involved in the transition. PL provides a wealth of information on semiconductor properties such as the fundamental band gap, impurity levels and defect states, electronic complexes and the relaxation mechanism of carriers in the materials.

3. RESULTS AND DISCUSSION

3.1. STRUCTURAL STUDIES

The X-ray diffraction patterns of the undoped and In doped ISILAR deposited CdS films are shown in Fig 3.1 (a-e). For all the films, a single diffraction peak approximately at 2θ = 26.7° is observed which may be associated with the (111) plane of the cubic Phase or the (002) plane of hexagonal phase. As the diffraction peaks corresponding to H(002) and C(111) are very close to each other, it is difficult to distinguish them. moreover, Since no other peaks related to both the phase are obtained in the present study, it is not easy to arrive at a decision on the phase of the deposited film. But, it is believed that the actual phase for CdS films, in the present study, should be only cubic, because the transformation of phase from cubic to hexagonal can take place only when the process temperature is above 623K. It is noteworthy to mention here that the absence of any other peak in the XRD patterns indicates the good crystalline quality of the films. From the XRD Pattern the crystallite size and other structural parameters are evaluated.

Particle Size Determination

$$\text{Grain Size } D = \frac{0.94\,\lambda}{\beta \cos\theta}\ \text{nm}$$

Dislocation Density

$$\delta = 1/D^2$$

Lattice Parameters a(=b=c) for the cubic structure of CdS is calculated using the formula

$$\frac{1}{d^2} = \frac{h^2 + K^2 + l^2}{a^2}$$

The calculated cryatallite size, dislocation density and lattice parameter values are given in Table 3.1.

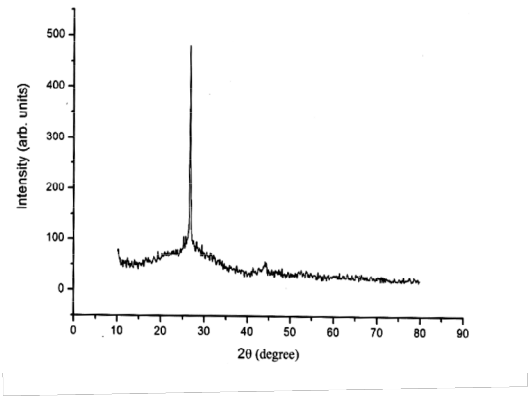

Fig.3.1 (a) XRD pattern of undoped CdS film

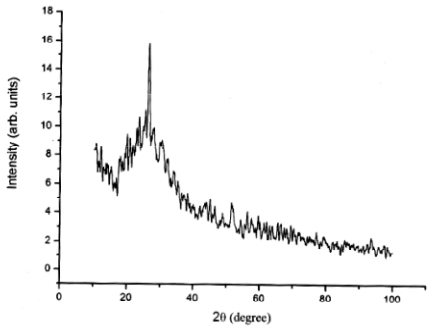

Fig.3.1 (b) XRD pattern of In doped CdS film (In doping level: 2 at. %)

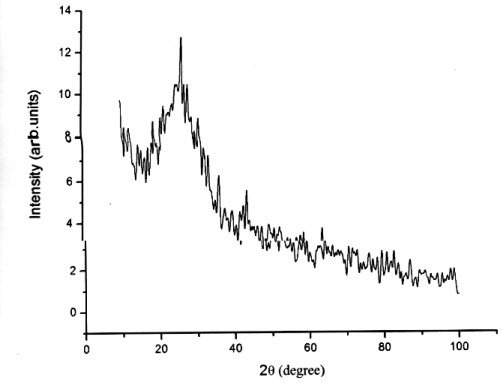

Fig.3.1 (c) XRD pattern of In doped CdS film (In doping level: 4 at. %)

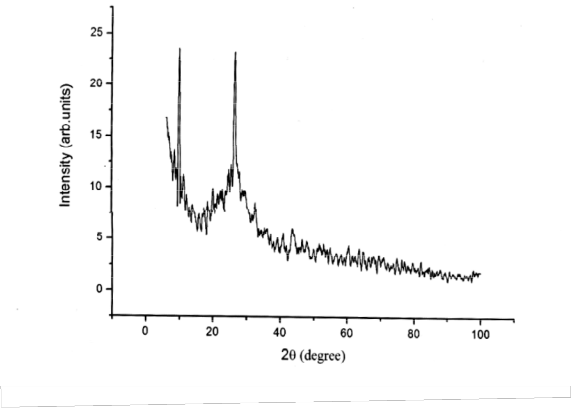

Fig.3.1 (d) XRD pattern of In doped CdS film (In doping level: 6 at. %)

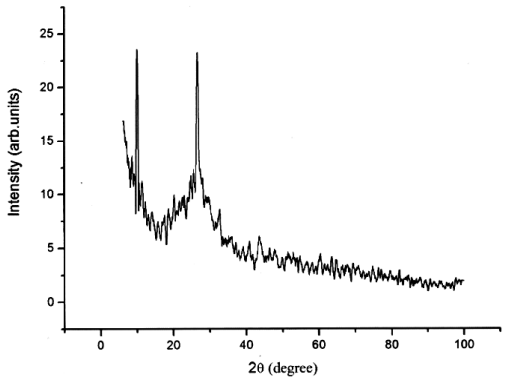

Fig.3.1 (e) XRD pattern of In doped CdS film(In doping level: 8 at. %)

Table 3.1 Structural parametyers of CdS : In thin nfilms

In doping level (at.%)	Crystallite size D (nm)	Lattice parameter (a) A	Dislocation density (δ) *10^{14} lines/m^2
0	54.80	5.814	3.329
2	48.51	5.809	4.249
4	34.07	5.813	8.615
6	33.31	5.816	9.013
8	23.65	5.816	17.879

3.2. Photoluminescence (PL) Studies

The Pl Spectra recorded for CdS:In thin films in the present study extend from 450nm to 750nm (Fig 3.2). The consist of a sharp and strong intrinsic band at approximately equal to 525nm (Near Band Edge Emission-NBE) and two very lwo intense peaks at 580nm and 710 nm. The very broad band around 525nm is related to radiative transitions. Hence, increase in the NBE intensity with In doping level, indicates the enhancement in radiative recombination involving impurity or defect levels. The peak at 580nm is associated with Cd^{2+} interstitials and the increase the intensity of the peak at 580nm with In doping level explores the incorporation of In^{3+} into the Cd^{2+} sites od CdS lattice, which in turn cause an increase in the number of interstitial Cd^{2+} ions. The band at approximately equal to 710nm is attributed to the complex defects

including the cadmium vacancies. In the present study, the very feeble defect related bands observed at and above 580nm are the clear identification of the good quality of the CdS films and/ or the presence of lesser number of defects in the crystal lattice.

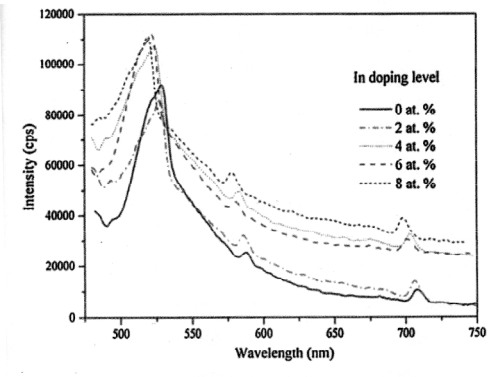

Fig.3.2. Room temperature photoluminescence spectra of CdS: In thin films

4. CONCLUSION

Good crystalline quality CdS: In thin films were deposited by an improved SILAR technique with different doping levels (0, 2, . . . , 8 at. %) of In. The physical properties of the films were analyzed to understand the influence of In doping level on these properties. From the XRD studies, it is confirmed that the obtained CdS: In films have cubic phase with (1 1 1) as preferential orientation. The calculated crystallite size of CdS films is found to decrease with the increase in In doping level from 54.80nm to 23.65nm. The observed weak band at and above 580nm in the PL spectra confirms good crystalline nature of CdS: In thin films with lesser defect density. Hence, the above discussed results of CdS:In thin films, induced us to conclude that, the deposition conditions employed in the present study are suitable to achieve defect free and good stoichiometric CdS: In thin films which lead to prospective applications in photovoltaic's. Furthermore, the SILAR technique employed in the present study can be recognized as one of the simplest inexpensive potential depositrion techniques to achieve good stoichiometric thin films.

REFERENCES

[1] J. Montero, G. Guillean and J. Herrero, Thin Solid Films, xxxx (2011) xxx-xxx. Doi: 10.1016/j. Tsf.2010.12.103.

[2] T. Fukano and T. Motohiro: Sol. Energy. Matter. Sol. Cells, 82 (2004) 567-575.

[3] K. Ravichandran and P. Philominathan. Appl. Surf. Sci. 255 (2009) 5736.

[4] Muto. P and Furunchi.S and Chou N.J, Electrochem. J Soc., 120, 701 (1973).

[5] P.K. Vidhya lai, K.P. Vijayakumar J. Mater. Sci. Lett. 13(1994) 1725.

[6] Element of X-Ray diffraction on 2nd Edition Cullity. B.D.

[7] Goswami, "Thin film fundamental", New Age International (p) Ltd., New Delhi (1996).

[8] K.L. Chopra, S. Major and D.K. Pandya, Thin Solid Films, 102 (1983) 1-46.

[9] M.R. Vaezi, Mater. Chem. Phys, 110 (2008) 89-94.

NANOSTRUCTURED NICKEL OXIDE THIN FILMS BY SPRAY PYROLYSIS AND ETHANOL SENSING RESPONSE

[1]Charles J* & [2]Lawrence N

[1]*Asst Professor of Physics, St. Joseph's College, Trichy*

[2]*Associate Professor of Physics, St. Joseph's College, Trichy*

Abstract

The Nickel Oxide thin films were deposited on a glass substrate by spray pyrolysis technique using 0.05M concentrated precursor solution of nickel chloride and air as a carrier gas at 250 ℃ substrate temperatures then the films are annealed at 350 ℃ for three hours. The prepared and annealed zinc oxide thin films are characterized by x-ray diffraction, scanning electron microscopy and ultra violet-visible spectrum. The x-ray diffraction pattern indicates that the zinc oxide thin films are polycrystalline nature with preferred orientation along c-axis with cubic structure and grain size is about 44.5nm. From x-ray diffraction pattern, the inter-planner spacing, strain, dislocation density and texture coefficients were estimated. Scanning electron microscope image showed that the nickel oxide thin films are smooth in morphology, spherical in shape and grain size is about 25-50nm. The optical studies showed the nickel oxide thin films are having partial transmittance (~45%) and low absorption. The ultra violet-visible spectra shows that the thin films having band gap in the range 3.5-3.6eV and it confirms nickel oxide thin films is a semiconductor with wide band gap material. The application of nickel oxide thin films are Ethanol sensing carried out at 373K were found that the resistance with various concentration of Ethanol.

Key words: *NiO, Spray pyrolysis, Nanostructure, Optical properties, Ethanol sensing.*

1. Introduction

The gas sensing mechanisms normally accepted for semiconductor sensors assume that the oxygen adsorbed on the surface of the oxide removes some of the electronic density and thus decreases the material's conductivity. When reduction gas molecules come into contact with this surface, they may interact with this oxygen, leading to inverse charge transference. Upon the gone out of the electrons to the conduction band, resistivity increases. This utilizes the gas-induced resistance variations in potential barrier height at grain boundaries (i.e. changes in thickness of the space charge layer) to detect ethanol vapors in air. For polycrystalline substances, grain boundaries contribute most of the resistance.

2. Experimental Details

The Nickel Chloride precursor solution was taking to deposit the NiO thin film by Spray Pyrolysis deposition method. The Air is the carrier gas is filled in the cylinder and the air flow was controlled by the Pressure Gauge. The glass substrates are put on the furnace then the furnace heated by the filament and it controlled by a temperature controller. The temperature was measured by the thermocouple sensor. After reaching the substrate temperature 250°C, Air was opened in the flow of 1.0 kg/cm^2. The solution was sprayed on the substrate for few seconds and it get few seconds to decomposition takes place then again spray for few seconds. This process will continuous until spraying the complete solution. After the deposition the substrate temperature decreases slowly to the room temperature. Now we obtain the good Nickel Oxide thin film.

The Nickel Oxide thin film deposited onto glass substrate is treated at 350°C constant temperatures in Air atmosphere for 3 hours. After this the substrate temperature was decreased slowly to room temperature.

During spray pyrolysis process, when droplets arrive close to the preheated substrates, the droplets undergo thermal decomposition, which results into the highly adherent Nickel oxide film formation. During the pyrolytic process, possible reaction mechanisms are as follows,

$$NiCl_2.6H_2O + H_2O \rightarrow 2HCl + NiO + 6H_2O$$

As-deposited NiO films were found to be well adherent on the glass substrate.

3. Structural Characterization

The crystalline nature and structural properties of nickel oxide films were analyzed using powder X-Ray Diffraction pattern (XRD) [Panalytical Xpert pro, with Cuk_{α} radiation (λ = 154059Å). This XRD pattern shows the formation of crystalline structure of NiO films. The observations were discussed below, as the films were by keeping the deposition temperature 250°C and distance between the nozzle of the gun and the substrate as ~48 cm throughout the deposition process.

3.1. XRD pattern for Un-annealed NiO Thin Film

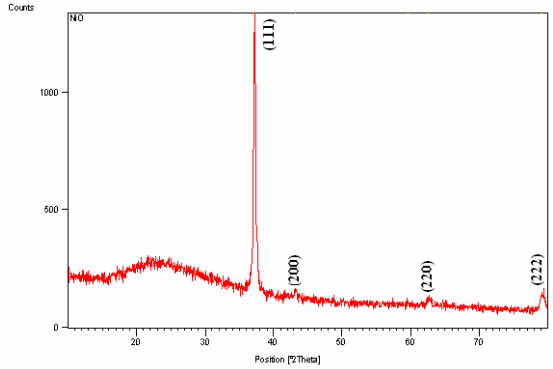

Fig.1. X-Ray diffraction pattern of Un-annealed NiO film

Table 1: X-Ray Diffraction of Un-annealed NiO film

Position [°2Th.]	FWHM [°2Th.]	d-spacing [Å]	Grain Size D(nm)	strain (ε) $lines^{-2}/m^{-4}$	Texture Coeff	Dislocation Density $(lines/m^2)$	Rel. Int. $[I/I_0]$ [%]
37.1766	0.3526	2.41651	43.31	0.067	4.34555	5.33E+14	100.00
43.1942	0.7112	2.09276	21.89	0.114	0.20641	2.09E+15	4.75
59.5957	0.3247	1.55136	51.37	0.036	0.08343	3.79E+14	1.92
62.5984	0.6494	1.48398	26.08	0.068	0.14427	1.47E+15	3.32
79.1461	0.5308	1.20914	35.38	0.041	0.22032	7.99E+14	5.07

The X-Ray diffraction pattern of a NiO film deposited at 250°C temperatures is shown in figure.1. According to JCPDS standard data, NiO having the Cubic crystalline structure and the theoretical pattern for NiO values for lattice constant (a=b=c=0.417Å) also is depicted in this figure. It is evident from the figure that NiO thin film molecules are in cubic structure during pyrolysis. The main peak (111) in diffracted angle 2θ=37.1766 and the miller indices (hkl) are (200), (220) and (222) peaks were also observed at 2θ=43.1942, 62.5984, and 79.1461. Full width half maximum intensity of about 0.3526 rad and it's having 100% of relative intensity. The inter-planar spacing between the lattices was 2.4165Å and Grain Size of the particle estimated using the Scherrer's formula and it is found to be 43.31nm. The strain, dislocation density and texture coefficient of the material is 0.067 $lines^{-2}/m^{-4}$, 5.33 $X10^{14}$ $lines/m^2$ and 4.3455 respectively.

3.2. XRD pattern for annealed NiO Thin Film

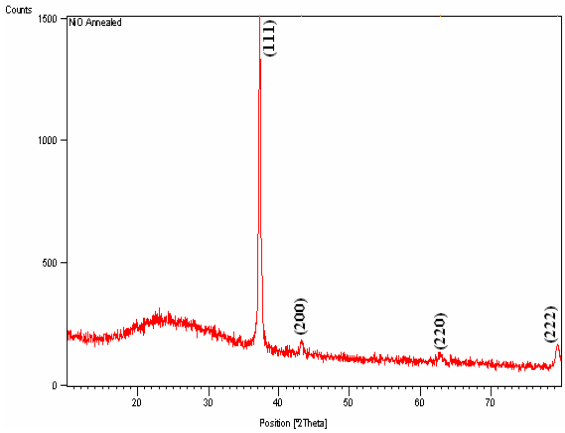

Fig.2 X-Ray diffraction pattern of Annealed NiO film

Table 2: X-Ray Diffraction of annealed NiO film

Position [°2Th.]	FWHM [°2Th.]	d-spacing [Å]	Grain Size D(nm)	strain (ε) lines^{-2}/m^{-4}	Texture Coeff	Dislocation Density (lines/m^2)	Rel. Int. [I/I$_0$] [%]
37.2266	0.3435	2.41337	44.50	0.064	3.5226	50.49E+14	100.00
43.2458	0.6987	2.09038	22.30	0.111	0.1426	2.01E+15	4.05
62.8290	0.6494	1.47909	26.13	0.0673	0.1187	1.46E+15	3.37
79.3606	0.3586	1.20641	52.40	0.0280	0.2159	3.64E+14	6.13

The X-Ray diffraction pattern of a NiO thin film deposited at 250°C temperatures and it was annealed in the air atmosphere at 350°C for 3 hours as shown in the figure.2. According to JCPDS standard data NiO having the Cubic crystalline structure and its lattice constant (a=b=c=0.417Å) also is depicted in this figure. It is evident from the figure that NiO thin films are in Cubic structure during pyrolysis. The main peak (111) in diffracted angle 2θ=37.2266 and the miller indices (hkl) are (200) then (220) and (222) peaks were also observed at 2θ=43.2458, 62.829, and 79.3606. Full width half maximum intensity is about 0.3435 rad and it is having 100% of relative intensity. The inter-planar spacing between the lattices is 2.4133Å and the Grain Size of the particle is estimated using the Scherrer's formula and the value is 44.50nm. The strain, dislocation density and texture coefficient of the material is 0.064 lines^{-2}/m^{-4}, 50.49X10^{14} lines/m^2 and 3.5226 respectively.

3.3. Morphological Studies

The surface morphology of the samples has been studied by using a Field Emission Scanning Electron Microscope (JEOL JSM – 6330F) [FE-SEM] at SASTRA University, Thanjavur.

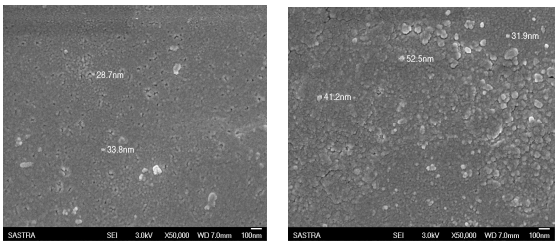

(a) **(b)**

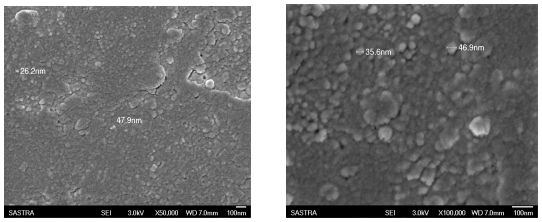

(c) **(d)**

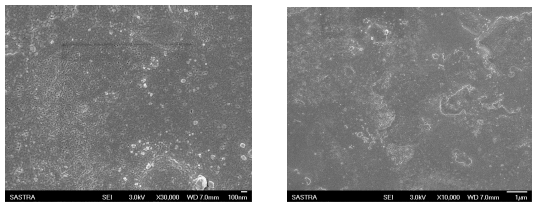

(e) **(f)**

Fig. 3 FE-SEM images for Un-annealed NiO films at a) 50,000 b) 50,000 c) 50,000 d) 1,00,000 e) 30,000 f) 10,000 magnifications respectively

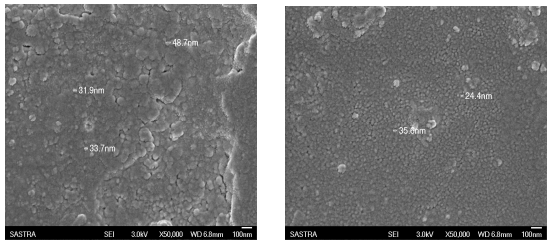

(a) **(b)**

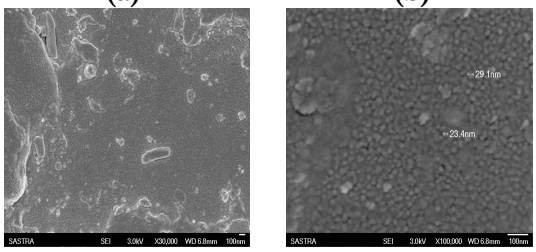

(c) **(d)**

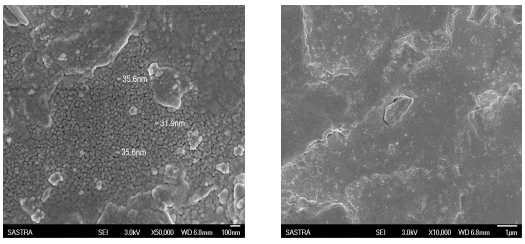

(e) **(f)**

Fig.4 FE-SEM images for Annealed NiO films at a) 50,000 b) 50,000 c) 50,000 d) 1,00,000 e) 30,000 f) 10,000 magnifications respectively

The SEM Images for the Un-annealed NiO thin films are shown in Figure 3 and annealed NiO thin film is shown in the figure 14. It is seen that the deposits are flat and smooth in morphology. The surface morphology of a NiO and annealed NiO thin film particles are in spherical shape. It's having good uniformity in lattice arrangement and the grain size of the particles is about 25-50nm range.

3.4. Optical Studies

The Optical Transmittance measurements of un-annealed and annealed ZnO thin films are studied using LAMBDA 35 ultra-violet/visible Spectrophotometer at St. Joseph's College, Trichy. The transmittances measurement is taken in the wavelengths range from 300nm to 1100nm are shown in the figure 5 & 6 respectively.

3.5. Transmission Spectra for NiO thin films

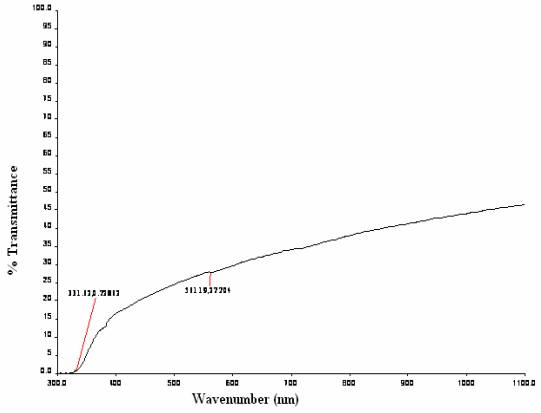

Fig.5 UV-VIS Transmission curve of Un-annealed NiO thin film

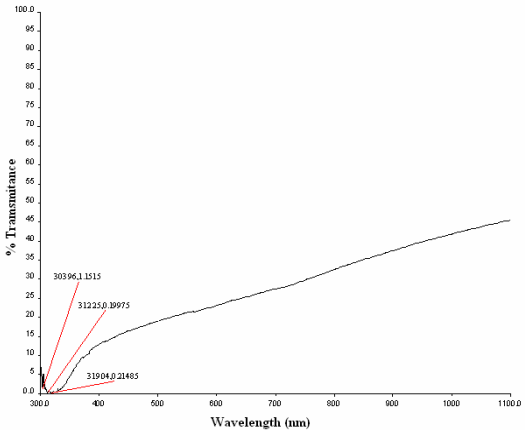

Fig 6. UV-VIS Transmission curve of Annealed NiO thin film

The Optical Transmittance spectrums of NiO and NiO annealed at 350°C are the two thin films in the wavelengths range from 300nm to 1100nm are shown in the figure. The films are having transparent in the visible range of the electromagnetic spectrum with an average transmittance values up to 45%. The annealed NiO thin films are having more transmittance compare to un-annealed thin films, because of annealing process are giving enough energy to lattice and eliminate water, solvent and moistures in the films.

3.6. Absorption Spectra for NiO thin films

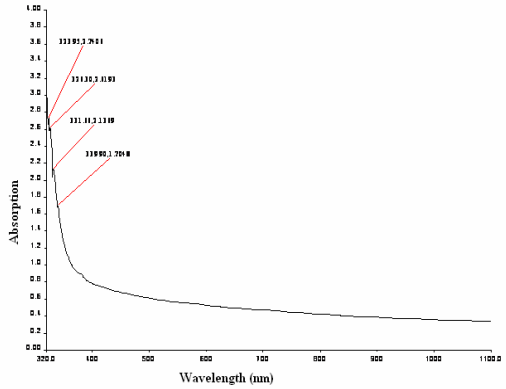

Fig.7 UV-VIS Absorption curve of Un-annealed NiO thin film

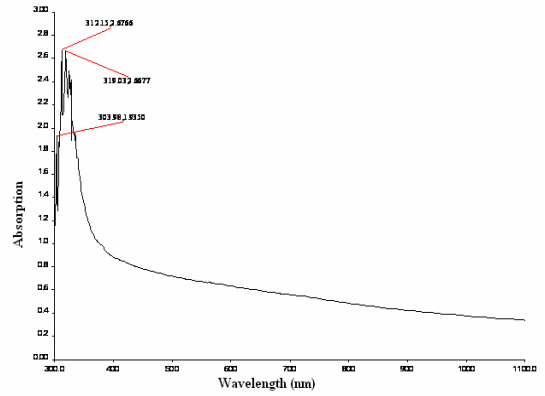

Fig.8 UV-VIS Absorption curve of Annealed NiO thin film

The Absorption spectrum of the un-annealed NiO and annealed NiO thin films are the two thin films in the wavelengths range from 300nm to 1100nm are shown in the figure. The spectra reveal that the films having low absorbance in the visible/near infrared region while absorbance is high in the ultraviolet region.

3.7. Determination of Band Gap Energy

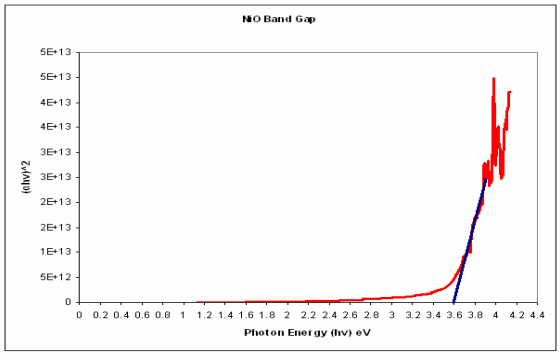

Fig.9. The Band Gap energy of un-annealed NiO thin film

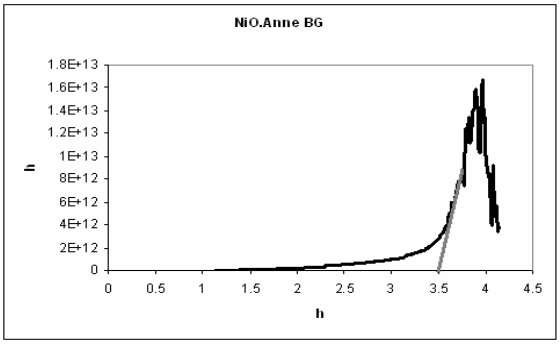

Fig.10. The Band Gap energy of Annealed NiO thin film

The band gap value of NiO thin film is 3.6eV and the band gap value of annealed NiO thin film is 3.5eV. The annealed ZnO thin film is having constant absorption in the ultraviolet region while the un-annealed film shows exponential decreased in absorption. It is known fact that decreasing optical absorption can be attributed to the improvement in crystallinity for variations in stoichiomatry.

3.8. Impedance Measurement Analysis

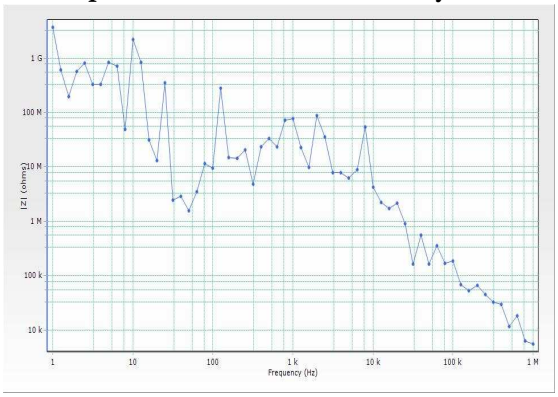

Fig.11. The Impedance Measurement for Un-annealed NiO thin film

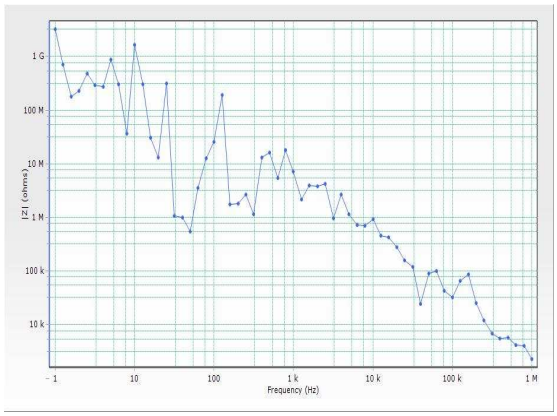

Fig.12. The Impedance Measurement for Annealed NiO thin film

From the above figures the impedance value decreased with the increasing of frequency as shown in the figures 21 and 22 are annealed and Un-annealed NiO oxide thin films.

3.9. Dielectric constant Measurement

Table 3: The Impedance and Dielectric constant values for corresponding selected Frequencies

Frequency	Before Annealing		After Annealing	
(Hz)	|Z| (ohms)	Dielectric (ε*r*)	|Z| (ohms)	Dielectric (ε*r*)
1000000	5550.27	8.56E-14	2310.54	2.89693E-13
501187.2	11670.89	8.13E-14	5760.86	2.31828E-13
100000	183548.86	2.59E-14	32202.5	2.07856E-13
50118.72	161221.92	5.88E-14	89745.7	1.48812E-13
10000	4295522.13	1.11E-14	928641	7.20783E-14
5011.873	6216526.75	1.53E-14	1137074	1.17453E-13
1000	77598248.2	6.13E-15	7132245	9.38482E-14

Sensing Test

The selected samples were placed inside the gas testing chamber and the response of the films towards the various concentrations of ethanol has been studied and reported. The sensitivity test is carried in Electrometer (Kethiley 6517 A model).

Sensing Mechanism

Oxygen ion adsorption gives the reduction electrons and increases the resistance of NiO. Reactive oxygen species such as O^{2-}, O^{2-} and O^{-} are adsorbed on the metal oxide NiO surface at elevated temperature, and the amounts of such chemisorbed oxygen species depend strongly on temperature. Low temperatures O^{2-} is chemisorbed, while at high temperatures, O^{2-} and O^{-} are chemisorbed and the O^{2-} disappears rapidly.

The whole of the oxygen adsorption can be described by the following formulae:

O_2 (gas) ↔ O_2 (adsorbed) (1)

O_2 (adsorbed) $+e-$ ↔ O_2 (ads)$-$ (2)

O_2 (ads)$^{2-}$ $+e-$ ↔ $2O_{(lat)}^{2-}$ (3)

Sensitivity

The sensitivity S for gases is defined by the form:

$$S = (Ro - Rgas)/Ro$$

Where, Ro is the resistance of the sensor in the absence of gas

Rgas is the resistance in the presence of gas.

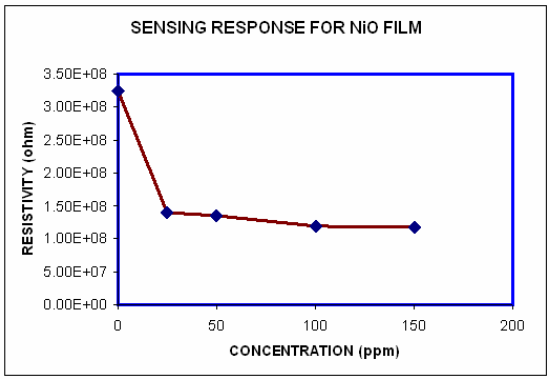

Fig.13 Ethanol sensing response for Un-annealed NiO thin film

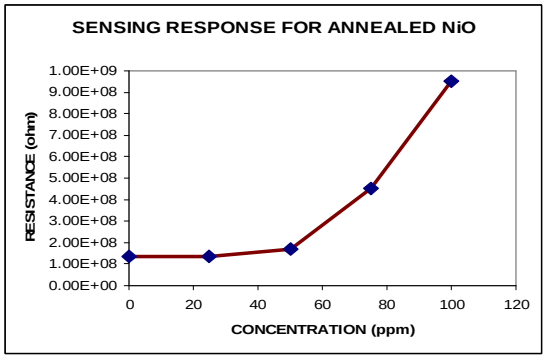

Fig.4 Ethanol Sensing response for annealed NiO thin film

Concentration	NiO thin film		Annealed NiO thin film	
ppm	Resistance(Ω)	Sensitivity	Resistance(Ω)	Sensitivity
0 (RT)	$1.65X10^{9}$	-	$1.50X10^{12}$	-
0 [100°C]	$3.25X10^{8}$	0	$1.35X10^{8}$	0
25[100°C]	$1.4X10^{8}$	56.92	$1.36X10^{8}$	0.74
50 [100°C]	$1.35X10^{8}$	58.46	$1.70X10^{8}$	25.92
100 [100°C]	$1.20X10^{8}$	63.69	$4.50X10^{8}$	233.33
150 [100°C]	$1.18X10^{8}$	63.69	$9.50X10^{8}$	603.70

Conclusion

- The NiO thin films were deposited on glass substrates using spray pyrolysis technique with $Nicl_2 \cdot 6H_2O$ as precursor.
- The X-Ray diffraction pattern shows that the film is polycrystalline in nature. It exhibits intense peaks corresponding to the (111) orientations of cubic NiO. The grain size of the particle estimated using the scherre'rs formula and the value is 43.31nm.

- SEM images show that surface morphology of the NiO film particles that are in the spherical shape. NiO film has good uniformity and the grain size of the particles are 25-50nm
- The optical analysis of Nickel oxide having partially transmittance. The band gap energy is 3.5-3.6eV. The average transmittance value upto 45% and the absorption of the film having low absorption in the visible region while the UV region is high.
- The Impedance measurement shows that impedance values increased when the frequencies are increased and it has low dielectric constant.
- The sensing analysis of the NiO films towards various concentrations of ethanol were studied at an operating temperature of 373K and it is concluded that the resistance of the NiO thin film increased with increasing the concentration of ethanol gas.

References

[1] Thin Film Solar Cells, edited by K.L. Chopra and S.R. Das ~Plenum, New York, 1983, p.607.
[2] Chopra, K.L., Major, S., Pandya, D.K., 1983. Thin Solid Films 102, 1.
[3] Muller, J., Weissenrieder, J.S., 1994. J. Anal. Chem. USSR 349, 380.
[4] Lin, F.C., Takao, Y., Shimizu, Y., Egashira, M., 1995. J. Am. Ceram. Soc. 78, 2301.
[5] Bose, S., Barua, A.K., 1999. J. Phys.D: Appl. Phys. 32, 213.
[6] Kim, H., Gilmore, C.M., 2000. Appl. Phys. Lett. 76, 259.
[7] Szarko, J.M., Song, J.K., Blackledge, C.W., 2005. Chemical Physics Letters, 404, 171-176.
[8] Ootsuka, T., Liu, Z., Osamura, M., 2005. Thin Solid Films, 476, 30 – 34.
[9] Sahay, P.P., Tewari, S., Nath, R.K., 2007. Cryst. Res. Tec hnol. 42, 723 – 729.
[10] Soon-Jin So, Choon-Bae Park, 2005. Journal of Crystal Growth 285, 606.
[11] Tan, S.T., Chen, B.J., Sun, X.W., Hu, X., Zhang, X.H., Journal of Crystal Growth 281, 571.
[12] Young-Sung Kim, Weon-Pil Tai, Su-Jeong Shu, 2005. Thin Solid Films 491, 153.
[13] Ashour, A. Kaid, M.A., El-Sayed, N.Z., Ibrahim, A.A., 2005. Applied Surface Science In Press.
[14] Martins, R., Igreja, R., Ferreira, I., Marques, A., Pimentel, A., Gonçalves, A., Fortunato, E., 2005. Materials Science and Engineering B 118, 135.
[15] Dikovska, A.Og., Atanasov, P.A., Vasilev, C., Dimitrov, I.G., Stoyanchov, T.R., 2005. J Optoelectron. Adv. Mater. 7, 1329.
[16] Masayuki Okuya, Koji Nakade, 2004. Journal of Photochemistry and Photobiology A: Chemistry 164, 167-172.
[17] Cullity sr.stock, B.D., Elements of X-ray Diffraction, 3rd Prentice Hall, 2001.
[18] Suryanarayana, C., Norton, Grant, M., X-ray Diffraction A practical Approach, New York, 1998.